Single-molecule tools
to study DNA-based processes

Machteld E. Kamminga

Abstract

Single-molecule tools represent a powerful approach to study molecular processes without the averaging present in conventional ensemble-averaging methods. This thesis contains three single-molecule research projects. All research projects contain real-time, single-molecule observation of DNA processes in a flow cell, where a laminar flow is used to stretch out multiple DNA molecules at the same time. The DNA processes are visualized using fluorescence microscopy. In the **_first research project_**, the effect of flow speed and buffer composition on the flow-stretched length of λ phage DNA is investigated. It was found that the presence of divalent magnesium ions in the buffer solutions has a negative influence on the stretched-out length, due to interactions with the negatively charged DNA backbone. In the **_second research project_**, the role of the _Escherichia coli_ β clamp protein in DNA replication is investigated by carrying out M13 rolling-circle replication experiments. To visualize the β clamps, the proteins were labelled with fluorescent molecules, yielding labelling efficiencies up to 90.4 %. It was proven that the labelled proteins maintained their functionality in DNA replication, by simultaneously imaging replication product growth and displacement of the β clamp at the tip of the product. It was found that the β clamps were left behind on the replication product after formation of each Okazaki fragment. Moreover, it was shown that no Okazaki fragments were formed in the absence of DnaG primase. In the **_third research project_**, an attempt was made to bring DNA molecules up in the flow by attaching them to a suspended gold nanowire, produced by nanoskiving. λ phage DNA molecules were successfully synthesised on pieces of 400 nm thick gold wires that were sticking out in the middle of the flow cell. Significant lowering of the flow rate resulted in still having fully stretched-out λ DNA molecules. This proved that the flow profile was indeed enhanced upon bringing the DNA molecules up in the flow cell.

Keywords: single-molecule, fluorescence microscopy, DNA replication, β clamp, nanowires, nanoskiving.

List of abbreviations

AFM	=	atomic force microscopy
ATP	=	adenosine triphosphate
CTP	=	cytidine triphosphate
dATP	=	deoxyadenosine triphosphate
dCTP	=	deoxycytidine triphosphate
dGTP	=	deoxyguanosine triphosphate
DNA	=	deoxyribonucleic acid
dNTPs	=	deoxyribonucleoside triphosphates
ds-DNA	=	double-stranded DNA
DTT	=	dithiothreitol ((2S,3S)-1,4-bis(sulfanyl)butane-2,3-diol)
dTTP	=	deoxythymidine triphosphate
E. coli	=	*Escherichia coli*
FRET	=	Förster resonance energy transfer
GTP	=	guanosine triphosphate
NHS	=	*N*-hydroxysuccinimide (1-hydroxy-2,5-pyrrolidinedione)
NTPs	=	ribonucleoside triphosphates
PBS	=	phosphate buffered saline
PDMS	=	polydimethylsiloxane
PEG	=	polyethylene glycol
RNA	=	ribonucleic acid
SAM	=	self-assembled monolayer
SSB	=	single-stranded binding protein
ss-DNA	=	single-stranded DNA
TIRF	=	Total internal reflection fluorescence
Trolox	=	6-hydroxy-2,5,7,8-tetramethylchroman-2-carboxylic acid
UTP	=	uridine triphosphate

Table of contents

1.   Introduction to single-molecule biophysics

All experiments in this thesis are related to the research field of single-molecule biophysics. Therefore, this chapter provides a general introduction to single-molecule biophysics. The first section will focus on the field of biophysical research and the challenges biophysical experiments contain. The second section will provide an overview of commonly used single-molecule imaging techniques, together with their advantages and limitations. The third section will introduce the DNA processes that are studied in this research project and outline what is written in each chapter.

1.1   Biophysical research and challenges

Biophysics is a relatively young field of research [1]. Since about the 1840's, scientific research has been carried out in which attempts were made to explain (biological) phenomena of life in a physical or mathematical way. However, it still took another 80 years before biophysics came up as a separate discipline in science itself. As the name suggests, biophysics is a bridge between biology and physics. In one of the earlier books, biophysics was defined as follows: *"Biophysics deals with the application of physical and physicochemical laws to the action of living things."* [2]. This is a particularly broad definition, and as Loofbourow already wrote in an article in 1940: *"… there does not seem to be a clear agreement, even among biophysicists, as to what the term biophysics means."* [3], there is no narrow interpretation of the meaning of biophysics. Biophysics combines biology with physics and this bridge between biology and physics works in two directions [4]. In biology, physical and mathematical tools can be used to simplify the complexity of life in order to get an easier understanding. The other way around, physical studies can be inspired by biological systems, especially concerning the physics of complexity and disordered systems. As a result, one single person can be referred to as a biophysicist or a biological physicist, simply by how the direction of his research is defined along this bridge. Thus, the field of biophysics can be stated to include biological physics, physical biology and everything in between and related to it. This still remains a broad definition and the main reason for this is that the scope of the field is very broad and keeps growing. Every breakthrough, like the acceptance of a model or the invention of new analysis methods and tools, leads to new lines of research within the field and hence a growth of the entire field. An example is Watson and Crick's model of the double helical structure of DNA (deoxyribonucleic acid) [5], which had an enormous impact in molecular biology. The combination of this model with the newer physical and mathematical tools enlarged the scope of biophysics at that time.

A more recent breakthrough that had an enormous impact is the possibility to study biological processes at the single-molecule level. The detection of single molecules was first accomplished in 1977, when single atoms in the gas phase were studied [6]. However, it took another twelve years before single molecules were detected in a solid matrix at low temperatures [7]. In 1990, the first detection of individual fluorescent molecules in solution was made [8]. The possibility to study biological processes at the single-molecule level enlarged the field of research. As an example, single-molecule assays made it possible to reveal protein [9] and enzyme [10] synthesis, in both *in vivo* and *in vitro* studies.

Most single-molecule methods rely on the attachment of light-scattering or -emitting labels to the molecule of interest in order to visualize them one-by-one. As a result, single-molecule experiments can gain insight into molecular motion of individual particles. Single-molecule techniques give the ability to study the interactions between various systems of a cell, including the interactions between DNA, RNA (ribonucleic acid) and proteins, as well as how these interactions are regulated. Examples include measurements of step sizes of molecular motors [11] [12], probing DNA-protein interactions upon unzipping double-stranded DNA [13], exploring mechanisms of unfolding [14] and observation of folding trajectories of single proteins [15] [16] [17]. Thus, single-molecule biophysics aims to address a variety of biologically important questions, such as how do protein machineries work, how do viruses invade cells and how does cell division take place? The main relevance of these questions is that a better understanding of biological mechanisms in both health and disease will open new possibilities in drug design, diagnosis and disease control by preventing and curing diseases. For example, Parkinson's disease is associated with misfolding of proteins [18]. These misfolded proteins obtain a different native structure and perform a different biological mechanism [19], which results in such a disease. Thus, understanding how this (mis)folding works will be relevant in the field of medicine.

The main advantage of single-molecule experiments over bulk experiments, is that it gives information about one single molecule, instead of giving an average over all molecules. However, studying individual molecules is still a challenge. In order to be able to distinguish single molecules, the molecule of interest should be highly diluted into the reaction mixtures (in the order of nM or pM), which could drastically decreases their efficiency in reactions. This makes it harder to visualize them. Another point it that labelling of the molecule with a light-scattering or –emitting small molecule, which is necessary to track the molecule, might interfere with the function of the molecule which is studied. Moreover, microscopic imaging techniques are limited by their diffraction limit, and some structures are too small to be observed in detail. This are challenges that single-molecule experiments brings with it, and these challenges will also be visible in the experimental parts of this thesis.

1.2   Single-molecule imaging techniques

This section will highlight a couple of the most commonly used approaches for high-resolution measurements of single-molecule motion. These techniques include atomic force microscopy, optical traps, magnetic tweezers and TIRF microscopy. For each technique the operating principles, applications, capabilities and limitations for practical use are examined.

Atomic force microscopy, optical traps and magnetic tweezers are force-based single-molecule methods. Using force-based methods to study molecular motion has two main advantages: applying a force to single-molecules increases the stiffness of the molecule and hence the resolution (reduction of amount of fluctuations), and it can modify the energy landscapes for the motion under study. This last point is illustrated in figure 1.1. In this figure it is visible that applying an external force changes the energy landscape of the molecule under study and hence the kinetics of its motion.
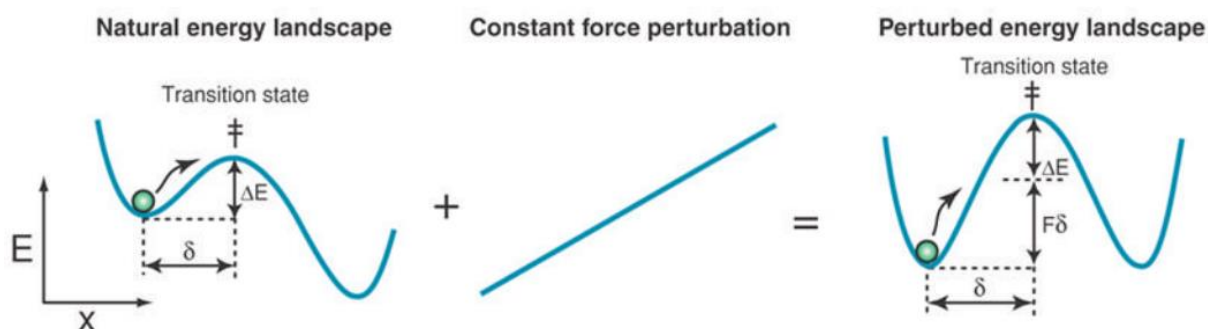
Figure 1.1: *The effect of a force perturbation on the energy landscape of a molecule. The illustrated perturbation increased the energy barrier necessary to overcome to reach the transition state. Figure source: [20].*

Atomic force microscopy

Atomic force microscopy (AFM) uses a cantilever to exert force upon a single molecule which is bound to the cantilever on one side and to a piezoelectric probe on the other side. The piezoelectric probe modulates the force upon the molecule, which results in a deflection of the cantilever. The cantilever acts as a linear spring and its deflection is measured by the position-sensing detector that measures the reflection of the laser beam off the cantilever. Figure 1.2 shows an animated figure of how this looks like.
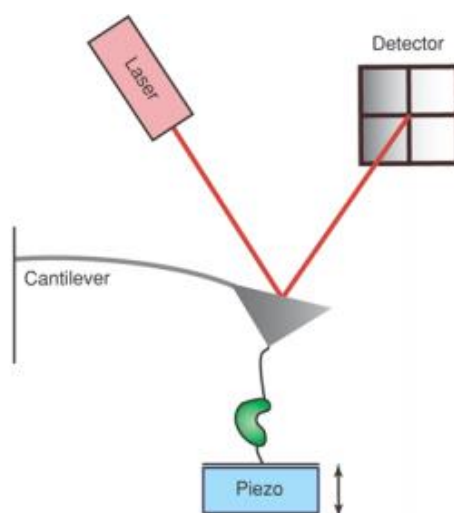
Figure 1.2: *Schematic drawing of an AFM setup. The motion of the molecule is measured by measuring the deflection of the cantilever as function of the force applied to the molecule through the piezoelectric probe. Figure source: [20].*

The cantilevers are usually very stiff. Therefore, forces between 10 and 10,000 pN can be exerted onto the single-molecule. AFM is used for example to study the mechanical strength and stability of proteins [21], the strength of disulfide bonds [22] and to study unfolding of proteins [23] [24].

However, a limitation of AFM experiments is this lower bound of 10 pN. The forces associated with many biological processes and structures are therefore hard to study with an AFM [25]. A major drawback of doing single-molecule AFM studies is that the molecule is usually attached to the cantilever tip by bringing the tip in contact with the molecule, applying a large force and pulling it back. This results into nonspecific absorption of the molecule to the cantilever tip. As a result, the attachment geometry is unknown and

uncontrollable. Moreover, it can be difficult to discriminate between interactions of the cantilever tip with the molecule of interest from these nonspecific interactions and undesired interactions with the molecule through for example binding at an intermediate position rather than at one of the ends as illustrated in figure 1.2 [25]. Other limitations for practical use are the sources of noise that affect the measurement: motions of the sample with respect to the tip, which include thermal expansion and piezo creep, and optical interference effects between the tip and the surface [20].

Optical traps

Optical traps (also referred to as optical tweezers) are created by focussing a tightly-focussed laser beam on a small dielectric bead which is attached to one side of the molecule of interest while the other side is tethered to a surface. This tightly-focussed laser beam exert radiation pressure onto the small dielectric particle which is polarized by the strong electromagnetic field. The interaction of this optically induced dipole with the steep gradient near the focus of the laser beam results in a force directed along the gradient and proportional to the intensity of the laser light. The applied force can be modified by adjusting the intensity of the laser or by physically moving the trap or the surface to which the molecule is attached to. Figure 1.3 shows schematically how a DNA strand can be stretched out using an optical trap. Instead of tethering the single-molecule to a surface on one end, it is also possible to use a second optical trap.
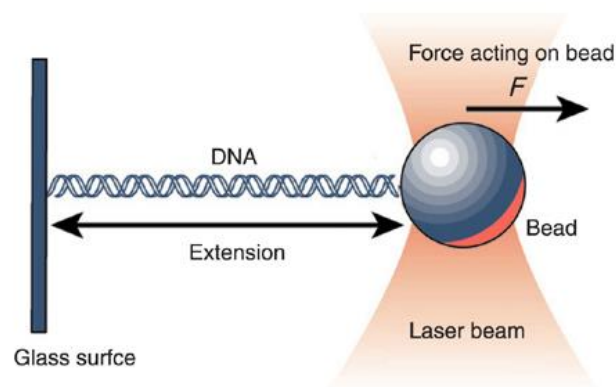

Figure 1.3: Illustration of a single DNA molecule attached to a glass surface and stretched out by an optical trap. Figure source: [26].

The stiffness of optical traps is typically lower than that for AFM cantilevers and consequently the forces that can be applied to the molecule are lower, in the range of 0.1 – 100 pN. With optical traps it is possible to measure motions of single biomolecules in real time over particularly long timescales (ranging from minutes to hours) with a resolution of around 1 Å at 50 Hz [20]. Optical traps are for example used to investigate the elastic properties of single-stranded RNA molecules [27], to measure DNA-protein interactions [13] and to characterize folding of proteins [15] [28].

A limitation, particularly *in vivo*, is the photodamage to the biomolecule under study from the intense light coming from the optical trap. Optical traps are most often generated using lasers with wavelengths in the near-infrared. The reason for this is that it was found that most biological materials are transparent in this region [29]. Moreover, the high intensity at the focus point of the trapping laser beam results in local heating and this can influence the enzymatic activity of the cell under study. Another drawback of the use of

optical traps is that they lack selectivity and exclusivity. In essence, all dielectric particle moving near the focal point of the laser can be trapped and there can be multiple particles trapped at the same time. Moreover, optical interference and non-ideal behaviour of the beam-steering optics can result in the generation of ghost traps [25].

Magnetic tweezers

Magnetic tweezers are similar in concept to optical traps. A molecule is bound between a surface and a small magnetic particle. This is illustrated in figure 1.4. This particle experiences a force proportional to the magnetic field gradient from the small permanent magnet. The permanent magnet gives the bead two degrees of freedom. It can move in the lateral direct, similar as in case of optical traps, but with forces ranging from around 0.05 – 20 pN [20], and it can rotate, as shown in figure 1.4. The magnetic bead acts as a dipole within the applied magnetic field, which allows the magnetic tweezers to apply torque. Instead of using a permanent magnet, electromagnets can also be used in order to modify the applied magnetic field.
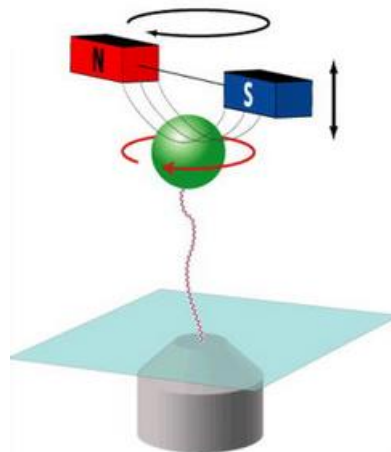

Figure 1.4: Schematic drawing of magnetic tweezers, based on a permanent magnet. Figure source: [25].

Magnetic tweezers have some advantages over optical traps, because they do not induce photodamage or heating in the sample. Moreover, permanent magnet configurations are relatively easy to assemble. The possibility to rotate samples, makes magnetic tweezers suited for studies that include over- or unwinding of DNA. Examples of studies that used magnetic tweezers include the investigation of the unwinding-response of DNA to force [30] and the effect of drugs on DNA extension [31].

A major disadvantage of using magnetic tweezers is that the bandwidth and sensitivity of the measurements are limited by the video-based detection, which prevents the possibility to directly detect very fast or very small displacements [25]. Moreover, the temporal resolution limit is typically fairly limited because of the viscous drag associated with the relatively large magnetic beads, which are usually 1-4 μm in diameter [20].

TIRF microscopy

TIRF (total internal reflection fluorescence) microscopy is a 'passive' technique in comparison to AFM, optical traps and magnetic tweezers, in the sense that it does not involve any exertion of a force onto the molecule of interest. TIRF microscopy is based on direct visualization of molecular motion by fluorescently labelling the molecule under

interest and real-time detection of the fluorescent signal. As the name suggests, TIRF microscopy is based on the total internal reflection phenomenon that occurs when light passes from a high-refractive medium, such as glass, into a low-refractive medium, such as water or biological cells [32]. No light propagates into the sample, but a thin evanescent field of roughly 100 nm is generated by the total internal reflection of the incoming light at the glass-sample interface. This evanescent field decays exponentially with the distance from the glass-sample interface and depends on the refractive index of the glass and sample, and the angle of the incoming light. This is illustrated in figure 1.5. When the angle of the incoming light beam is below a critical value, which depends on the refractive index, there will be nog total internal reflection and most of the light will pass through the sample. In that case, fluorescence microscopy is said to take place in epifluorescence. When the angle is higher than the critical angle, total internal reflection takes place and the evanescent field is formed. Changing this angle, called TIRF angle, varies the depth of the evanescent field.
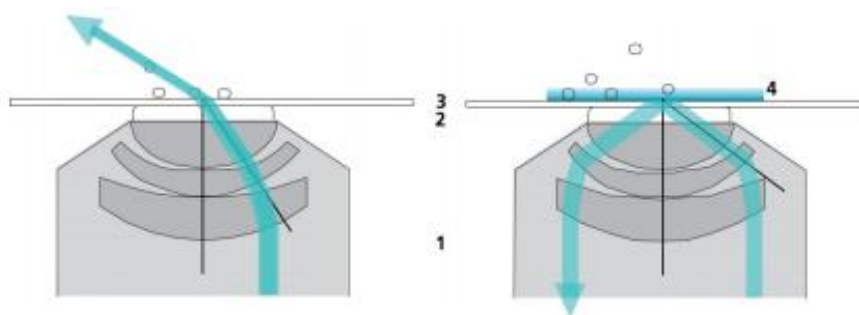

Figure 1.5: Illustration of TIRF microscopy inside the objective. The left image shows the beam path below the critical angle (epifluorescence) and the right image shows the beam path under total internal reflection. 1: Objective, 2: Immersion liquid (high refractive oil used to increase microscope resolution) , 3: Glass coverslip, 4: Evanescent field. Figure source: [33].

The most straightforward method to use TIRF microscopy to track the motion of a single-molecule is by tagging the molecule with a label that is easily visualized, i.e. a fluorescent dye molecule, protein or quantum dot. Real-time motion of the single molecules can be recorded by measuring the light emitted from the fluorophores. By fitting the intensity profile and measuring the centre of the fluorescence distribution, a fluorophore can be localized with a precision up to 1.5 nm [20]. However, this method reaches its limit when trying to visualize internal molecular rearrangements or small motions that occur on the millisecond timescale.

Förster resonance energy transfer (FRET) makes it possible to study small (nanoscale) motions and conformational changes through the resonant coupling of two different fluorophores attached to the molecule under study. Figure 1.6 shows how this works. One of the two fluorophores is excited by the incoming light beam and this donor fluorophore then transfers energy nonradiatively via the Förster dipole-dipole interaction to the nearby acceptor fluorophore. The condition for this energy transfer to happen is that the absorption spectrum of the acceptor must overlap the emission spectrum of the donor. Hence, a good donor and acceptor fluorophore pair must be selected for FRET experiments. The efficiency of FRET is given by the following formula: $E = (1 + [R / R_0]^6)^{-1}$ and is strongly dependent on the distance R between the donor and the acceptor. The FRET efficiency is therefore a measure of the distance between the two labels. Conformational changes in a molecule can thus be interpreted as a change in this FRET efficiency. The Förster radius R_0 is defined as the

distance between the donor and the acceptor where the efficiency is 50%. This value depends on the donor-acceptor pair chosen, but is typically in the order of 2-6 nm [34].
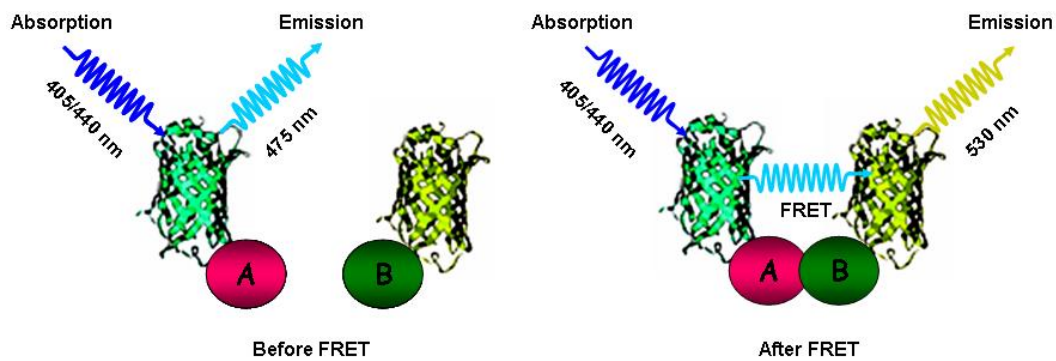

Figure 1.6: Detection of protein-protein interaction via FRET. Protein A emits at 475 nm. When protein A and B are close to each other, FRET takes place between the fluorophores and the complex emits at 530 nm. Figure source: [35].

An advantage of TIRF microscopy is that the evanescent field produced by the total internally reflected light excites the fluorescent molecules close to the glass-sample interface while the remaining sample volume is minimally exposed. This results in high-contrast fluorescence images of single molecules near the surface, with a high signal-to-noise ratio. The background is low due to minimized out-of-focus fluorescence, because the excitation of fluorophores further away from the coverslip is reduced [32]. Examples of what has been studied in biology with TIRF microscopy are the dynamics of skeleton filaments [36] and the quantification and characterization of the fusion of vesicles with the plasma membrane [37].

The above described way of tracking single molecules with TIRF microscopy also has limitations. TIRF microscopy can only be used to examine the molecules that are in close proximity to the glass-sample interface. Despite the fact that the signal-to-noise ratio is high, it cannot give insight into motions of molecules that are further away. Another problem might be the attachment of fluorophores to the molecule of interest. The fluorophore must be covalently attached in a region where it will not disturb the function of the. This requires significant knowledge of the target molecule. Moreover, photobleaching of the fluorophore can happen when doing TIRF experiments. Photobleaching is the permanent loss of fluorescence and hence dimming of the observed molecule over time. Reactive oxygen species induce photobleaching. When oxygen collides with the fluorescent molecule in its excited state, it quenches the fluorescence by trapping it into a triplet state, which is not fluorescent. Oxygen can also undergo a chemical reaction with the dye, which will result in permanent photobleaching. The photostability of a dye can be increased by ten times when an oxygen scavenger system (usually containing glucose oxidase and catalase) is introduced within the reaction mixture [38]. Another problem that can occur is the photodamage that can take place, as described above for the optical traps.

1.3   Single-molecule tools to study DNA-based processes

This section will give a short overview of the research carried out in this thesis. The following three chapters cover three single-molecule research projects. All research projects contain real-time, single-molecule observation of DNA processes in a flow cell. In order to perform single-molecule studies on DNA, for example studies that involve tracking proteins that carry out DNA replication, it is important to stretch out the DNA strands to have a clear image of what happens were. The previous section described various techniques to stretch out single DNA molecules, namely AFM, optical traps and magnetic tweezers. Although this can give a well-defined stretching of the DNA, only one molecule can be studied at the time, which is unfavourable for obtaining significant statistics. Therefore, all research in this thesis is carried out in a flow cell where a laminar liquid flow is used to stretch out multiple DNA molecules at the same time. This flow is created through suction of a syringe pump. A TIRF microscope is used to observe the stretched-out DNA and the proteins that interact with it. The flow cells are constructed by pouring PDMS (polydimethylsiloxane) over a lithography-made master, baking it and removing the PDMS from the master as illustrated in figure 1.7. The protocols of constructing the lithography masters and making the PDMS channels are given in Appendix D.1 and D.2 respectively.
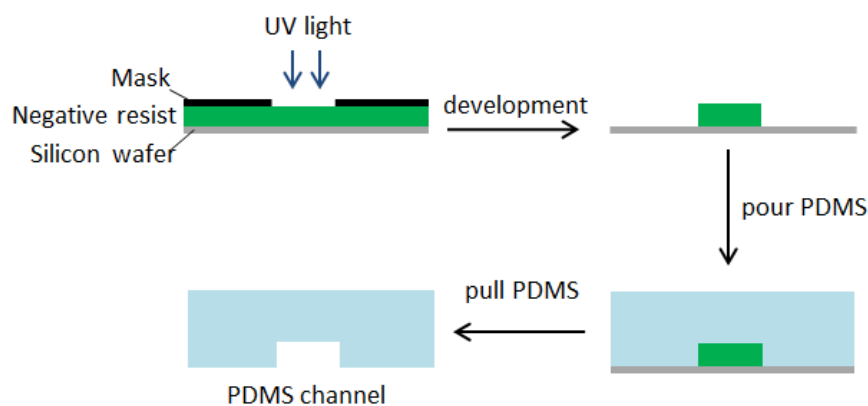

Figure 1.7: Illustration of PDMS flow cell fabrication using photolithography.

This flow-channel-shaped block of PDMS is then placed onto a functionalized glass coverslip, using polyethylene tubing for flow inlet and exit. The glass coverslips are functionalized by covalently binding biotin-bearing polyethylene glycol (PEG) to it in order to provide an inert layer between the protein, DNA and the glass. This is done to reduce nonspecific interactions [39]. The attachment of the DNA molecules is done via biotin-streptavidin-biotin linkage. After functionalizing the coverslip with biotin, incubating in streptavidin and constructing the flow cell by placing the PDMS on top, the stretched-out DNA molecules are created *in situ* by flowing in biotinylated DNA molecules.

Chapter 2 describes the effect of the flow speed and buffer composition on the flow-stretched length of λ phage DNA. Chapter 3 investigates the role of an *Escherichia coli* protein, the β clamp, in DNA replication kinetics. Here the protein will be fluorescently labelled to track its motion during DNA replication in order to investigate its function. Chapter 4 shows how the stretching of the DNA can be improved when the DNA molecules are attached to a suspended gold nanowire that brings the DNA up in the flow. This will result in a better flow profile along the stretched DNA.

2. Flow-stretched λ phage DNA length calibration

This chapter describes the effect of flow speed and buffer composition on the flow-stretched length of λ phage DNA. At first, a brief introduction is given. The two sections that follow describe the length of flow-stretched λ phage DNA as a function of flow speed and buffer solution composition. The fourth section focuses on the force profile along the flow-stretched DNA. Finally, some concluding remarks are made. This research project is carried out together with Enrico Monachino (PhD student, Van Oijen Lab).

2.1 Introduction

The main goal of this research project is to calibrate the length of λ phage DNA for the fluorescence microscope setup used in the Van Oijen Lab. In other words, to determine the physical length of λ phage DNA strands as a function of experimental conditions such as flow speed and buffer solution composition. This length calibration makes it possible to determine for example replication rates (i.e. the amount of base pairs per second replicated) more precisely by measuring the growth in pixels with the microscope camera and converting it to physical length for the experimental conditions used.

λ phage is a bacteriophage that infects *Escherichia coli* (*E. coli*). A bacteriophage is a virus that infects and replicates within bacteria. Since the discovery of λ phage by E.M. Lederberg in 1951 [40], λ has become a model organism in which many foundational studies lead to our current understanding of how genes work and how they are regulated, as well as how proteins perform DNA replication [41]. Figure 2.1 shows an illustration of λ phage as well as an electron micrograph.
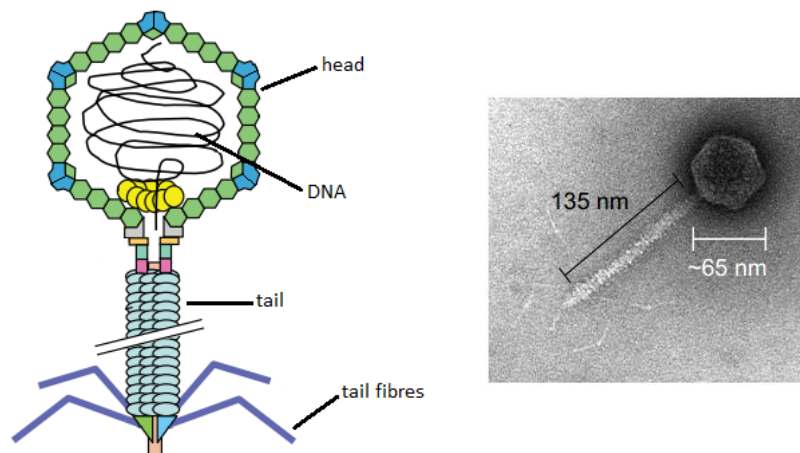
Figure 2.1: Left: illustration of λ phage indicating the head, tail, tail fibres and DNA. Right: electron micrograph of λ phage. Figures adapted from [41].

The double-stranded DNA (ds-DNA) genome is encapsulated within proteins. This shell with ds-DNA in it makes up the head of the λ phage as shown in figure 2.1. The tail with tail fibres recognizes *E. coli* and binds to it. After binding, it injects its DNA genome through the tail into this cytoplasm of the host cell. Once the λ phage DNA has entered the host cell, the DNA circularizes and will go into a lytic or lysogenic cycle. This is illustrated in figure 2.2. When it enters the lytic cycle, new λ phage DNA and proteins are synthesized and assembled into

new virions. These new λ phages will then be released from the host cell and can again infect new cells. When it enters the lysogenic cycle, the DNA of the λ phage integrates with the DNA of the *E. coli* host cell and become a so-called prophage. After that, the bacterium will reproduce normally through cell division, resulting in multiple λ phage infected cells. In some of these cells, the integrated λ phage DNA will excise from the *E. coli* chromosome and will go into a lytic cycle.
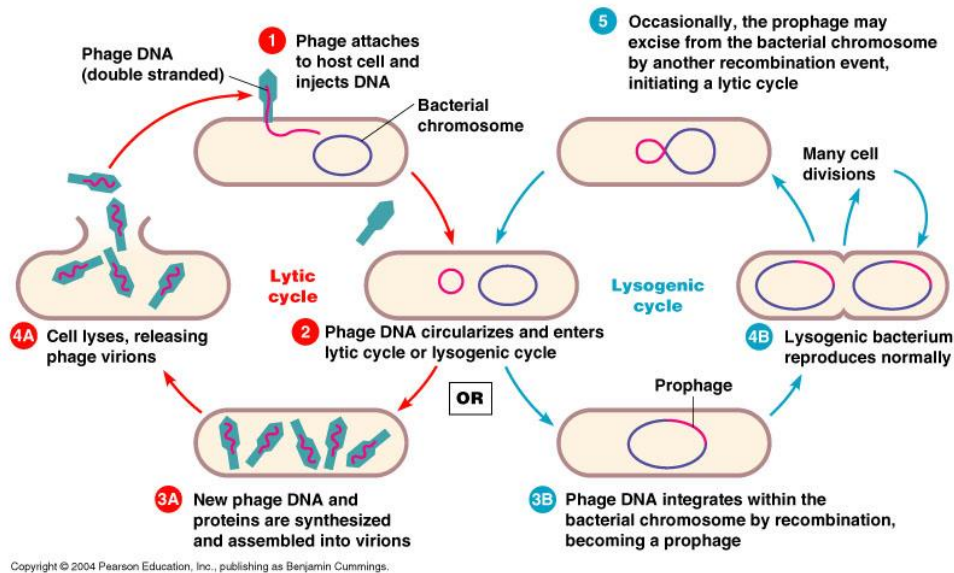

Figure 2.2: Scheme indicating the possible pathways that can happen when a phage infects a host cell: the lytic and lysogenic cycle. Figure source: [42].

There are various methods to purify, i.e. to isolate, phage DNA from the infected bacteria [43] [44] [45]. This isolated DNA can be used in various studies, as described above. The λ phage genome contains 48,490 base pairs of linear ds-DNA, with 12 base pairs long single-stranded DNA (ss-DNA) at both 5' ends [46]. λ DNA has a contour length of 16.5 µm [47]. In the circular form of step two of figure 2.2, the genome is 48,502 base pairs long in length. These 12 base pairs long ss-DNA overhangs are used to attach modified and unmodified DNA oligonucleotides (in short, oligos) using standard annealing and ligation techniques. A biotinylated oligo is annealed to the 5' end of the λ DNA, providing surface binding through the in section 1.3 described biotin-streptavidin-biotin linkage of the DNA strand with the functionalized coverslips. A λ complementary forked arm is annealed to provide a leading-strand template for DNA replication experiments. Figure 2.3 shows how the λ DNA template used in this study looks like.
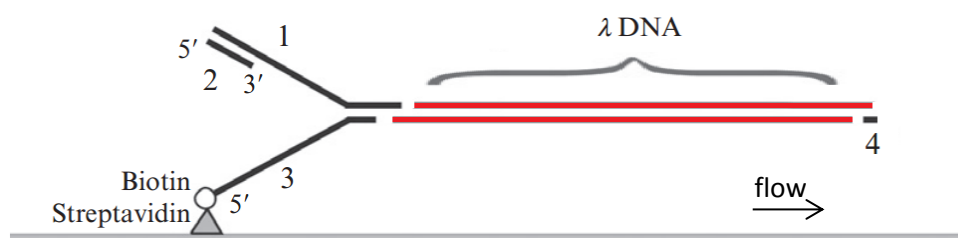

Figure 2.3: Illustration of the λ DNA construct used in this study. Oligo 1 forms the fork arm, oligo 2 the leading-strand primer, oligo 3 the biotinylated fork arm and oligo 4 complements the strand. Figure adapted from [48].

For more information regarding the exact preparation of this template and the oligos needed for this construction is referred to [48].

As stated in the introduction, TIRF microscopy is used as the imaging technique to determine the flow-stretched length of the DNA for different experimental conditions. SYTOX Orange DNA stain is used to visualize the flow-stretched λ DNA. SYTOX Orange is a commercially available nucleic acid stain which has an absorption and emission peak at 547 and 570 nm respectively when bound to DNA. Figure 2.4 shows the absorption and fluorescence emission spectra. The Van Oijen Lab uses a 532 nm laser to excite SYTOX Orange.
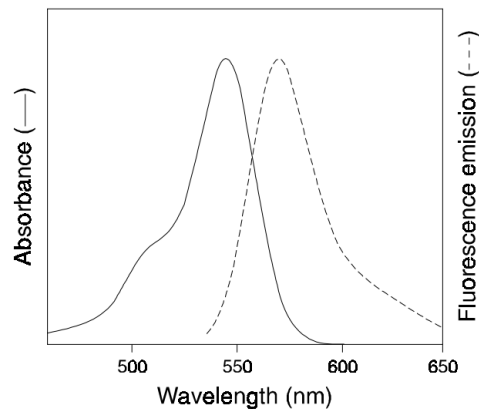
Figure 2.4: *Absorption and fluorescence emission spectra of SYTOX Orange nucleic acid stain bound to DNA. Figure source: [49].*

SYTOX Orange has a high fluorescence intensity and a large fluorescence enhancement upon binding to ds-DNA [50]. SYTOX Orange is an intercalating dye for DNA, meaning that it reversibly inserts into the DNA strand. Therefore, the full length of the DNA strand will be visible in fluorescence microscopy. Figure 2.5 shows a microscope image of how this looks. Note, however, that this image is slightly up in TIRF, because the λ DNA molecules are a little bit above the surface (around 200 nm), as shown in figure 2.3.
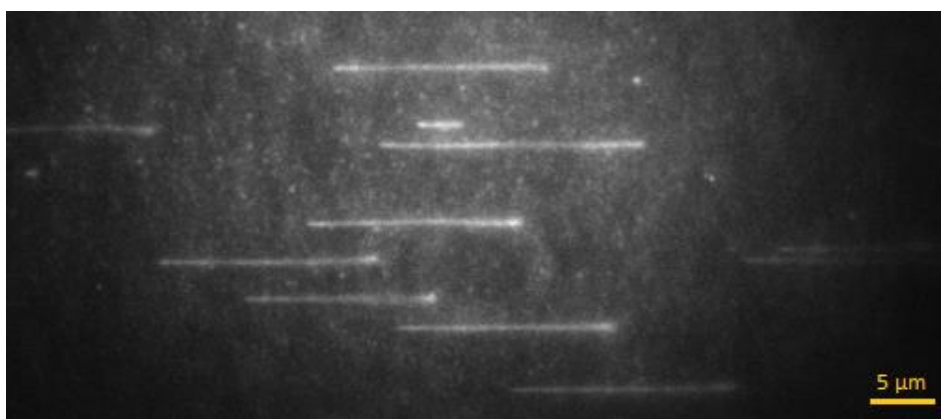
Figure 2.5: *TIRF microscope image of flow-stretched λ DNA stained with SYTOX Orange. Flow is coming in from the left at a flow rate of 5 µl/min. This image is a single frame, taken with an exposure time of 200 ms.*

2.2   Flow-stretched λ phage DNA length as function of flow speed

This section describes the flow-stretched λ phage DNA length as a function of flow speed. This experiment is carried out in a rectangular flow cell of 100 μm high and 500 μm broad, which is a standard size cell used in the Van Oijen Lab. The streptavidin-functionalized coverslips described in section 1.3 are used to build the flow cell. The stretched-out λ DNA molecules are created *in situ* by flowing in around 8.7 pM of biotinylated DNA molecules in blocking buffer (buffers are always degassed first, to prevent bubbles), together with 150 nM SYTOX Orange. Blocking buffer is a buffer used in the Van Oijen Lab to load the surface with DNA and to minimize nonspecific binding by 'blocking' the surface. For the chemical composition of blocking buffer, see Appendix A. After tethering the DNA to the surface, a wash solution of blocking buffer with 150 nM is used to wash out unbound DNA. With a laser (532 nm) power density of around 19 W/cm^2, short movies of 20 frames (with 200 ms exposure time) are taken at different places within the channel. After that, averaging over all 20 frames results in an image, such as in figure 2.5, in which the length of individual λ molecules can be determined. An important remark is that the long λ DNA molecules can break due to photocleavage, and therefore only full-length DNA molecules are considered in this calibration study. The average length and its error are determined by plotting the distribution of lengths in a histogram and fitting a Gaussian. This experiment is done for flow rates ranging from 2 μl/min up to 40 μl/min. Figure 2.6 shows the flow-stretched length of λ DNA as a function of the flow rate.

Figure 2.6: *Flow-stretched length (in μm) of λ DNA as a function of flow rate (in μl/min). This experiment is carried out in blocking buffer. The measurement points are fitted with a fitting function obtained from the worm-like chain model [51] [52] [53].*

Figure 2.6 shows a clear saturation behaviour. Such saturation behaviour is consistent with literature [51]. At significantly low flow rates, the DNA is not stretched out completely. A flow rate higher than 10 μl/min is necessary to stretch out the DNA and reduce the fluctuations. However, at high flow rates, more DNA molecules tend to break due to shear forces. Therefore, the optimal flow rate for measuring it between 10 and 20 μl/min. At these rates, the molecules are nicely stretched out and the majority has still the full length.

Since the goal is to obtain a calibration curve, figure 2.7 shows the conversion factor of the amount of base pairs per pixel, for the different flow rates. With the aid of this curve,

replication rates can be determined at all flow rates. At high flow rates, i.e. saturation length, the conversion factor is around 500 base pairs per pixel.

Figure 2.7: Conversion factor of number of base pairs per pixel of λ DNA as a function of flow rate (in μl/min). This experiment is carried out in blocking buffer.

During this experiment, it was found that the type of buffer has a significant influence on the length of the flow-stretched λ DNA. The above described experiment has been done in both blocking buffer and *E. coli* replication buffer, which is a buffer used to do replication experiments with *E. coli* proteins. Looking at the histograms, see figure 2.8, it is clear that there is a significant length difference. These histograms belong to the buffer dependence test of the next section.
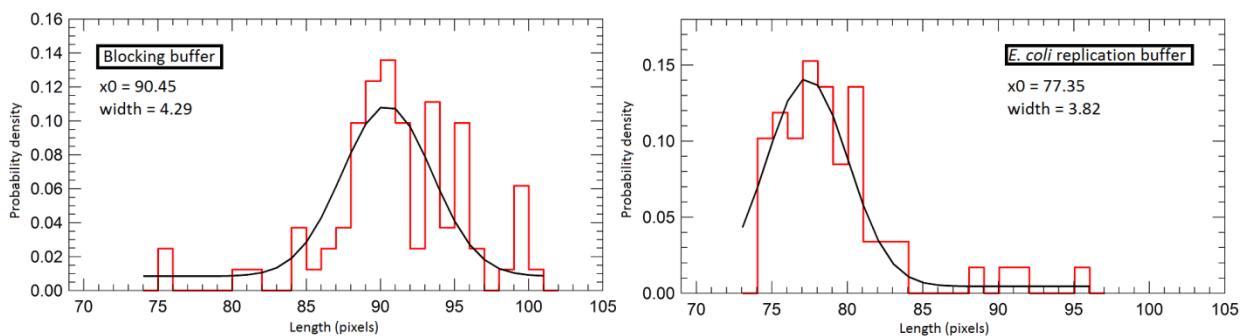
Figure 2.8: Histograms of flow-stretched λ length distributions for measurements done in blocking buffer and E. coli *replication buffer at 10 μl/min. The X-axis represents the length measured in pixels, the Y-axis represents the probability.*

Figures 2.9 and 2.10 show the length and conversion factor as a function of flow rate for both blocking buffer and *E. coli* replication buffer, indicating a clear difference. In both buffers, the saturation regime starts at around the same flow rate, i.e. between 10 and 20 μl/min. However, the full-stretched length of λ DNA in blocking buffer is around 16 μm, while in *E. coli* replication buffer it is around 12 μm. Thus, the conversion factor in *E. coli* replication buffer is around 650 base pairs per pixel as for the blocking buffer this was around 500 base pairs per pixel. A closer look at the chemical composition of the buffers is required. This is done in the following section.
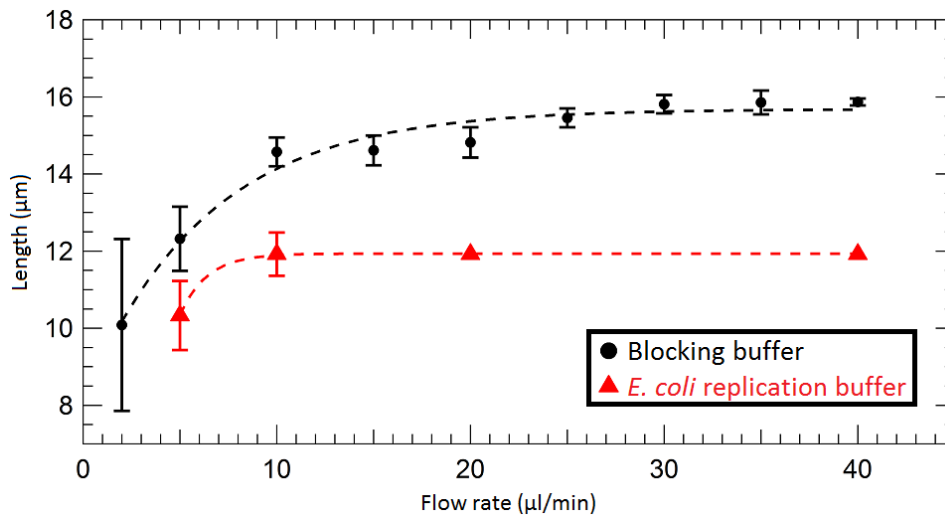
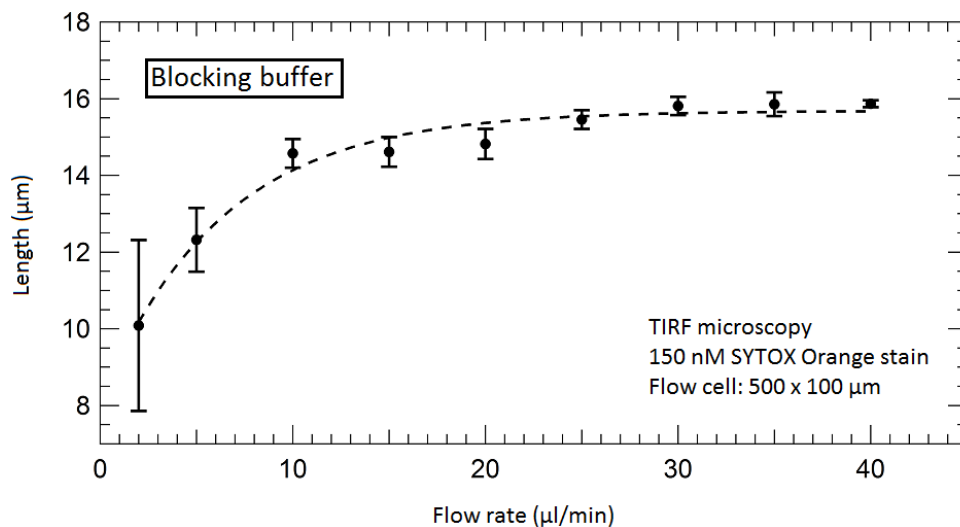*Figure 2.9:* *Flow-stretched length (in µm) of λ DNA as a function of flow rate (in µl/min) for experiments carried out in blocking buffer and* E. coli *replication buffer, showing a clear difference.*

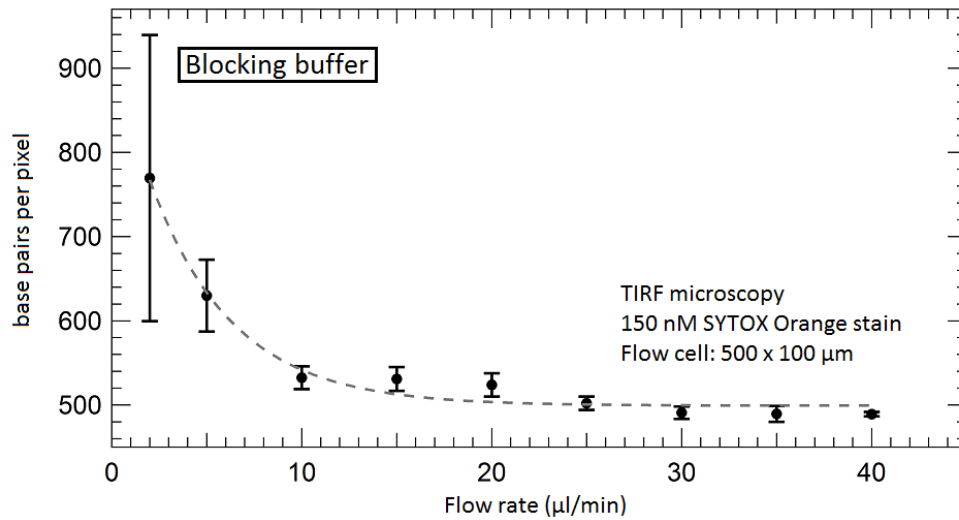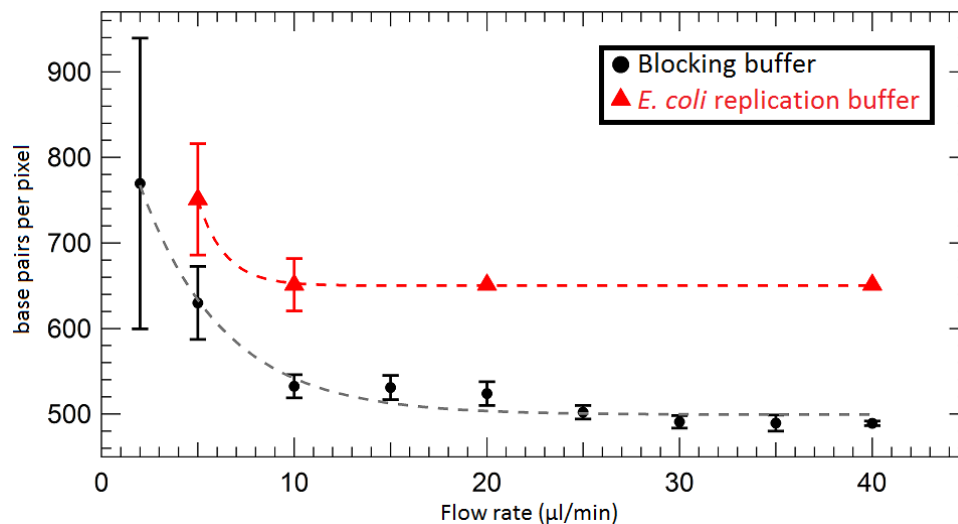*Figure 2.10:* *Conversion factor of number of base pairs per pixel of λ DNA as a function of flow rate (in µl/min) for experiments carried out in blocking buffer and* E. coli *replication buffer, showing a clear difference.*

2.3   Flow-stretched λ phage DNA length for different buffer solutions

This section describes the effect of the different buffers on the stretched-out length of λ phage DNA. As mentioned in the previous section, it was found that there is a significant length difference in fully stretched λ DNA when the experiment is performed in blocking buffer or *E. coli* replication buffer. Looking closer into the chemical composition of the buffers, it is clear that the *E. coli* replication buffer has 12 mM MgOAc while blocking buffer has none. The buffer compositions of often used buffers in the Van Oijen Lab are listed in Appendix A. It is found in literature that the divalent magnesium ions in solution has an effect on the negatively charged phosphate groups of the DNA backbone [54] [55]. This results in small local bending of the DNA backbone and hence shorter stretched-out DNA. To confirm this hypothesis, experiments of stretching λ DNA are done in different buffer

solutions. To make sure that the effect comes from the magnesium ions, a modified version of the *E. coli* replication buffer is made where the MgOAc was left out. This buffer is referred to as *E. coli* replication buffer (-), because it is related to the *E. coli* replication buffer, although the *E. coli* replication buffer (-) cannot be used in any replication experiments since magnesium ions play a critical role in replication [56]. Magnesium ions are required for both DNA polymerase and helicase activity, which are components of the replication machinery, as can be seen in section 3.1. The other buffers used in this study are T7 replication buffer with and without magnesium, i.e. (+) and (-), used for replication with T7 proteins, HU buffer used for HU experiments and the β buffer used for the β clamp experiment described in Chapter 3.

All experiments in this section are carried out at a flow rate of 10 µl/min in a 100 µm high and 500 µm broad flow cell. Again, 150 nM SYTOX Orange stain is used in combination with a green laser (532) with a laser power of around 19 W/cm^2 and an exposure time of 200 ms. In order to exclude any effects of the position in the flow cell on the stretched-out length (the flow profile differs when imaged near the edge or in the middle), all buffer are flown in one after another, without changing the camera position within the flow cell. Figure 2.11 shows the result of this buffer dependence test.
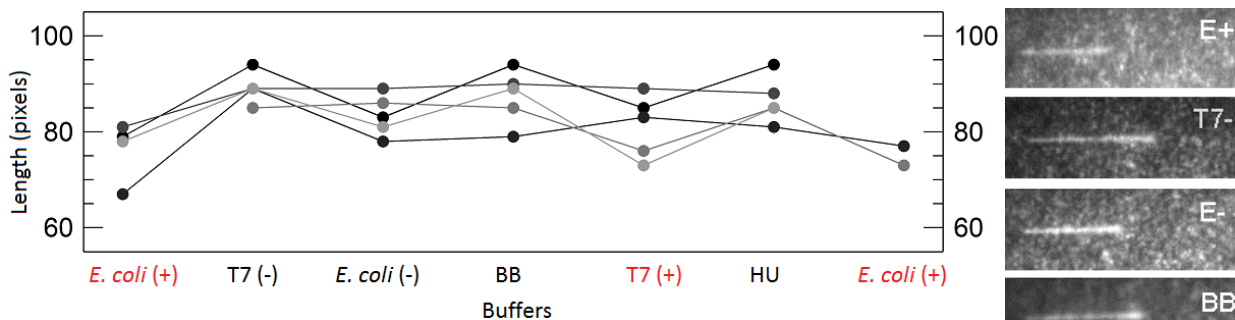
Figure 2.11: Buffer dependence test. Length (in pixels) as function of buffer at a flow rate of 10 µl/min. Connected dots indicate the same molecule undergoing length changes due to buffer changes. Buffers containing magnesium ions are depicted in red. Note that the experiment started and ended in E. coli *replication buffer with magnesium ions. The picture on the right shows microscope images of a single λ DNA strand, visually showing the increase and decrease in length upon buffer exchange.*

It is visible in figure 2.11 that the λ DNA molecules have a shorter stretched-out length in magnesium-ion-containing buffers than in buffers without magnesium. This is in agreement with the literature described above. This experiment is also performed in such a way that the buffers are exchanged in a different order, and the similar trend as in figure 2.11 was observed.

This is a proof of principle experiment, the presence of magnesium ions in buffer solutions is the main effect on decreasing the maximum stretched-out length of λ DNA in flow cell experiments. Other compositional elements might also play a role, but this is not investigated in this research project. There was also no significant relationship found between the pH of the buffers and the stretched-out length. In order to obtain more statistics, needed to make a valid conversion table for all buffers, a different experiment is performed. This experiment is performed in the same way as the above, except that the camera is used to scan various field of views along the channel. In order to keep the effect of the flow profile constant, this scan is performed in a direction with the flow on a fixed distance from both flow cell edges. Figure 2.8 shows the histograms of blocking buffer and *E.*

coli replication buffer (+), and figure 2.12 shows the histograms of two other buffers, out of which the mean values and errors are obtained by fitting a Gaussian. Again it is clear that the effect of adding magnesium ions is significant for the value of the stretched-out length.
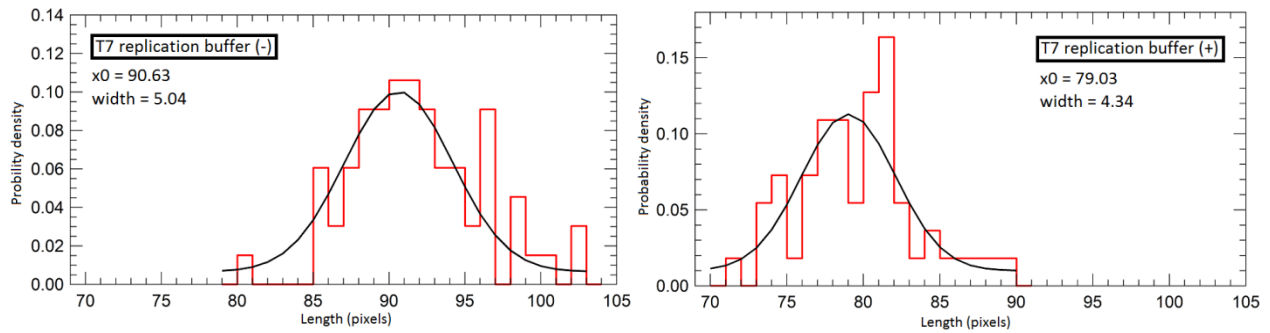
Figure 2.12: *Histograms of flow-stretched λ length distributions for measurements done in T7 replication buffer (-) and T7 replication buffer (+). The X-axis represents the length measured in pixels, the Y-axis represents the probability.*

Figure 2.13 shows the final result of the buffer dependence test that was performed by scanning along the flow cell to obtain more data. This figure combines the mean values and errors of figure 2.8 and 2.12 and the results obtained for the β buffer.
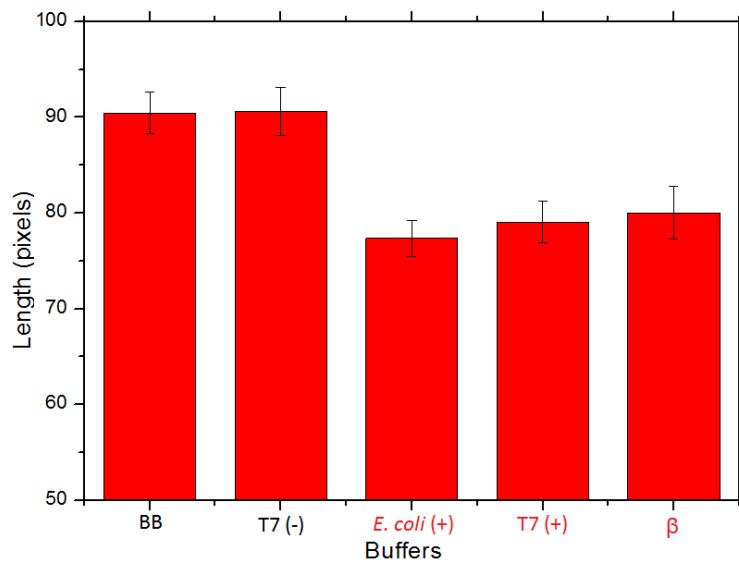
Figure 2.13: *Buffer dependence test. Length (in pixels) as function of buffer at a flow rate of 10 µl/min. Data points obtained from means and errors of histograms, not single DNA strands as in figure 2.11. Buffers containing magnesium ions are depicted in red.*

The results from the buffer dependence test of figure 2.13 is used to create the final conversion table for the length calibration of λ phage DNA in which the length and number of base pairs per µm are given as a function of both the flow rate and the buffer solution. This is done in the first approximation, in which a conversion factor with respect to blocking buffer for the different buffers can be applied on the length versus flow rate experiment done in blocking buffer. The final conversion sheet, which is printed and distributed in the Van Oijen Lab is shown in Appendix B.

2.4   Investigation of force profile along flow-stretched λ phage DNA

Since the λ DNA molecules are tethered to the surface by one end while the other end is loose within the flow cell, the molecules fluctuate a lot within the flow. Reason for this is that the DNA molecules are tethered to the surface where the flow is by definition zero. As illustrated in figure 2.3, the λ DNA molecule moves a bit above the surface. However, the flow profile there is still not the most desired one to nicely stretch out the DNA. Chapter 4 investigates a new technique to bring the DNA molecules up in the flow to decrease the undesired fluctuations, which disturb the precision of the measurements and require higher flow rates than would be necessary if the DNA molecules were places within the centre of the flow cell.

The fluctuations of the DNA at the surface are best visualized by making a Z projection (average intensity sum over al frames of the movie) over 2000 frames. This will give a more cone-shaped figure that shows that the tip of the DNA moves the most. Figure 2.14 shows such an image.

Figure 2.14: Average intensity sum over 2000 frames of a single λ DNA molecule at a flow rate of 10 µl/min, showing the cone-shaped figure of the DNA strand due to fluctuations because of flow. Yellow bars correspond to the data points in figure 2.15.

The main purpose of this section is to have some insight into the force profile along the flow-stretched λ phage DNA. The width of DNA in the Z projection is investigated by plotting a transversal line profile at places along the DNA, indicated by the yellow bars in figure 2.14, fitting this line profile with a Gaussian and plotting its full width at half maximum as a function of distance along the DNA. This is plot is shown in figure 2.15. The DNA is tethered to the surface at position 0 and the tip is at 80 pixels from the anchor point. The overall trend is definitely increasing, meaning that the fluctuation increase with the distance from the anchor point, as expected [51].
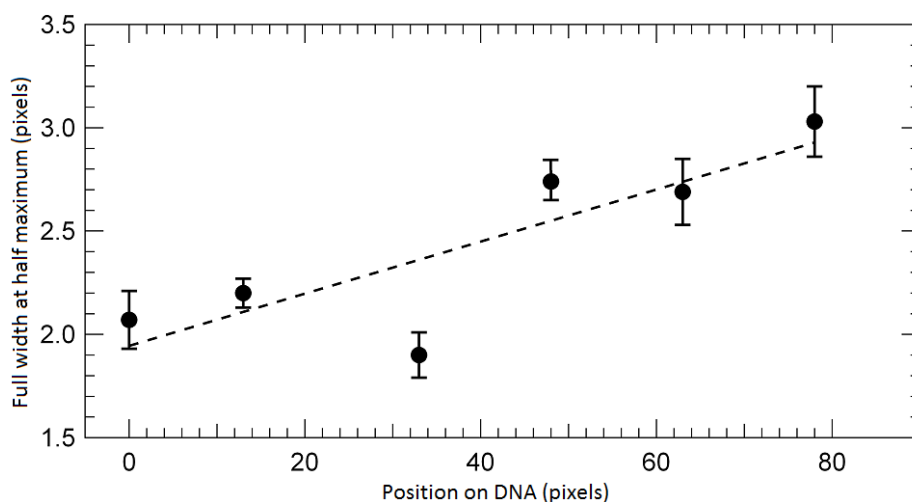

Figure 2.15: Full width at half maximum of Z projection as function of position along the DNA. The data points correspond to the yellow lines of figure 2.14. The dashed line is plotted to show the overall behaviour [51].

This is done for five other molecules and they all show the same increasing trend as in figure 2.15. The force exerting on the λ DNA molecule was estimated with the theory and formulas from [57]. The result is shown in figure 2.16. The fluctuation amplitudes used in the calculations are the values obtained from the linear fit and normalized to the amplitude at the DNA anchoring point.
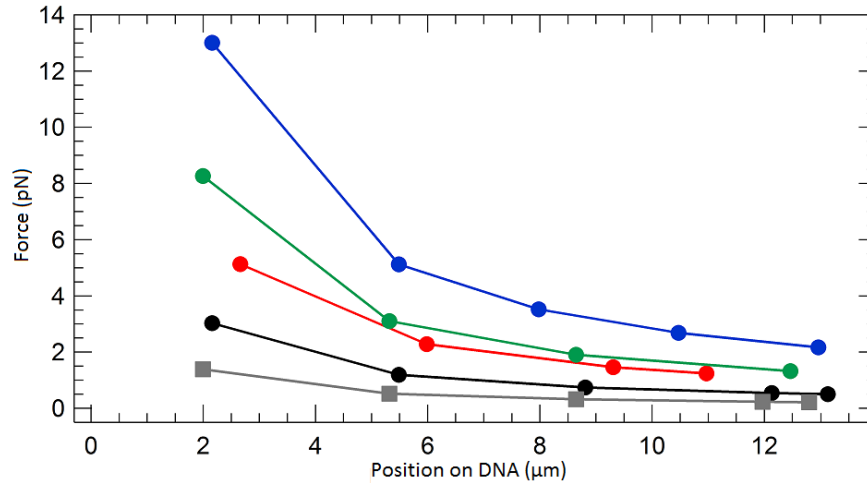
Figure 2.16: Force on stretched-out λ DNA, accounting for the fluctuations in the flow. The error bars are very large and not shows for clarity. Different colours represent different DNA molecules. Note that the force at the DNA position 0 is infinitely large, since this is the anchor point. The force at the tip of the DNA is the lowest, which is logical, since the fluctuations are the highest here, as can be seen in figure 2.15.

This measurement is definitely not the most accurate one. The best idea to tackle this problem would be to make a computer model and simulate this flow-stretched DNA. However, this is beyond the scope of thesis. The main goal here was to investigate the order of magnitude of the force profile along the DNA as visualized in figure 2.16, which is in the 1-12 pN regime.

2.5   Conclusion

The goal of this chapter was to calibrate the length of λ phage DNA for the fluorescence microscope setup in the Van Oijen Lab. It was found that there is a saturation behaviour for the flow-stretched length of λ phage DNA that is tethered to the bottom surface in a flow cell, which is in agreement with literature [51]. For the specific experimental conditions which are commonly used in the Van Oijen Lab, his maximum length is reached at flow rates between 10 and 20 µl/min for rectangular flow cells with dimensions of 100 µm height and 500 µm width. At saturation, the conversion factor for the microscope setup is around 650 base pairs per pixel. The experiments were carried out with SYTOX Orange as DNA stain.

It was found upon performing this experiment in blocking buffer and *E. coli* replication buffer that the type of buffer has a strong influence on the maximum stretched-out length of λ DNA molecules. Including more types of buffers, it was proven that the presence of divalent magnesium ions in the buffer solutions has a negative effect on the stretching of the DNA molecules. The reason for this can be found in the fact that the divalent positively charged magnesium ions could interfere with the negatively charged backbone of DNA, resulting in small bending of the DNA molecule which prevents it from

becoming fully stretched [54] [55]. Appendix B shows the conversion sheet obtained for the Van Oijen Lab, which shows the actual length and the conversion factor for the amount of base pairs per μm as a function of both the flow rate and the type of buffer.

At last, an attempt was made to investigate the force profile along flow-stretched λ DNA. Some rough approximation were made to show that this is in the order of 1-12 pN with the lowest force on the tip of the DNA. The reason for this is the fluctuations of the DNA molecule in flow due to the fact that they are tethered to the bottom of the flow cell where the flow is by definition zero. Chapter 4 investigates a solution to overcome this problem.

3. The role of *E. coli* β clamp in DNA replication kinetics

This chapter focuses on DNA replication. In particular, the role of the *E. coli* β clamp protein in DNA replication kinetics is investigated. The protein will be fluorescently labelled to track its motion during DNA replication in order to study and visualize its function. For cells to divide, the genetic material should first be replicated and as stated in Chapter 1, understanding this types of biological mechanisms in both health and disease can open new possibilities in drug design, diagnosis and disease control by preventing and curing diseases.

 E. coli is a gram-negative, rod-shaped bacterium of around 2 microns long and 0.8 microns wide. *E. coli* is known as the principal "guinea-pig" [58] of microbiologists and has been the subject of intensive research for more than 60 years. *E. coli* has a duplication rate of 30 minutes [59], the environmental requirements are simple and the full genome is sequenced [60]. For these reasons, *E. coli* and its replication machinery have been studied extensively. The *E. coli* replication machinery is simple compared to higher-order organisms, as it involves only 12 proteins. Various biochemical and biophysical research has been carried out during the last decades that lead to a clear picture of the bacterial replication mechanism. Therefore, this research project caries out DNA replication experiments in *E. coli*. In *E. coli*, the replication fork moves at a rate approaching 1000 nucleotides per second [61] and makes less than one mistake per 10^9 nucleotide incorporations [62]. Moreover, the fully functional replisome can be reconstructed *in vitro* with a limited number of purified key protein components [63]. For these reasons, *E. coli* is ideal for studying the dynamic interplay among the various components at the replication fork. The replication experiments described in this chapter are carried out *in vitro* at the single-molecule level, using TIRF microscopy and the in Chapter 1 described flow cell design. The main goal of this research project is to get a better understanding of the specific role of the β clamp, one of the proteins involved in DNA replication in *E. coli*.

 The first section will summarize the existing knowledge about the DNA replication machinery, i.e. the replisome, of *E. coli* and highlight all proteins involved in the process. The second section will explain how the β clamp is fluorescently labelled. The third section will describe the movement of the β clamp along ds-DNA. The fourth and fifth sections will describe the effect of the β clamp on M13 rolling-circle replication and the effect of the primase on the length of the Okazaki fragments formed during lagging-strand synthesis. The last sections will focus on conclusions and recommendations for future research.

3.1 Introduction to DNA replication mechanism

As stated above, this section will focus on the *E. coli* replisome, which is a multiprotein apparatus that replicates the parental ds-DNA into two identical daughter ds-DNA molecules. The fundamental components of the replisome are conserved across viruses and bacteria. All replisomes include a helicase to unwind the ds-DNA, two or more polymerases to synthesize the new strands of DNA, and a clamp loader to organize the complex on the DNA. The replication proteins assemble at a specific site within the genomic DNA, the so-called origin of replication, and form a replication fork. Here, the ds-DNA is separated into two individual strands by the helicase and both are subsequently copied in the 5' to 3'direction of the DNA [64]. Figure 2.3 shows such a replication fork. The major role of the replisome is to coordinate the reactions mediated by the proteins of leading- and lagging

strand DNA synthesis [65]. For example, the unwinding of DNA by the helicase in order to expose ss-DNA templates occurs at the same rate as the polymerization of nucleotides by the polymerase. In other words, the unzipping of the double helix of DNA happens at the same rate as making the complementary strands for the created ss-DNA. Therefore, there is a clear association between the two proteins. Figure 3.1 shows a model of the replication fork of *E. coli*, indicating all proteins involved in DNA replication.
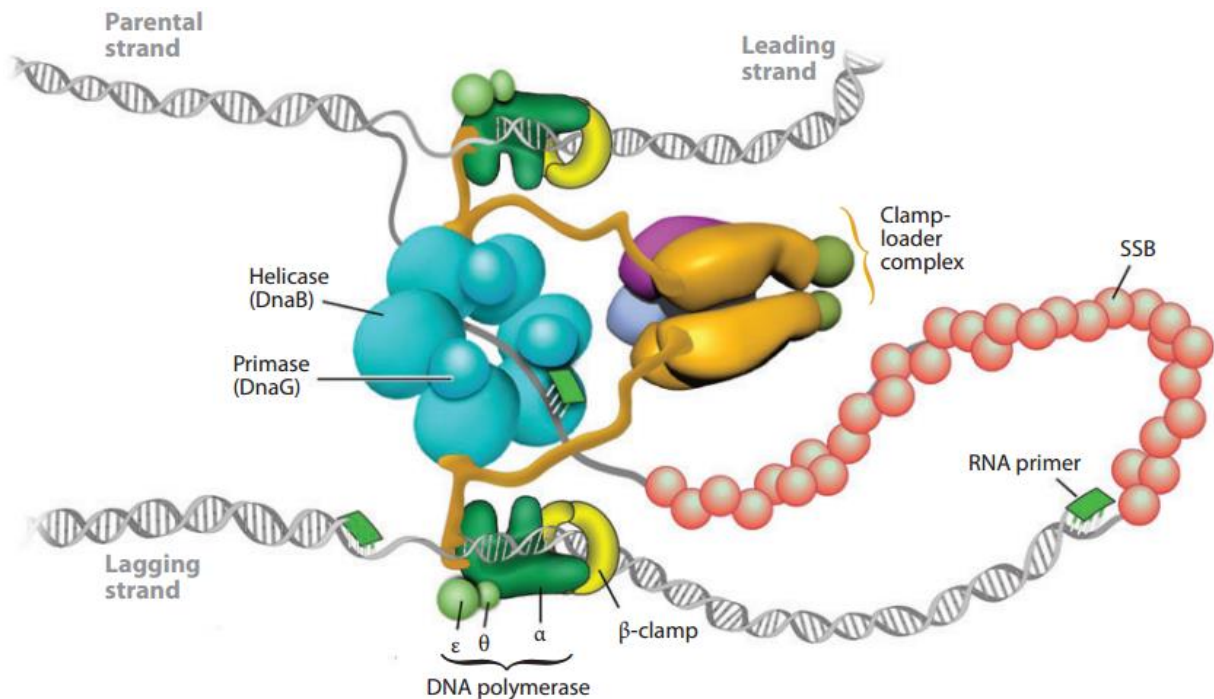
Figure 3.1: Model of the replication fork of E. coli*. Figure source: [65].*

The DnaB protein is a hexameric protein that encircles one strand of the parental DNA strand. This helicase uses energy from ATP (adenosine triphosphate) hydrolysis to separate the duplex DNA into two daughter strands by moving along the parental DNA in the 5' to 3' direction, i.e. from right to left in figure 3.1. DnaB is often associated with DnaC, which loads DnaB. After loading DnaB, DnaC is released. This interaction between DnaB and DnaC requires energy from ATP hydrolysis [66].

The DNA polymerase III (Pol III) holoenzyme (complete complex containing all the subunits needed for activity) consists of three assemblies: the Pol III core, the β clamp and the clamp-loader complex. The Pol III core consist of three subunits: α, the DNA polymerase, ε, a proofreading 3' to 5' exconuclease and θ, which stimulates ε [67]. The proofreading exconuclease is the first line in defence in correcting errors made by the DNA polymerase by removing the incorrect nucleotides copied by the DNA polymerase.

The β clamp is a ring-shaped dimer that is loaded onto the DNA by the clamp-loader complex. Figure 2.3 shows the crystal structure of the β clamp. The two β subunits are assembled around the DNA via ATP hydrolysis. Once bound to the DNA, the β clamp can slide along the DNA strand. The β clamp regulates switching between polymerases, as it has a high affinity for binding the DNA polymerase. The dissociation constant K_d for interaction of the Pol III core with the β clamp is approximately 1 nM [67]. Therefore, the β clamp contributes to the high processivity of the polymerases by keeping them close to the DNA template [68].

Figure 3.2: Crystal structure of β clamp. Figure source: [69].

The clamp-loader complex in this study consists of the $\tau_3\delta\delta'\chi\psi$-subunits. These five subunits are required for clamp loading and coordination of the different enzymatic activities at the replication fork [63]. The τ -subunits bind the DNA polymerase cores with the helicase via its carboxyl terminus, effectively trimerizing the polymerase at the replication fork [70]. It organizes the replisome by simultaneously binding the α-subunit with DnaB. The τ subunit can be replaced by the smaller γ subunit, but since all research carried out in this research project makes use of the $\tau_3\delta\delta'\chi\psi$ clamp-loader complex, no further details about this is discussed. The δ-subunit is responsible for binding the β clamp and the δ'-subunit induces ATPase activity within the clamp-loader complex [68]. The χ- and ψ-subunits induce binding to SSB (single-stranded binding protein) and facilitate lagging-strand DNA replication [71]. ss-DNA is prone to chemical and nucleolytic attacks that can damage it and produce breaks that are difficult to repair [72]. In order to protect this fragile ss-DNA, SSB binds to it with high affinity and in a sequence-independent manner [73]. SSB prevents formation of any secondary structures that may inhibit synthesis [74].

As described above, the helicase unwinds the parental DNA strand and creates two ss-DNA daughter strands. The two DNA polymerase complexes subsequently synthesise a complementary DNA strand on each of these two single-stranded templates. However, the DNA polymerases can only add nucleotides to a primer in the 5' to 3' direction, while the single-stranded daughter strands are of opposite polarity. The leading-strand polymerase synthesizes in a continuous fashion while following the helicase [75]. The synthesis of the lagging-strand is more complex and discontinuous. The lagging-strand polymerase cannot continuously synthesize this strand while following the helicase, because the lagging-strand is of opposite polarity and the polymerase cannot add nucleotides in the 3' to 5' direction. As a result, the lagging-strand polymerase synthesizes short fragments discontinuously in the 5' to 3' direction [76]. These short fragments are referred to as Okazaki fragments, after the discovery by Sakabe & Okazaki in 1966 [77]. Initiation of each Okazaki fragment requires an RNA primer of 10 to 12 nucleotides long, synthesized by the DnaG primase (see figure 3.1) [78]. The primer is held in place by the primase until it is transferred to the lagging-strand polymerase to initiate the synthesis of the Okazaki fragment. These Okazaki fragments are around 1-2 kilobase pairs long [64]. As stated above, the unzipping of the double helix of DNA happens at the same rate as synthesizing both complementary strands, i.e. the leading- and lagging-strand are synthesized simultaneously. In order to coordinate lagging- with leading-strand synthesis, Alberts *et al.* [79] proposed the "trombone model" in which a loop is formed to reorient the lagging-strand DNA so that the lagging-strand polymerase can replicate it in parallel with the leading-strand polymerase. This loop is illustrated in figure 3.1. During each cycle of Okazaki fragment synthesis, this replication loop grows and shrinks

(is released) like the slide of a trombone. Single-molecule techniques, using TIRF microscopy, gave indirect evidence for these loop formations in the T7 bacteriophage replisome [80]. However, experimental proof for the *E. coli* system is not found yet. Figure 3.3 is an animated figure showing the growing and releasing cycle in lagging-strand synthesis.
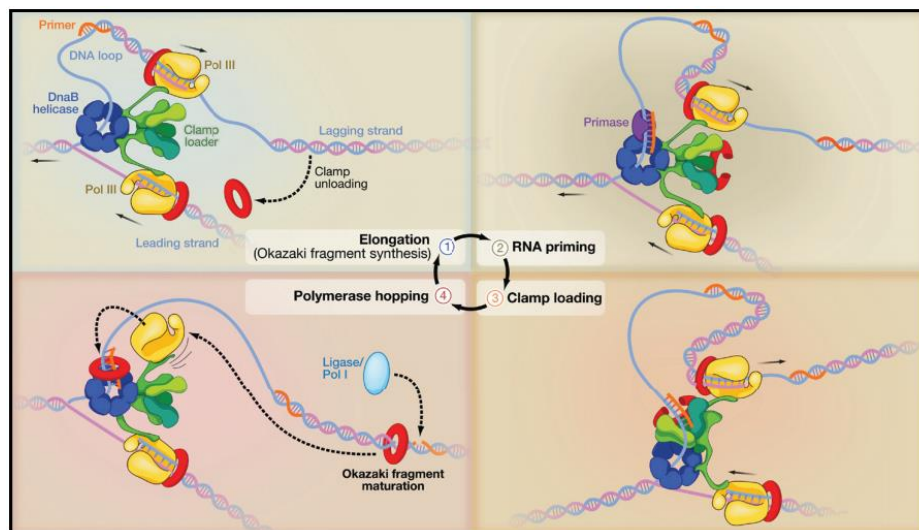
Figure 3.3: Lagging-strand cycle. Clockwise from upper left image: 1. Okazaki fragment synthesis, loop growth. 2. Primase synthesizes RNA primer near the replication fork. 3. Clamp-loader assembles new β clamp around the RNA primer. 4. Polymerase hops to new β clamp, loop release, and starts formation of new Okazaki fragment. Ligase connects formed Okazaki fragment to the Okazaki fragment formed the cycle before by replacing the RNA primer with DNA. As a result, a continuous chain of DNA is formed. Figure source: [64].

The last components involved in the DNA replication process are the deoxyribonucleoside triphosphates (short: deoxyribonucleotides, abbreviated: dNTPs) and the ribonucleoside triphosphates (short: ribonucleotides, abbreviated: NTPs). Figure 3.4 illustrates the chemical structure of the dNTPs and NTPS. Both consist of a triphosphate group, a sugar (deoxyribose or ribose) and a base. For the deoxyribonucleotide, these bases include adenine (A), cytosine (C), guanine (G) and Thymine (T). Hence, the dNTPs consists of dATP, dCTP, dGTP and dTTP. These dNTPs are the building blocks of DNA. For the ribonucleotide, the bases include adenine (A), cytosine (C), guanine (G) and uracil (U). Hence, the NTPs consists of ATP, CTP, GTP and UTP. These NTPs are the building block of RNA, i.e. the primer formation at the start of every Okazaki fragment [81].
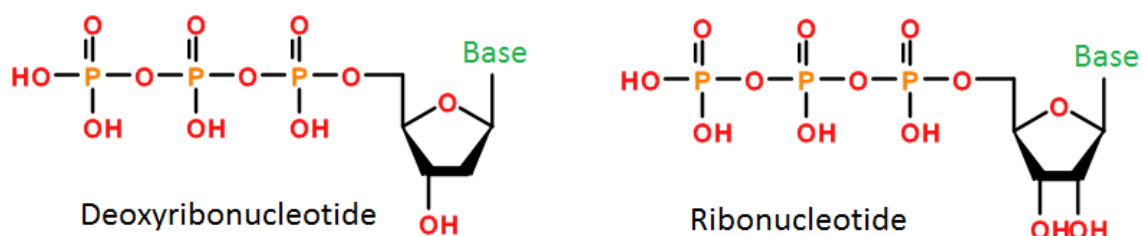
Figure 3.4: General chemical structure of a deoxyribonucleotide as basis for dATP, dCTP, dGTP and dTTP (left) and a ribonucleotide as basis for ATP, CTP, GTP and UTP (right).

3.2   Fluorescent labelling of β clamp

As described in the introduction of this chapter, the main goal of this research project is to get a better understanding of the specific role of the β clamp in DNA replication. The previous sections showed how the β clamp is involved in the DNA replication machinery. The clamp-loader complex opens and loads the dimeric β clamp onto the DNA, and the β clamp has a high affinity for binding the DNA polymerase. Since the β clamp can slide along the DNA, the main contribution of the β clamp is that it keeps the DNA polymerase close to the DNA, so that it can copy the parental strand. In order to track single β clamps during DNA replication using a TIRF setup, the β clamps need to be fluorescently labelled. In this research, this is done in two ways, as described below. Moreover, various different fluorescent dyes are used. The experiments in this research are carried out using the dual-view mode of the microscope setup. This means that the camera can show two images, corresponding to the signal from two different colours of lasers simultaneously. This is a useful feature to image the DNA molecules and the fluorescently labelled β clamps at the same time. One problem that might occur, is cross-excitation. In that case, the DNA stain or fluorophore label of the β clamp might be visible in both channels, making it impossible to conclude where the signal came from in the first place. In order to prevent this problem, the β clamp is labelled with either blue or red dyes, which can be used in combination with red or blue intercalating fluorescent DNA stains. The big distance within the spectrum between red and blue makes it possible to exclude these cross-excitations. The labelling has been performed using the protocol written in the supplementary materials from Tanner *et al.* [82]. A more general description of how this is carried out in this research is written below.

The β clamp has multiple amine groups. However, both subunits of the β clamp have only one N-terminal amine group and by using a lower pH of only 7.6, the labelling should only take place at the N-terminal amines. Therefore, an attempt was made to synthesize a fluorescent dye onto the β clamp, using an amine-reactive NHS-fluorophore (*N*-Hydroxysuccinimide, IUPAC: 1-hydroxy-2,5-pyrrolidinedione). This reaction is illustrated in figure 3.5.

Figure 3.5: Amine-NHS labelling of β clamp with a florescent dye.

The dyes used were Atto488 (maximum absorption/emission at 501/523 nm) and Cy5 (649/670 nm). At first, the protein stock was dialyzed into PBS (137 mM NaCl, 2.7 mM KCl, 10 mM Na_2HPO_4, 1.8 mM KH_2PO_4, pH = 7.6) in order to get the proteins into an amine-free buffer. This is done to prevent the NHS-fluorophores to bind in large excess to the free amines in the buffer, instead of to the β clamp. The protein and dye were mixed with a 10-fold excess of the dye, wrapped in aluminium foil to protect the dye and kept on a stirring plate at 4 °C for four hours. After this, the mixture was run twice through a spin desalting column in order to remove free dye and stored in a storage buffer (160 mM KCl, 10% glycerol, 0.1 % triton, 40 mM HEPES, 5mM DTT). To see if this labelling was successful, a protein gel was run. Figure 3.6 shows the result, clearly showing a high concentration of

labelled β clamp. The proteins moved due to the applied potential gradient, carrying the fluorescence with it and indication successful labelling.
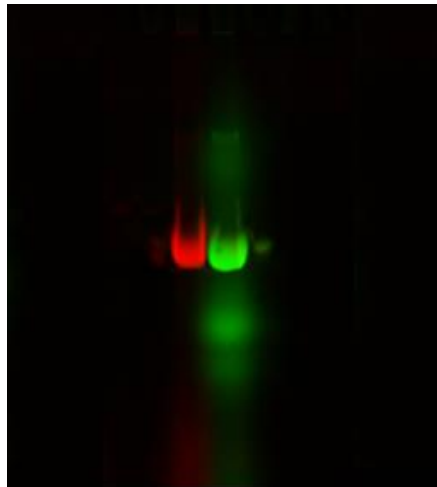
However, this does not give any information about the functionality of the protein. Labelling requires a covalent bonding with a specific side of the molecule and might interfere with its function. For example, adding the fluorescent label to the β clamp might make it impossible to bind the polymerase and hence cannot be used in replication experiments. The fluorescent molecules themselves are seldom directly harmful to cellular processes, but their fusion with proteins can perturb the native function of the target protein. The binding interfaces of proteins are often highly specific for interaction with other proteins, and the introduction of a bulky fluorescent protein can sterically interfere with these binding interactions [83]. However, there is no easy functionality assay available for the β clamp, as it has no enzymatic activity readout. The single-molecule diffusion and replication assays described in the upcoming sections will proof if the β clamps are still functional or not.

The goal is to obtain a high labelling efficiency, i.e. to have as much as β clamps with a fluorophore as possible. For this reason, the incubation of the protein with the fluorophore is done in great excess of the dye. In theory it is possible to over-label the β clamp, because each protein has two binding sites available where a fluorophore can attack. Since this might create even bigger functionality issues, the attempt was made to reach but not exceed a 100 % labelling.

The second labelling method used in this research is cysteine-maleimide labelling. The β clamp has four cysteines per monomer, i.e. eight cysteines per full dimer [84]. The reaction of a cysteine of the β clamp with a maleimide-fluorophore is illustrated in figure 3.7. This labelling method is performed using the following dye molecules: Alexa Fluor 488 (495/519 nm), Alexa Fluor 647 (650/665 nm) and Cy5 (649/670 nm). The labelling procedure is carried out in the same way as the amine-NHS labelling described above. The only difference is that the protein stock was dialyzed into the storage buffer without any DTT. This is done to prevent binding of the maleimide-fluorophores to the thiol groups of DTT. After incubation and running a spin desalting column twice to remove free dye, 5mM of DTT was added for storage purpose.
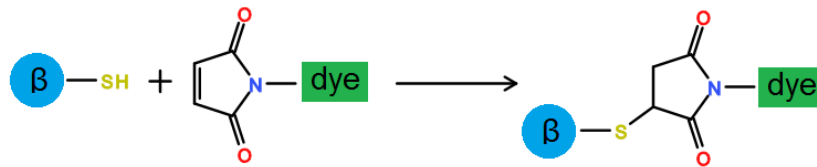
Figure 3.7: *Cysteine-maleimide labelling of βclamp with a fluorescent dye.*

A NanoDrop™ Spectrophotometer was used to determine the labelling efficiencies. Incubation of the β clamp with Cy5 in a ratio of 1:10 resulted in a labelling efficiency of around 12.9 %. Preforming the incubation with Alexa488 in a ratio of 1:20 resulted in a efficiency of around 25.6 %. The highest efficiencies were achieved when incubating the β clamp with the Alexa647 in a ratio of 1:10 and 1:20, which gave labelling efficiencies of around 39.7 % and 90.4 % respectively.

The following sections describe how these cysteine-maleimide labelled β clamps are used in various experiments. Section 3.3 describes the movement of the β clamp along doubly-tethered, double-stranded DNA. Section 3.4 and 3.5 describes the visualization of the β clamp in M13 rolling-circle replication experiments.

3.3   Movement of β clamp along doubly-tethered, double-stranded DNA

The main goal of this section is to see if the labelled β clamps can be visualized when they bind and slide along ds-DNA. As described in section 3.1, the β clamp does not bind the DNA using direct chemical bonding, but it binds by encircling the DNA strand, i.e. through so-called topological binding [69]. As a result, the β clamp slides along the DNA via diffusion. This diffusion turned out to be bidirectional and does not require ATP, as the β clamp has no ATPase site [85]. It was found that the β clamp has a high affinity to binding circular DNA templates, but almost no affinity to binding onto linear DNA [85]. It actually has the same affinity, but almost no affinity is found, because the β clamp can dissociate from a linear DNA strand by sliding off the end. However, using a circular DNA template is inconvenient for doing the flow-stretched single-molecule studies described in the previous chapters. Therefore, a linear λ phage DNA template with biotin ligated at both ends is used in this study. This is done in a similar fashion as described in section 2.1. Figure 3.8 shows this λ DNA construct.

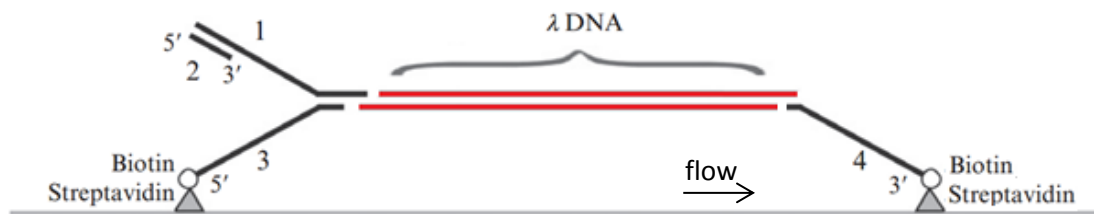*Figure 3.8:* *Illustration of the λ DNA construct used in this study. Oligo 1 forms the fork arm, oligo 2 the leading-strand primer, oligo 3 the biotinylated fork arm and oligo 4 complements the construct with a second biotin. Figure adapted from [48].*

This construct forms a sort of bridge within the flow cell and contains a fork arm where the clamp-loader complex can come in and load the β clamp onto the ds-DNA template. After

loading, the bridge-shape of the construct prevents the β clamp from sliding off and the diffusion of the β clamp along the DNA should be visible.

The experiment is performed in the same rectangular flow cell of 100 μm high and 500 μm broad as mentioned in Chapter 2. Here, the double-tethered ds-DNA bridges are created by flowing in 17.5 pM of the above λ DNA constructs in blocking buffer. 150 nM YO-PRO-1 stain is used to visualize the DNA bridges. YO-PRO-1 is a DNA stain with excitation and emission maxima at 491 nm and 509 nm respectively. Note that for all experiments in this chapter, the buffers are degassed to prevent air bubbles in the flow cell that break the DNA constructs and that all buffers are heated to 37 °C, which is needed for *E. coli* proteins to work. The microscope setup contains a heater to keep the flow cell at 37 °C. In order to have nicely stretched-out bridges, the DNA molecules are flown in at a high flow rate of 100 μl/min. This high flow rate is required, because the λ DNA construct should first bind the streptavidin-functionalized surface with one biotin and then be highly stretched out before binding with the second biotin. At lower flow rates, this will result in having the binding sides in closer proximity and hence no linearly stretched-out DNA templates. The intercalating nature of the DNA stains, as discussed in the previous chapter, slightly elongate the DNA. Hence, it is important that the DNA stain is already introduced in the first step, to make the DNA bridges as stretched-out as possible.

After tethering the DNA to the surface, a wash solution of β buffer (see Appendix A) with 150 nM YO-PRO-1 is used to wash out unbound DNA. This washing step is done at a 'normal' (as discussed in Chapter 2) flow rate of 10 μl/min. This wash step also has the purpose to change the blocking buffer into the β buffer, which is needed for loading the β clamp [56]. For this purpose, the *E. coli* replication buffer is suitable as well. However, the β buffer is created by slightly modifying the *E. coli* replication buffer, which gives a little bit better microscope contrast using blue and red DNA stain. The doubly-tethered DNA bridges are visualized with a 488 nm laser, using a power density of 3.24 W/cm^2. Figure 3.9 is an example of how these DNA bridges look like.
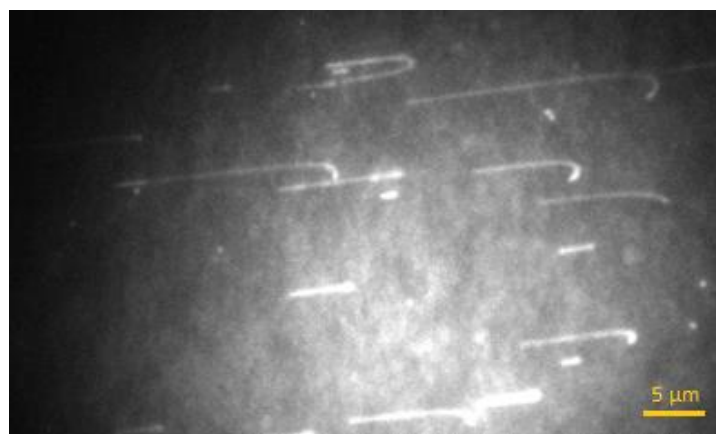
Figure 3.9: TIRF microscope image of doubly-tethered λ DNA constructs, stained with YO-PRO-1. Flow is coming in from the left at a flow rate of 10 μl/min. This image is an average intensity sum over 100 frames, with an exposure time of 500 ms.

Figure 3.9 shows that most doubly-tethered DNA constructs are not fully stretched. This results in the formation of small loops and molecules that wobble slightly in the flow. However, the flow does stretch out the molecules as much as possible and the second biotin still makes sure that the β clamp cannot slide off the DNA strand.

After the wash step, the protein mixture was flown in. This protein mixture contains 15 nM clamp-loader complex, 1 mM ATP and around 30 nM Cy5-labelled β clamp in β buffer. 150 nM YO-PRO-1 stain is added as well, to keep the DNA visible when imaged in dual view mode. As described in Chapter 1, reactive oxygen species can induce photobleaching of fluorophores. When oxygen collides with the fluorescent molecule in its excited state, it quenches the fluorescence by trapping it into a triplet state, which is not fluorescent. Therefore, an oxygen scavenger system is added to the protein mixture when it contains fluorescently labelled proteins. The oxygen scavenger system introduced contains 1 mM trolox (IUPAC: 6-hydroxy-2,5,7,8-tetramethylchroman-2-carboxylic acid), 40 mM glucose, 250 nM glucose oxidase, 64 nM catalase and 10 mM DTT. Trolox is an excellent triplet state quencher, suppresses blinking and stimulates long-lasting emission in combination with an enzymatic oxygen-scavenging system [86]. The most popular enzymatic oxygen-scavenging system is the combination of glucose, glucose oxidase and catalase [87]. Glucose oxidase and catalase remove molecular oxygen by oxidizing glucose. DTT is a strong reducing agent and in combination with specific salt conditions, it can be used to prevent blinking of the dye and to produce a brighter signal [38].

In dual view mode, the DNA constructs and the Cy5 dyes can be visualized simultaneously. For visualizing the Cy5-labelled β clamps, a 647 nm laser with a power density of 19.2 W/cm^2 is used. Figure 3.10 shows the result of flowing in labelled β clamps.
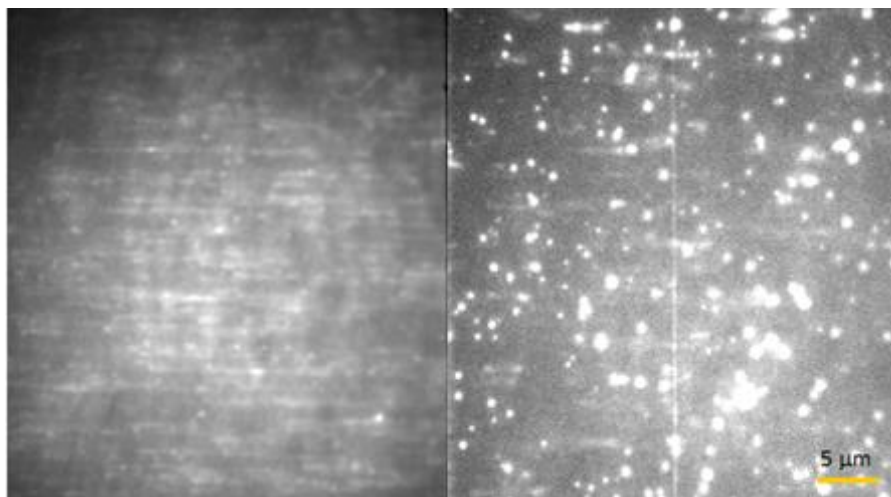
Figure 3.10: TIRF microscope image of doubly-tethered λ DNA constructs, stained with YO-PRO-1 (left channel) and Cy5-labelled β clamps (right channel). Flow is coming in from the left at a flow rate of 10 μl/min. This image is an average intensity sum over 50 frames, with an exposure time of 200 ms.

As can be seen in figure 3.10, the Cy5 channel shows clearly signals correlating to the fluorescently stained DNA in the YO-PRO-1 channel, meaning that the β clamps do bind to the doubly-tethered ds-DNA construct. As mentioned in the previous section, no cross-excitations can occur when YO-PRO-1 is used in combination with Cy5.They are too far apart in the spectrum. Hence, figure 3.10 shows no artefact. Figure 3.11 shows another field of view of the same measurement. Here the 488 nm laser is switched of. The same pattern is observable for the Cy5 channel, indicating that the visible signal is indeed due to the Cy5 molecules and no leak-through from the YO-PRO-1 stain into the Cy5 channel. This is a direct proof that there is no leak-through. As indicated in figure 3.10, not all DNA molecules have correlating signals in the Cy5 channel. If there was leak-through, all DNA visible in the YO-PRO-1 channel should have been visible in the Cy5 channel as well. Another point is that

these figures show that the β clamps are bound to the DNA by the clamp-loader complex and not by nonspecific binding to the DNA. If they would nonspecifically bind, i.e. stick to the DNA, they will not diffuse along the DNA. In that case, the signals in the Cy5 channel will indicate multiple β clamps stuck to one single DNA construct. Since this will be a stochastic process, it is impossible that some DNA molecules will have a lot of β clamps, while others will have none.
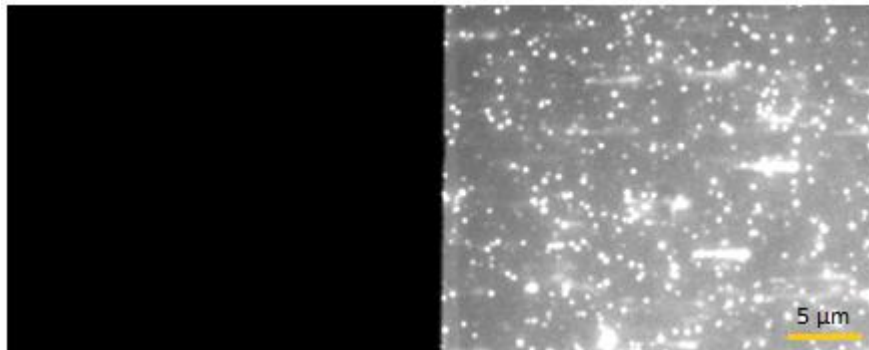
Figure 3.11: TIRF microscope image of doubly-tethered λ DNA constructs, stained with YO-PRO-1 while the 488 nm laser is switched off (left channel) and Cy5-labelled β clamps (right channel). Flow is coming in from the left at a flow rate of 10 µl/min. This is an average intensity sum over 50 frames, with an exposure time of 200 ms.

As stated above, the β clamps are indeed loaded by the clamp-loader complex and not bound nonspecifically. However, this leaves two possible explanations for the stripes visible in the Cy5 channel of figure 3.10 and 3.11. The first possibility is that the β clamps diffuse really fast and since both figure are average intensity sums over 50 frames (because it makes the image more clear), this could smear out the signal. The other possibility is that the clamp-loader complex is the limiting factor for loading β clamps on all DNA products. In that case, it is a more 'all or nothing approach', in the sense that if the clamp-loader complex *can* bind to the forked arm of the construct and load a β clamp, this can happen multiple times and hence result into multiple β clamps loaded onto a single DNA molecule. However, if the clamp-loader complex *cannot* bind to the forked arm, no β clamps can be loaded on that DNA strand. The best way to check if the fluorescently labelled β clamp is diffusing along the DNA is by making a kymograph. A kymograph is a picture that shows how a spatial position evolves over time by having a spatial axis represent the time. Figure 3.12 shows kymographs of the β clamp(s) bound to two DNA strands. These figures match figure 3.10 and 3.11.
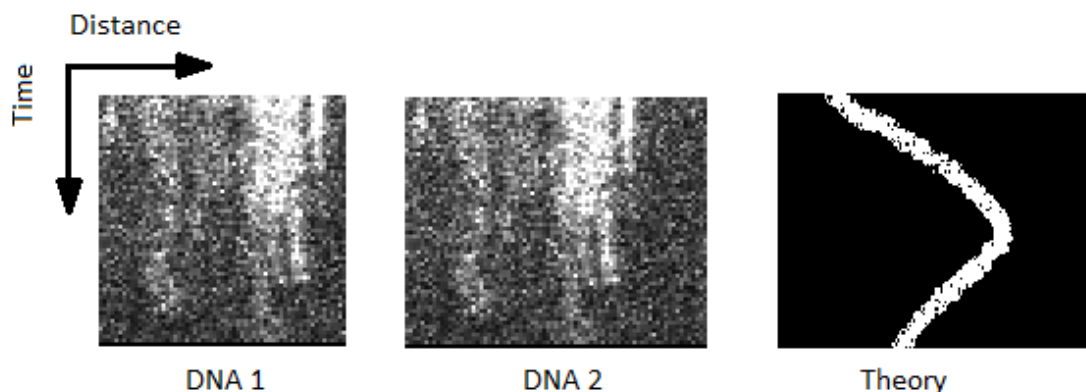
Figure 3.12: Kymographs of the Cy5 channel showing the β clamp(s) move in time along two different DNA strands. The right image shows how a kymograph should look like when a single β clamp diffuses to the right and bounces back upon reaching the end of the DNA construct.

Figure 3.12 shows no single β clamp diffusing along the doubly-tethered ds-DNA construct. It appears to be stationary and it seems like there are indeed multiple β clamps loaded onto each construct. However, the above measurements are imaged with an exposure time of 200 ms. Since there is still the possibility that the β clamps move to fast to be observed, experiments are done in which the exposure time was decreased tremendously, down to 11 ms. Still, no kymographs showed movement of just a single β clamp. Kochaniak *et al.* [88] determined the diffusion constant of a PCNA sliding clamp along DNA, which is tetrameric ring which binds DNA polymerase in eukaryotic cells and moves in a similar fashion as the β clamp. They found that the arithmetic mean value of the diffusion constant is 1.16 ± 0.07 μm^2/s. Diffusion coefficients of this order should have definitely been visible at the low exposure times used in this study.

This result proves that indeed either multiple or no β clamps bind to the DNA bridges. This is proof of the 'all or nothing approach' where the limiting factor upon clamp-loading is the association of the clamp-loader complex with the DNA construct. Multiple β clamps can be loaded onto the DNA construct if the clamp-loader complex can load to the DNA. No β clamps will be loaded onto the DNA construct if the clamp-loader complex cannot load to the DNA. This result is later confirmed by Slager [89], who introduced a nicking enzyme to create more binding sites for the clamp-loader complex with the DNA template. As a result, a better distribution of β clamps over all DNA constructs was obtained and the diffusion coefficient of a single β clamp on one ds-DNA template was obtained.

The main contribution of these experiments to this study is that it showed that the fluorescent labelling of the β clamps did not interfere with its function upon binding to ds-DNA. The affinity with the clamp-loader complex is still intact. The next section will show how these labelled β clamps can be used in M13 rolling-circle replication experiments. This will gain insight into its motion during DNA replication, which is the goal of this research project.

3.4 M13 rolling-circle replication experiments with fluorescently labelled β clamp

This section shows single-molecule DNA replication experiments with the *E. coli* proteins described in section 3.1, including the fluorescently labelled β clamp. The main goal of this research is to obtain insight into the role of the β clamp in the DNA replication machinery. This project uses the M13 rolling-circle template to do replication experiments. Just like λ phage, M13 is a bacteriophage out of which the DNA template can be isolated and used in replication studies. Since section 2.1 is quite elaborate about λ phage, its purification and its life cycle, no further information is given here. The M13 plasmid, i.e. a small DNA molecule that is physically separated from and replicated independently of chromosomal DNA, is a circular ss-DNA template of 6407 base pairs long [90]. The M13 template is constructed by annealing a biotinylated 66-mer oligonucleotide to the plasmid and filling in the circle to get ds-DNA, as described in [91].

DNA replication experiments with the M13 plasmids are performed by a rolling motion of the circular ss-DNA template and copying the 6407 base pairs of the template. Moreover, multiple copies of the template can be made. An analogy can be made with a paint roller, which rolls over a surface and prints the same pattern every time it makes a complete rotation. Figure 3.13 shows how this rolling-circle M13 replication works. At the 3'

end, the red circular template can be copied continuously. As a result, the template rotates clockwise. The complementary template strand will then be copied discontinuously, i.e. with the formation of Okazaki fragments, by the polymerase (which reads 5'-3'). This is shown by the blue arrows. Hence, leading-strand synthesis takes place at the circular head of the construct and lagging-strand synthesis takes place at the tail between the circle and the anchor point. In the single-molecule studies presented here, using a TIRF setup, replication is visualized by staining the DNA and imaging the length of the product as the replication proceeds. When replication takes place, the products grow and will be stretched-out due to the flow, as shown in the kymographs of figure 3.15.
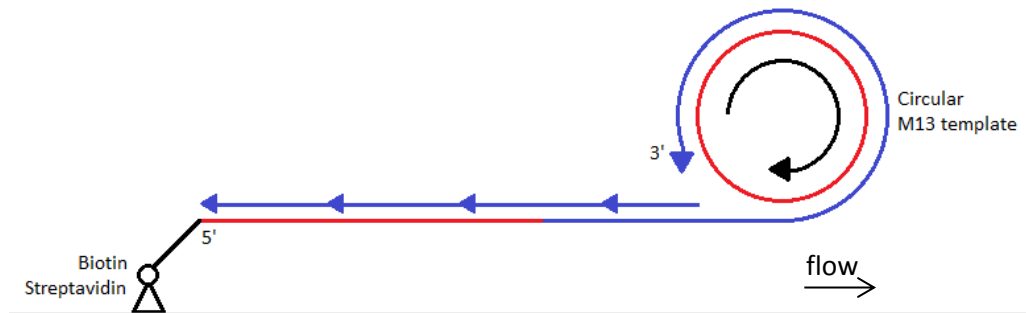
Figure 3.13: *Animated figure of M13 rolling-circle replication. The single-stranded circular template is copied at the 3' end. As a result, template rotates clockwise as indicated by the black arrow. The complementary template strand is copied discontinuously via the formation of Okazaki fragments as indicated by the blue arrows to the left.*

The replication experiments are carried out with the same type of flow cell as discussed in the previous section. The experiment is performed by first flowing in 5.3 pM biotinylated M13 templates with 150 nM of YO-PRO-1 stain in blocking buffer. Figure 3.14 shows how this looks under the microscope under exposure (200 ms) of the 488 nm laser (32 W/cm^2). The M13 template are visible as bright spots.

Figure 3.14: *TIRF microscope image of biotinylated M13 templates binding to the streptavidin-functionalized glass coverslip. This image is a single frame, taken with an exposure time of 200 ms.*

After a wash step, i.e. flowing in 150 nM of YO-PRO-1 in β buffer to change to the buffer required for replication and to wash out all M13 that did not bind, the replication mixture is flown is. This replication mixture contain all replication proteins as described in section 3.1 and the oxygen scavenger system introduced in section 3.3. This is required for stabilization of the fluorescence signal from the labelled β clamps. Appendix C shows the literal protocol

of all concentrations required to form this replication mixture. The only remark here is that the standard replication protocol in the Van Oijen Lab requires 30 nM of β clamp. However, in this experiment it is adjusted to around 14 nM or even lower. The reason for this is that high concentrations of β clamps also introduce high concentrations of fluorophores, which give an extremely bright signal that saturates the camera and makes detection of single β clamps impossible. However, concentrations that are way lower turned out to decrease the replication yield too much.

The experiment showed that it takes around 20 minutes, at a flow speed of 10 μl/min, before replication starts. Moreover, not all M13 templates undergo replication, in fact the majority (around 95 %) of the surface-bound M13 templates does not replicate at all. In a multi-protein process like this, this is expected. Like the experiments performed in section 3.3, the imaging is done in dual view mode with one channel showing the YO-PRO-1 stain of the DNA and one channel showing the β clamps. Figure 3.15 shows various kymographs of M13 replication, i.e. growth with respect to time, in the YO-PRO-1 channel.
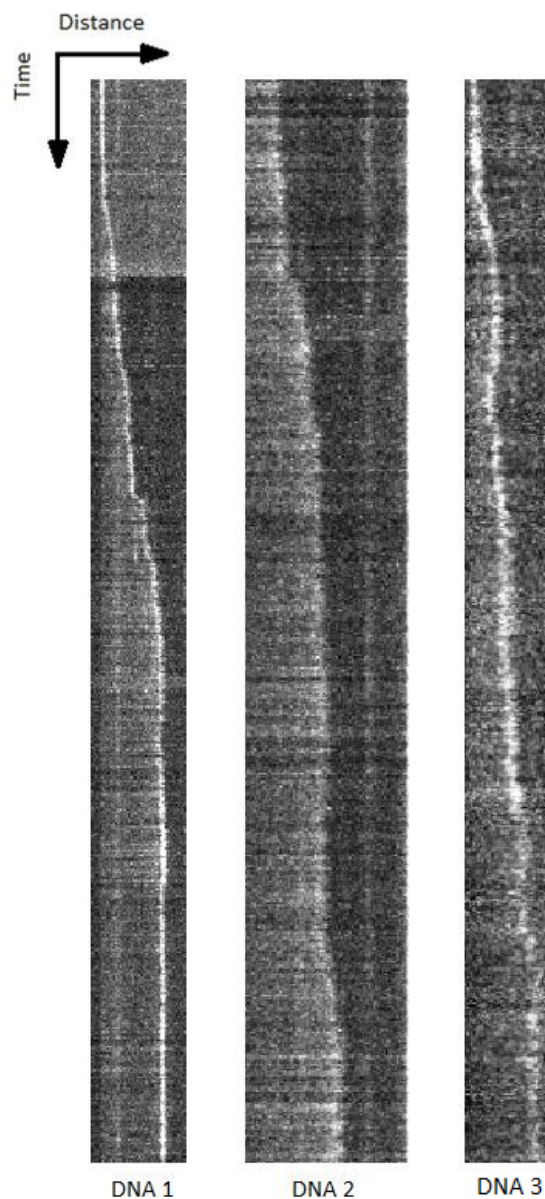

Figure 3.15: *Kymographs of the YO-PRO-1 channel, showing growing of DNA in time due to replication of M13 (300 ms exposure time).*

Doing a base pairs per pixel calculation using the conversion sheet from Appendix B (applies to the ds-DNA formed during replication), the replication rates of the kymographs in figure 3.15 are estimated. The products formed are around 23.4 kilobase pairs long, which indeed indicate the above described replication doing multiple rotations of the rolling-circle template. DNA 1 has a rate of around 274 base pairs per second, DNA 2 of 163 base pairs per second and DNA 3 of 162 base pairs per second. These values are lower than obtained by Tanner *et al*. [91], who found a mean rate of around 536 base pairs per second in M13 rolling-circle replication. However, the experiment shown here is performed with less β clamps in solution and the fact that they are labelled could also affect the rate.

Looking at the kymograph of figure 3.16, the labelled β clamp can do replication, i.e. it is still functional upon labelling. This kymograph shows growing of the product in the YO-PRO-1 channel and movement of the Cy5 molecule of the β clamp in the exact same way (647 nm laser, 8.5 W/cm^2). Unfortunately, this particular reaction resulted in the replication of only 7.6 kilobase pairs, which could mean that the labelling decreased the processivity upon labelling the β clamp.

Figure 3.16: Kymograph of M13 rolling-circle replication with a Cy5-labelled β clamp (300 ms exposure time). The left channel is the DNA product stained with YO-PRO-1, the right channel is the movement of the β clamp with Cy5 label.

However, this is not the case. As illustrated in figure 3.17, replication with the labelled β clamp can still obtain longer products. Unfortunately, this experiment was not done under the best conditions. The flow-stretched product show fluctuations due to flow and there was too much M13 templates bound to the surface in the background, which results in the vertical (i.e. stationary molecules) lines in the kymograph. However, the product shown in figure 3.17 is around 35.7 kilobase pairs long. Figure 3.17 also proofs again that the Cy5 channel indeed shows the β clamp and is not leak-through from the YO-PRO-1 channel. This is also discussed in the previous section. In figure 3.17, at the end of the recorded movie, the 488 nm laser was switched of, showing the black region in the kymograph. The Cy5 channels shows a decrease in overall intensity, because there is less illumination, but it still shows the movement of the β clamp.
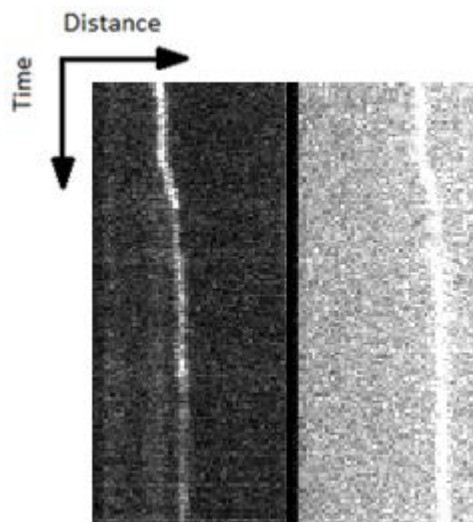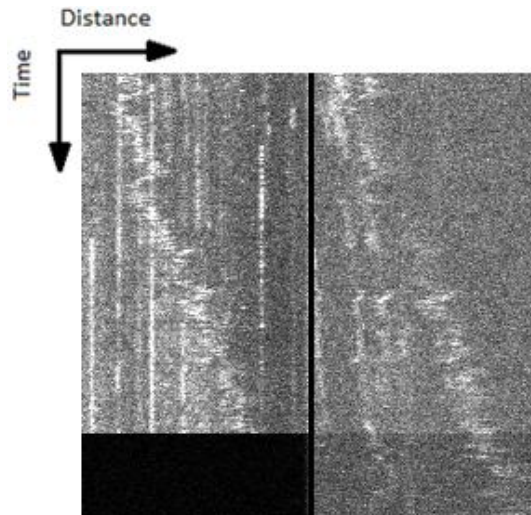
Figure 3.17: Kymograph of M13 rolling-circle replication with a Cy5-labelled β clamp (200 ms exposure time). The left channel is the DNA product stained with YO-PRO-1, the right channel is the movement of the β clamp with Cy5 label. At the end of the recorded movie, the 488 nm laser is switched off, still showing movement of the β clamp in the Cy5 channel, proving a real observation of the β clamp.

Looking closer at the long replication products, there are β clamps left behind on the product. This is shown in figure 3.18. Stukenberg *et al*. [92] showed that polymerase core remains bound to the β clamp as long as there is DNA to be replicated. In lagging-strand replication, when an Okazaki fragment is completed, the polymerase core disengages from the β clamp and dissociates in solution. This leaves the β clamp behind, while the polymerase core reassociates with a new primed template where the clamp-loader complex has loaded another β clamp.
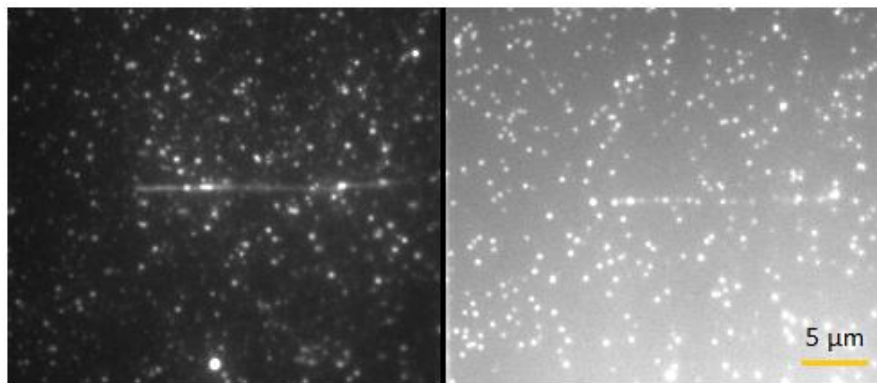
Figure 3.18: TIRF microscope image of an M13 replication product, stained with YO-PRO-1 (left channel) and Cy5-labelled β clamps left behind on the product (right channel). Flow is coming in from the left at a flow rate of 10 µl/min. This is an average intensity sum over 50 frames, with an exposure time of 200 ms.

Figure 3.18 shows the fully fluorescent signal of the replication product in the YO-PRO-1 channel, but the Cy5 channel shows fluorescent spots at the DNA. This indicates single β clamps left behind. As stated above, these β clamps will be left behind upon finishing an Okazaki fragment. In other words, the spacing between the single spots in the Cy5 channel should be around 1-2 kilobase pairs long, which is the length of the Okazaki fragments formed by the lagging-strand polymerase [64]. Figure 3.19 shows the line profile of the Cy5 spots of figure 3.18.
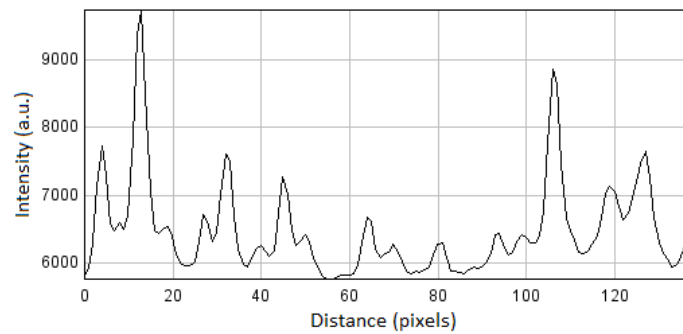
Figure 3.19: *Line profile along the DNA of the Cy5 channel of figure 3.18, clearly showing peaks.*

The line profile clearly shows multiple peaks, corresponding to single β clamps left behind. Figure 3.20 shows a histogram of the distance between the peaks, i.e. the suspected Okazaki fragment length, for multiple line profiles, such as figure 3.19, taken from various replication products in the Cy5 channel. A single-exponential decay is fitted, ignoring the first bin. These values are undersampled because of the limited resolution (around 300 nm, i.e. 1300 base pairs) of the camera and should therefore be ignored.
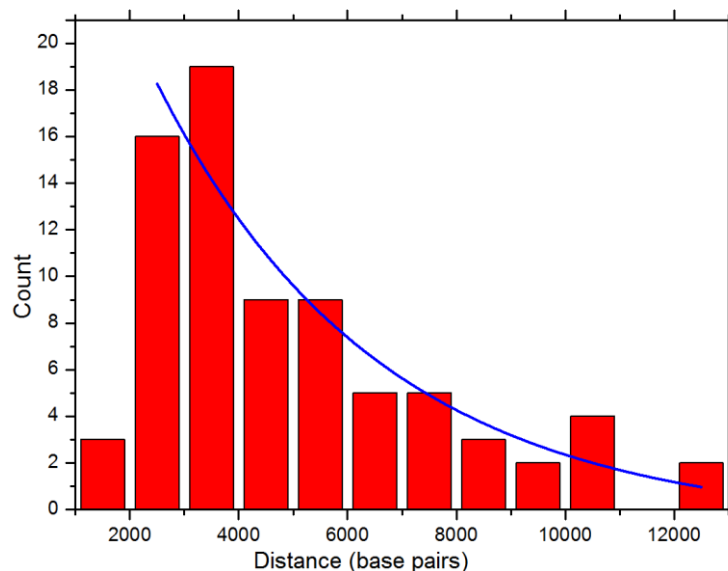
Figure 3.20: *Histogram of the distance between peaks (in base pairs) of the line profiles taken from multiple Cy5 channels over all left behind β clamps. The exponential fit gives the mean value with standard deviation for the distances: 4099 ± 64 base pairs.*

As can be seen in figure 3.20, the average distance between the β clamps is 4099 ± 64 base pairs. However, this data comes from experiments performed with the Cy5-labelled β clamps and as stated in section 3.2, only 12.9 % of the β clamps are labelled with a Cy5 molecule. Thus, assuming that the labelled and non-labelled β clamps have equal affinity to be loaded and coupled to the polymerase, this data would suggest Okazaki fragments of 529 ± 8 base pairs long. These are quite short Okazaki fragments, but it still looks like β clamps left behind during lagging-strand replication. The same experiment is also done with the Alexa488- and Alexx647-labelled β clamps, which have a significant higher labelling efficiency than the Cy5-labelled β clamp. The Alexa488-labelled β clamp has a labelling efficiency of 39.7 %. The experiment with Alexa488 β clamps is performed while staining the DNA with 150 nM TO-

PRO-3. TO-PRO-3 is a DNA stain with excitation and emission maxima at 642 nm and 661 nm respectively. The Alexa647 β clamps have the highest labelling efficiency of 90.4%. The result of the M13 rolling-circle replication experiment with Alexa647 β clamps is shown in figure 3.21. Unfortunately, the contrast in the YO-PRO-1 channel is poor.
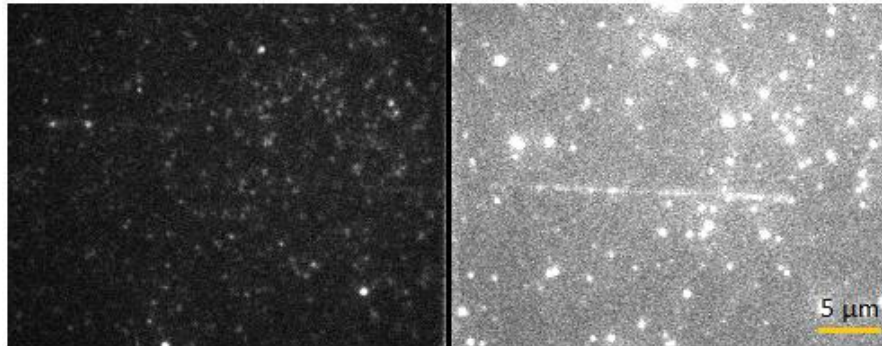
Figure 3.21: TIRF microscope image of an M13 replication product, stained with YO-PRO-1 (left channel) and Alexa647-labelled β clamps left behind on the product (right channel). Flow is coming in from the left at a flow rate of 10 μl/min. This image is a single frame, taken with an exposure time of 120 ms.

Figure 3.21 shows many β clamps left behind on the replication product. Although this is a single frame, it is not possible to distinguish single β clamps, because the fluoresence signal is diffraction limmited. Calculating backwards from 1-2 kilobase pairs long Okazaki fragments, with almost all β clamps fluorescently labelled, the average distance between two β clamps should be 2-3 pixels. With the resolution of the camera, it is not possible to visualize this, and this would indeed result in a smeared-out signal as shown in figure 3.21.

An attempt is made to do a replication experiment with a mixture of Alexa488- and Alexa647-labelled β clamps. This mixture is made in a ratio that the amount of Alexa488 and Alexa 647 β clamps was equal. Figure 3.22 shows the result. Both channels show β clamps left behind. Unfortunately it was not possible to capture replication in real-time.
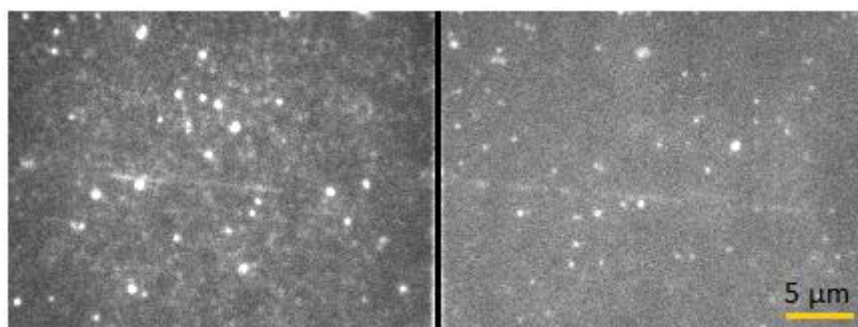
Figure 3.22: TIRF microscope image of an M13 replication product, with Alexa488 (left channel) and Alexa647 (right channel) β clamps left behind on the product. Flow is coming in from the left at a flow rate of 10 μl/min. This image is a single frame, taken with an exposure time of 200 ms.

The question remains what the exact mechanism of the β clamp is. The clamp-loader complex cannot only *load* the β clamp onto the DNA template, it can also *unload* the β clamp. The β clamps left behind remain stable on the DNA (half-time of around 115 minutes [93]) and must be removed rapidly for reuse at numerous primed sites on the lagging-strand. It was found that the δ subunit of the DNA polymerase III holoenzyme opens and hence unloads the β clamp without any need for ATP to catalyse clamp unloading [93]. Tanner *et*

al. [82] showed that the β clamp can be recycled during replication when they did replication in the absence of free β clamps. The β clamps were unloaded and reloaded onto a new primed site. These primed sites are created by the primase and form the beginning of the Okazaki fragments. Therefore, insight into the effect of the DnaG primase on the Okazaki fragment length can be obtained by tracking the β clamps. This is done in the next section.

3.5   Visualization of the effect of DnaG primase on Okazaki fragment length

As shown in the previous section, the labelled β clamps are left behind on the stretched-out M13 replication products. With a low labelling efficiency, it was possible to distinguish individual β clamps. With a high labelling efficiency this was not possible, because the fluorescence signal is diffraction limited. As stated in section 3.1, initiation of each Okazaki fragment requires an RNA primer of around 10 to 12 nucleotides long, synthesised by the DnaG primase [78]. As shown in figure 3.3, the clamp-loader complex loads the β clamp onto this primer. After that, the polymerase associates with the β clamp and starts to synthesize the Okazaki fragment. In other words, DnaG is a key component in formation of Okazaki fragments. In this section, the effect of DnaG primase on the Okazaki fragment length is investigated by visualizing the labelled β clamps left behind.

During this experiment, a modified replication protocol came up in the Van Oijen Lab. The exact protocol is given in Appendix C. The protocol basically contains two differences compared to the previous 'standard' protocol as used during the replication experiments in section 3.4. At first, the modified protocol introduces a pre-loading of the DnaB/DnaC complex. This is not really pre-assembly, because the DnaB/DnaC complex remains in the replication mixture after adding the other proteins. However, it gives the DnaB/DnaC complex a head start and a slightly higher concentration to enhance its binding to the replication fork before all other proteins are introduced in solution. The idea behind this is that it would increase the replication yield by having a higher chance that the helicase binds to the template. As discussed in section 3.1, a critical step in DNA replication is loading of the helicase (DnaB) onto the DNA by DnaC. The second difference between the standard and the modified protocol is that the new protocol does not include the so-called restart proteins. There has been a discussion about the function and it turned out that excluding the restart proteins resulted in a higher yield. However, it was found that, upon excluding the restart proteins, there were two distinct replication product populations visible. Leaving out the restart proteins results in a population of very long and a population of extremely short replication products. These very short products are only a couple of kilobase pairs long. However, it turned out that the higher yield compared to the standard protocol is due to the formation of the very short product population. Looking closer to the very short products, it was suggested that the short products are formed by strand displacement synthesis. In this case, the leading strand synthesis does not continue to replicate the rolling circle as drawn in figure 3.13, but upon strand displacement it starts to complement its own complementary strand, without DnaB present at the fork. In other words, it takes over the lagging-strand synthesis and synthesizes back in the formation of an Okazaki fragment. After strand displacement it is not possible anymore to do rolling-circle replication, because the extended 3' end drawn in figure 3.13 has reached the beginning of the previously formed Okazaki fragment. As a result, the products stop growing and only short ds-DNA replication products are produced. The mechanisms of strand displacement is beyond the scope of this thesis and

will not be discussed here. The important remark is that the restart proteins seem to suppress strand displacement synthesis.

This section shows replication products of M13 rolling-circle replication with and without the DnaG primase present. At first, the experiments are carried out with 10 nM of the Cy5-labelled β clamps. Figure 3.23 shows again the β clamps left behind when the standard amount of DnaG is introduces (100 nM). An intensity sum over a couple of frames is made to enhance the contrast. It is clearly visible that this is a long product and that there are multiple β clamps visible in the Cy5 channel.

Figure 3.23: TIRF microscope image of an M13 replication product performed with 100 nM DnaG. YO-PRO-1 DNA stain (left channel) and Cy5-labelled β clamps (right channel). Flow is coming in from the left at a flow rate of 10 µl/min. This is an average intensity sum over 50 frames, with an exposure time of 200 ms.

The exact same experiment is done without adding any DnaG to the protein mixture. The result is shown in figure 3.24. Replication did take place, although the products were particularly short. It is clearly visible that the Cy5 channel does not show any β clamp left behind on the product. This result is as expected, because without DnaG, no RNA primers are formed and hence there are no templates for the β clamps to be loaded on. In fact, no lagging-strand replication takes place without DnaG, no Okazaki fragments are formed and thus no β clamps are left behind. Moreover, this proofs that the β clamps visible in figure 3.23 are indeed left behind on the product and that they are not there due to nonspecific binding to the DNA.

Figure 3.24: TIRF microscope image of an M13 replication product performed without DnaG. YO-PRO-1 DNA stain (left channel) and Cy5-labelled β clamps (right channel). Flow is coming in from the left at a flow rate of 10 µl/min. This is an average intensity sum over 50 frames, with an exposure time of 200 ms.

However, only short products are visible in doing the replication experiment without DnaG. Since the experiment is done without the restart proteins, it is possible that figure 3.24 shows the short product created by strand displacement. As described above, these short products are ds-DNA. However, if strand displacement did not take place, only leading-strand replication takes place. This results in a long single-stranded product with only the head of the product, i.e. the circular template, being ds-DNA. Important to mention here is that the 250 nM SSB in solution prevents the ss-DNA to coil up, meaning that it should still

be stretched-out and visible. According to the manufacturer, YO-PRO-1 dyes should also bind to ss-DNA, although typically with a lower fluorescence quantum yield. However, Yao *et al.* [94] state that the YO-PRO-1 intercalating dye does not detect ss-DNA. If that is indeed the case, only the rolling-circle should be visible in the YO-PRO-1 channel, but with the enormous amount of M13 templates bound to the surface, it impossible to distinguish this from the background. This is no proof, but the fact that no long ss-DNA products are visible does not necessarily mean that they are not there.

The same experiment is done with the Alexa647 β clamps, which has a higher labelling efficiency. This experiment is carried out with 100 nM DnaG, less DnaG (20 nM) and no DnaG. Figure 3.25 shows the products with 100 nM DnaG, which looks the same as in figure 3.23. Figure 3.26 shows the products with 20 nM DnaG. Here it is hard to draw conclusions. It looks like there are some products. However, they look spotty in the YO-PRO-1 channel. A possibility is that the Okazaki fragments are not formed completely, leaving pieces of ss-DNA in the product, that are not (properly) stained with YO-PRO-1. The Alexa647 also shows some smears, but they look more spotty than in figure 3.26, which might mean bigger spacing between the β clamps. However, this is definitely a point for future research. Figure 3.27 shows the product without DnaG. The products here are extremely short and nothing is visible in the Alexa647 channel.
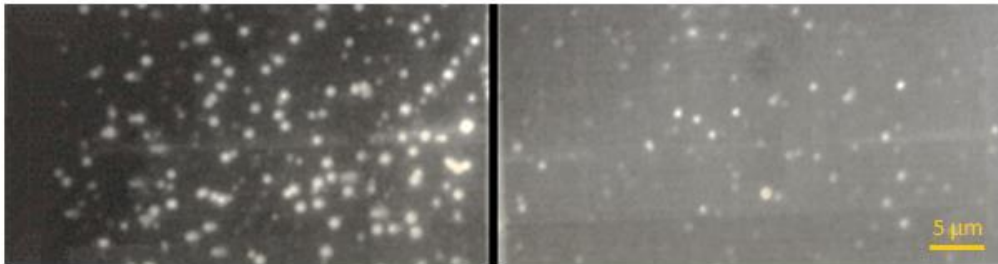

Figure 3.25: TIRF microscope image of M13 replication products performed with 100nM DnaG. YO-PRO-1 DNA stain (left channel) and Alexa647-labelled β clamps (right channel). Flow is coming in from the left at a flow rate of 10 µl/min. This is an average intensity sum over 200 frames, with an exposure time of 200 ms.
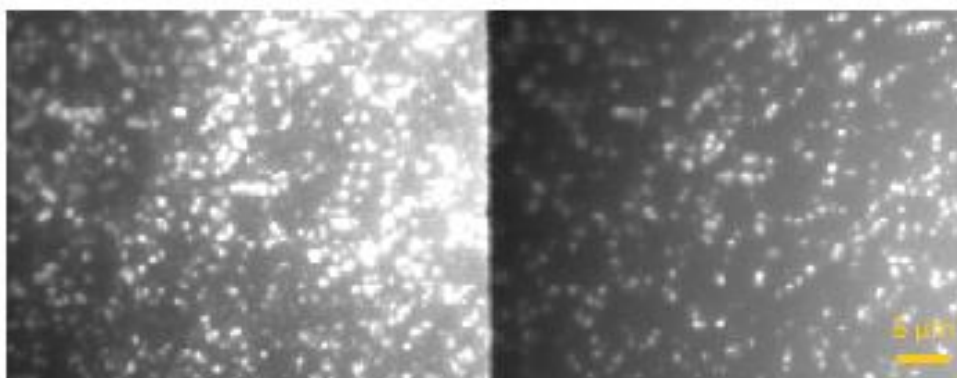
Figure 3.26: TIRF microscope image of M13 replication products performed with 20nM DnaG. YO-PRO-1 DNA stain (left channel) and Alexa647-labelled β clamps (right channel). Flow is coming in from the left at a flow rate of 10 µl/min. This is an average intensity sum over 200 frames, with an exposure time of 200 ms.
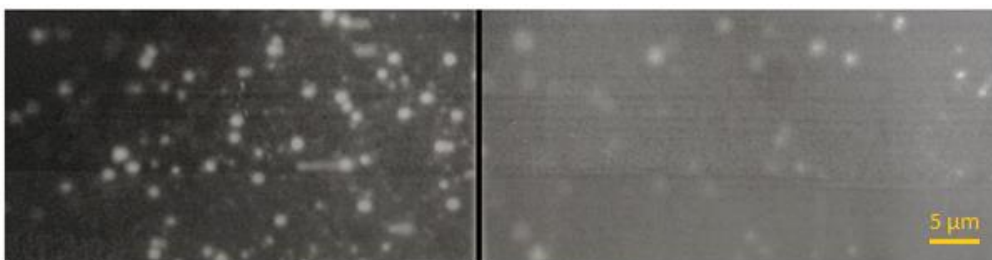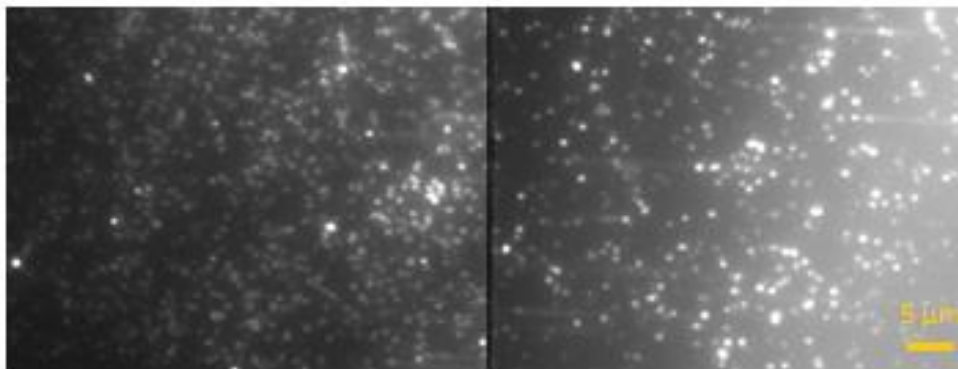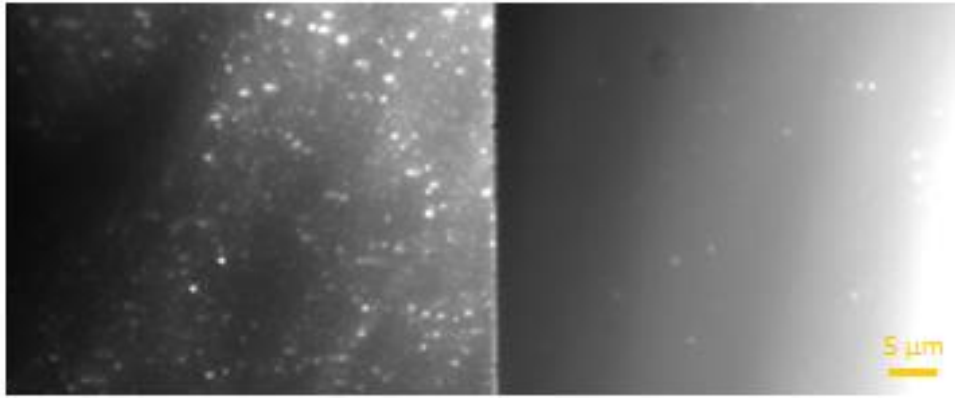
Figure 3.27: *TIRF microscope image of M13 replication products performed without DnaG. YO-PRO-1 DNA stain (left channel) and Alexa647-labelled β clamps (right channel). Flow is coming in from the left at a flow rate of 10 µl/min. This is an average intensity sum over 200 frames, with an exposure time of 200 ms.*

Another attempt is made to do the same experiment with 100 nM DnaG, but without CTP, GTP and UTP. This should have the same effect as without DnaG, because CTP, GTP and UTP are the building blocks for the RNA primer made by the primase. Without the primase or without the ribonucleotides, the primed template cannot be made. However, no replication products were visible during this experiment. This was also done with less CTP, GTP and UTP (50 µM each instead of 250 µM), but again no replication products were visible. If it is indeed the case that YO-PRO-1 cannot stain the ss-DNA and only products of strand displacement can be visible without DnaG, leaving out these ribonucleotides might supress strand displacement. However, no proof is given.

3.6 Conclusion

The goal of this chapter was to investigate the role of the *E. coli* β clamp in DNA replication kinetics, i.e. to track the motion of the β clamp during M13 rolling-circle replication to get a better understanding of its mechanism.

At first, the β clamps were successfully labelled using different fluorescent dye molecules. It was proven that the labelled β clamps kept their affinity for binding ds-DNA. This was visible by having labelled β clamps loaded onto linear ds-DNA which was bound to the surface at both ends. The fact that the β clamps were not loaded on all bridge-like DNA constructs showed that the binding to the DNA was a result of clamp-loading and not due to nonspecific binding. It turned out that the interaction between the clamp-loader complex and the forked arm was the limiting factor for binding.

It was proven that the labelled β clamps remain functional during M13 rolling-circle replication. This was proven by simultaneously imaging replication product growth and displacement of the β clamp at the tip of the replication product. During replication, it was found that individual β clamps were left behind on the product. It was strongly suggested that the β clamps are left behind after completion of every Okazaki fragment in lagging-strand synthesis. Analysis showed that the average distance between the β clamps, i.e. the length of the Okazaki fragments, is 529 ± 8 base pairs long, assuming equal affinity of the labelled and the non-labelled β clamps to the DNA. However, with the spatial resolution of the camera, it was not possible to distinguish singular β clamps when the labelling efficiency was close to 100%.

The labelled β clamps were used to investigate the effect of DnaG primase on the Okazaki fragment length. It was shown that excluding DnaG results in not having any β clamp left behind on the replication product. Reason for this is that no primed templates are formed where the β clamps can binds. No Okazaki fragments are formed without DnaG. Without DnaG, only very short replication products were visible. The reason for this can be found in strand displacement synthesis. When strand displacement takes place, the products are short and double-stranded. When there is no DnaG and strand displacement does not take place, long and stretched-out (due to SSB) ss-DNA products are formed. However, these products were not visible in the performed experiments. The reason for this could be that the used YO-PRO-1 DNA stain does not seems to bind to ss-DNA [94] and hence the long products are simply not visible. This could also explain the spotty pattern of the DNA stain when only one fifth, i.e. 20 nM, DnaG was introduced in the replication reaction. In that case, incomplete Okazaki fragments could have been formed, creating alternating pieces of ss-DNA and ds-DNA. The presence or absence of these long products cannot be concluded from this research, it still needs to be proven.

3.7   Future perspective

This section highlights various new ideas for future work, regarding the labelled β clamps.

The mechanism of the β clamp in DNA replication is still not fully known. It was found in previous work that the β clamps are reused during replication [82], but is this recycling or exchange? A suggestion is to have a 1:1 mixture of 100 % labelled β clamps with different colour dyes. Correlation analysis of the differently labelled protein could indicate whether the β clamps are exchanged during replication.

In order to fully check the distance between the β clamps left behind on the replication product, i.e. the proposed Okazaki fragment length, measurements should be performed with a 100 % labelled β clamps and a camera with a higher spatial resolution. The diffraction limit of the camera used (around 230 nm) is insufficient to distinguish the individual β clamps.

The β clamp binds to multiple proteins, like the polymerase and a subunit of the clamp-loader complex. These binding sites, however, are competing [67]. The β clamp cannot be unloaded when the polymerase remains bound. Interesting would be to label a subunit of the polymerase with a different coloured dye and see if the polymerase remains bound when the β clamps are left behind on the replication product.

A suggestion to check if long products have formed during replication without DnaG, is to use fluorescently labelled SSB. That will make the long ss-DNA products visible if they are there. Moreover, repeating the experiment without or with less ribonucleotides is suggested.

4.   DNA binding to suspended gold nanowires

The research project described in this chapter focuses on methods to bind DNA molecules to suspended gold nanowires in a flow cell. The first section will introduce the problem of binding DNA to the bottom surface of the flow cell and describes how the use of nanowires can solve this. Moreover, some information about other applications of suspended nanowires in flow cells is given. The sections that follow will describe how the DNA molecules can be bound chemically to gold, how the nanowires are made and how the flow cells with suspended nanowires are constructed. After that, the experiment is carried out on both nanowires deposited onto the bottom surface and nanowires suspended within the flow cell. At last, concluding remarks and comments on future work are given.

4.1   Introduction

Section 2.4 already clearly described the disadvantage of using streptavidin-functionalised coverslips. The biotinylated DNA molecules are tethered to the surface by one end, and stretched-out by a flow. As the DNA molecules are bound to the surface by one end, while the other end is loose within the flow, the fluctuations of the stretched-out DNA molecules is significant. The reason for this is that the DNA molecules are tethered to the surface, where the flow is by definition equal to zero. Since the flow profile has a parabolic shape, with its maximum at the centre of the flow cell, the molecules that are moving only slightly above the surface are in a low velocity regime. Bringing the molecules up in the flow, where the flow profile is more stable, will result in better stretched-out molecules with less fluctuations. Figure 2.14 shows these fluctuations upon making an intensity sum over 2000 frames. These fluctuations are highly undesired, because they disturb the precision of the measurements, i.e. the precise localization of molecules, which is a key component in single-molecule studies. Moreover, bringing the molecules up in the flow will benefit from a lower flow rate and a higher chance that replication proteins will bind the DNA molecules. Thus, it would be beneficial to place the DNA molecules up in the flow. This is illustrated by the simplified calculations of the flow profile.

These calculations of the flow profile in the rectangular flow cell follow [95]. As described in the previous chapters, the flow cell face has a rectangular geometry of 500 μm wide and 100 μm high. This is shown in figure 4.1.
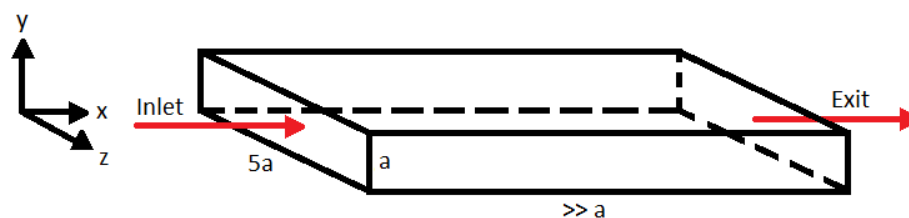
Figure 4.1: Geometry of the flow cell.

As can be seen in figure 4.1, the flow cell is five times as wide as it is high. For that reason, the assumption is made that in the middle of the flow cell (in the z-direction), the variation of the flow profile in the z-direction is minimized and therefore assumed to be neglected.

Hence only the two-dimensional situation as drawn in figure 4.2 is considered for simplicity reasons.
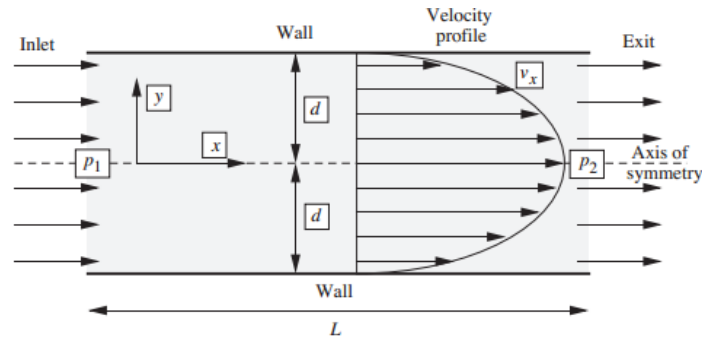
Figure 4.2: Geometry of the flow through a rectangular duct, assuming no variation in the z-direction. Figure source: [95].

The flow is *Poiseuille*, because it is caused by the pressure difference $(p_1 - p_2)$. Moreover, the following assumptions are made: The flow is only in the x-direction, meaning that only the velocity v_x is nonzero, while $v_y = v_z = 0$. Moreover, there is no variation in velocity in the z-direction, i.e. $\partial v_x/\partial z = 0$. The flow is steady and Newtonian, with constant density ρ and viscosity μ. The velocity is zero at the walls, so that $v_x = 0$ at $y = \pm d$, where d is the distance between the centreline and axis of symmetry $y = 0$ and the walls, as illustrated in figure 4.2. L is the length of the flow cell, defined in the x-direction. The gravity acts in the y-direction; $g_y = -g$ and $g_x = g_z = 0$.

In steady state, the rate at which mass enters a system is equal to the rate at which the mass leaves the system. This leads to the following continuity equation:

$$\frac{\partial \rho}{\partial t} + \frac{\partial(\rho v_x)}{\partial x} + \frac{\partial(\rho v_y)}{\partial y} + \frac{\partial(\rho v_z)}{\partial z} = 0 \qquad \text{Eq. 1}$$

Due to the assumption that the density is constant, this simplifies to:

$$\frac{\partial v_x}{\partial x} + \frac{\partial v_y}{\partial y} + \frac{\partial v_z}{\partial z} = 0 \qquad \text{Eq. 2}$$

With the assumption made that $v_y = v_z = 0$, this results into:

$$\frac{\partial v_x}{\partial x} = 0 \qquad \text{Eq. 3}$$

As a result, v_x is independent from its position in the x-direction. Thus, the velocity profile is the same for all values of x. Moreover, since it was assumed that $\partial v_x/\partial z = 0$, it follows that $v_x = v_x(y)$, i.e. the velocity in the x-drection is only a function of y. Applying the Navier-Stokes equations to the Newtonian fluid gives:

$$\rho\left(\frac{\partial \overline{v}}{\partial t} + \overline{v} \cdot \nabla \overline{v}\right) = -\nabla \overline{p} + \mu \nabla^2 \overline{v} + \rho \overline{g} \qquad \text{Eq. 4}$$

Writing this for all directions gives the momentum balances for the x-, y- and z-directions:

$$\rho\left(\frac{\partial v_x}{\partial t} + v_x\frac{\partial v_x}{\partial x} + v_y\frac{\partial v_x}{\partial y} + v_z\frac{\partial v_x}{\partial z}\right) = -\frac{\partial p}{\partial x} + \mu\left(\frac{\partial^2 v_x}{\partial x^2} + \frac{\partial^2 v_x}{\partial y^2} + \frac{\partial^2 v_x}{\partial z^2}\right) + \rho g_x$$

$$\rho\left(\frac{\partial v_y}{\partial t} + v_x\frac{\partial v_y}{\partial x} + v_y\frac{\partial v_y}{\partial y} + v_z\frac{\partial v_y}{\partial z}\right) = -\frac{\partial p}{\partial y} + \mu\left(\frac{\partial^2 v_y}{\partial x^2} + \frac{\partial^2 v_y}{\partial y^2} + \frac{\partial^2 v_y}{\partial z^2}\right) + \rho g_y \quad \text{Eq. 5}$$

$$\rho\left(\frac{\partial v_z}{\partial t} + v_x\frac{\partial v_z}{\partial x} + v_y\frac{\partial v_z}{\partial y} + v_z\frac{\partial v_z}{\partial z}\right) = -\frac{\partial p}{\partial z} + \mu\left(\frac{\partial^2 v_z}{\partial x^2} + \frac{\partial^2 v_z}{\partial y^2} + \frac{\partial^2 v_z}{\partial z^2}\right) + \rho g_z$$

sing the following made consumptions: $v_y = v_z = 0$, $\partial v_x/\partial x = 0$ (Eq. 3), $g_y = -g$ and $g_x = g_z = 0$, and steady flow with constant density and velocity, these equations simplify to the following:

$$\frac{\partial p}{\partial x} = \mu\frac{\partial^2 v_x}{\partial y^2} \qquad\qquad \text{Eq. 6}$$

$$\frac{\partial p}{\partial y} = -\rho g \qquad\qquad \text{Eq. 7}$$

$$\frac{\partial p}{\partial z} = 0 \qquad\qquad \text{Eq. 8}$$

Eq. 8 indicates that there is no pressure variation across the width of the channel. Integration of Eq. 7 gives the equation for the pressure in the system:

$$p = -\rho g\int dy + f(x) = -\rho g y + f(x) \qquad\qquad \text{Eq. 9}$$

Note that integration over a partial differential equation gives a function of integration rather than an integration constant. Upon assumption that $\partial p/\partial x$ is constant, i.e. a uniform pressure gradient and a fully developed flow profile, the function of integration is a linear function. Thus, at the axis of symmetry ($y = 0$, see figure 4.2), the equation for the pressure has the following form:

$$p_{y=0} = ax + b \qquad\qquad \text{Eq. 10}$$

Using the following boundary conditions (visible in figure 4.2):

$$\text{at} \quad x = 0: \qquad p = p_1 = b \qquad\qquad \text{Eq. 11}$$

$$\text{at} \quad x = L: \qquad p = p_2 = aL + b \qquad\qquad \text{Eq. 12}$$

This leads to:

$$b = p_1 \qquad\qquad \text{Eq. 13}$$

$$a = -\frac{p_1 - p_2}{L} \qquad \text{Eq. 14}$$

Filling in Eq. 13 and Eg.14 in Eq. 10 and Eq. 9 gives the complete pressure distribution:

$$p = p_1 - \frac{x}{L}(p_1 - p_2) - \rho g y \qquad \text{Eq. 15}$$

As $\partial v_x / \partial z = 0$ and $\partial v_x / \partial x = 0$ (Eq.3), the partial derivative of Eq. 6 because a total derivative:

$$\frac{\partial p}{\partial x} = \mu \frac{d^2 v_x}{dy^2} \qquad \text{Eq. 16}$$

And from Eq. 15 follows that the pressure gradient between the inlet and exit is given by:

$$\frac{\partial p}{\partial x} = -\frac{(p_1 - p_2)}{L} \qquad \text{Eq. 17}$$

Eq. 16 is a second-order differential equation and integrating twice over y will lead to a function for v_x. The first integration gives:

$$\int \frac{d^2 v_x}{dy^2} dy = \int \frac{d}{dy}\left(\frac{dv_x}{dy}\right) dy = \int \frac{1}{\mu}\left(\frac{\partial p}{\partial x}\right) dy$$

$$\frac{dv_x}{dy} = \frac{1}{\mu}\left(\frac{\partial p}{\partial x}\right) y + c_1 \qquad \text{Eq. 18}$$

The second integration gives:

$$\int \frac{dv_x}{dy} dy = \int \left[\frac{1}{\mu}\left(\frac{\partial p}{\partial x}\right) y + c_1\right] dy$$

$$v_x = \frac{1}{2\mu}\left(\frac{\partial p}{\partial x}\right) y^2 + c_1 y + c_2 \qquad \text{Eq. 19}$$

The integration constants, c_1 and c_2, can be calculated using the following boundary conditions:

$$\text{at} \quad y = 0: \qquad \frac{dv_x}{dy} = 0 \qquad \text{Eq. 20}$$

$$\text{at} \quad y = d: \qquad v_x = 0 \qquad \text{Eq. 21}$$

Implementing this in Eq. 19 leads to:

$$c_1 = 0 \qquad \text{Eq. 22}$$

$$c_2 = -\frac{1}{2\mu}\left(\frac{\partial p}{\partial x}\right)d^2 \qquad \text{Eq. 23}$$

Thus, filling in Eq. 22 and Eq. 23 in Eq. 19 gives the velocity profile as drawn in figure 4.2:

$$v_x = \frac{1}{2\mu}\left(-\frac{\partial p}{\partial x}\right)(d^2 - y^2) \qquad \text{Eq. 24}$$

Note that $p_1 > p_2$ in order to have flow in the positive x direction. Thus, in Eq. 17 yields a negative value for the pressure gradient and hence the velocity in Eq. 24 is always positive. Eq. 24 shows clearly that the flow profile is parabolic. Since the pressure gradient is assumed to be uniform, i.e. $\partial p/\partial x$ is a constant, the ratio of flow speed at different heights (y-positions) is given by:

$$\frac{v_{x1}}{v_{x2}} = \frac{\left(d^2 - y_1{}^2\right)}{\left(d^2 - y_2{}^2\right)} \qquad \text{Eq. 25}$$

Thus, coming back to the flow cell geometry used in this research, with $d = 50$ µm, the ratio of the flow speed in the middle of the cell over the flow speed at only 0.2 µm above the bottom surface (where the λ DNA molecules that are tethered to the surface move) is:

$$\frac{v_{x1}}{v_{x2}} = \frac{(50^2 - 0^2)}{(50^2 - 49.8^2)} \approx 125$$

This is a massive increase of flow speed in the middle of the flow cell, compared to the place where the DNA molecules are usually tethered to the surface. Even bringing the molecules slightly up in the flow, for example 20 µm, results in a significant enhancement of the flow speed along the DNA:

$$\frac{v_{x1}}{v_{x2}} = \frac{(50^2 - 30^2)}{(50^2 - 49.8^2)} \approx 80$$

The above calculations clearly show that bringing the DNA molecules up in the flow will benefit from a significant higher flow speed, i.e. lower flow rates could be used during the experiments. The idea in this research project is to span a gold nanowire in the flow cell, perpendicular to the flow, and tether the DNA molecules to this wire. As a result, the DNA molecules will 'hang' in the flow by anchoring to the wires. A simple analogy that can be made, it that the DNA molecules will hang on the wires like clothes hang on a clothes line in massive wind. Thus, this would result in a 'curtain' of DNA molecules hanging on a wire within the flow cell.

These gold wires with nanometre thickness have been used for other purposes in flow. Examples are various nanowire biosensors in microfluidics [96] [97] [98] and flow speed and temperature sensors [99]. This research by Kalkman [99] made use of the same freely-suspended gold nanowires placed up in a flow cell, as will be used in this study.

4.2   Functionalization of gold surfaces

As stated in the introductory section 4.1, the goal of this research project is to anchor the DNA molecules to gold nanowires. Thus, the surface chemistry should be well-understood in order to bind the DNA molecules to the gold. The easiest way to figure out how to functionalize the gold nanowires is to start by functionalizing simple gold surfaces. These gold surfaces are made by deposition of a very thin gold layer onto clean glass coverslips. In order to be able to use TIRF microscopy, it is essential that this layer of gold is extremely thin and optically see-through. Therefore, a layer of 10 nm gold is deposited onto a 2 nm chromium adhesion layer.

 The idea is to have the same biotin-streptavidin-biotin interaction as on the 'normal' functionalized glass coverslips used in the previous chapters. Thus, the DNA molecules contain a biotinylated arm and are tethered *in situ* to the streptavidin-incubated biotin-functionalized coverslips. Therefore, the goal is to bind a biotin molecule to gold. For the 'normal' functionalized glass coverslips, the clean glass coverslips are silanized in order to get amine groups bound onto the surface. After that, the PEG molecules (a mixture of PEG molecules with and without a biotin to prevent full coverage of biotin in order to keep the surface from being too crowded with DNA molecules) are connected to the amine groups, providing a biotinylated surface. The gold-coated coverslips are functionalized in a similar way. Bonding of the amine groups is done with cysteamine (IUPAC: 2-aminoethanethiol). The cysteamine molecules form a self-assembled monolayer (SAM) on the gold. The formation of the SAMs is done by leaving the coverslips overnight in a cysteamine solution in high-purity ethanol. After this incubation step and rinsing with Milli-Q water, the same PEGylation step is done as for the 'normal' functionalized coverslips, i.e. incubation of the coverslips in PEG in $NaHCO_3$ (pH 8.2) for four hours. After these steps, the functionalized gold-coated coverslips are incubated in streptavidin and constructed into a flow cell. λ phage DNA molecules with 150 nM SYTOX Orange is flown in, this is shown in figure 4.3. The DNA molecules did bind to the gold substrate, the functionalization looks successful.
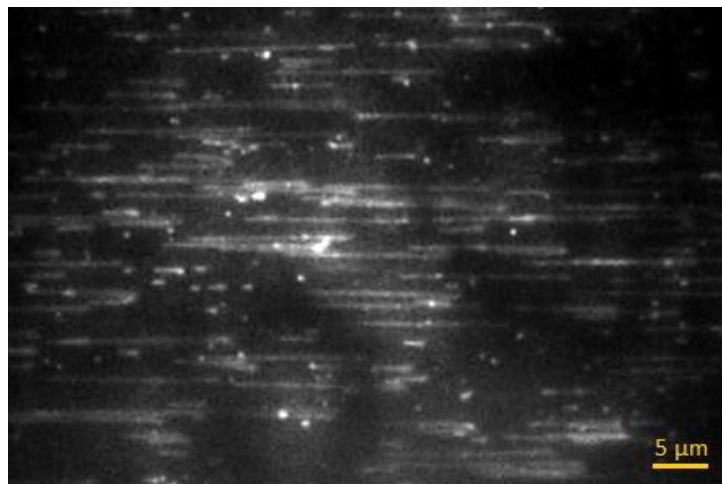
Figure 4.3: *TIRF microscope image of flow-stretched λ DNA stained with SYTOX Orange, bound to a gold substrate. Flow is coming in from the left at a flow rate of 10 µl/min. This image is a single frame, taken with an exposure time of 120 ms.*

However, an extra check is made to see if this procedure worked the way it should. Since every step of the synthesis procedure results in different hydrophobicity of the surface,

contact angle measurements are done after each step to see if the synthesis on the gold-coated coverslips yield the same result as on the glass coverslips. Figure 4.4 shows exactly how the contact angle is defined and figure 4.5 shows the results, comparing the contact angles after each synthesis step for glass and gold substrates. The experiment is performed with 2 mM and 10 mM cysteine in pure ethanol.
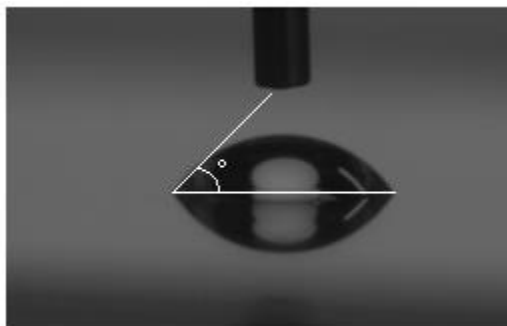
Figure 4.4: Definition of contact angle measure.

Clean glass	Silanized glass	Glass after PEGylation
59.6 ± 1.6 °	60.6 ± 2.5 °	32.3 ± 0.5 °

Clean gold	2 mM cysteamine on gold	Gold after PEGylation
71.0 ± 1.8 °	69.5 ± 1.8 °	38.4 ± 1.4 °

10 mM cysteamine on gold	Gold after PEGylation
60.7 ± 2.0 °	34.8 ± 2.0 °

Figure 4.5: Contact angle measurements after each synthesis step for glass and gold substrates with two different cysteine concentrations.

Janssen *et al.* [100] found that a SAM with amine groups has a contact angle of 58.4 ± 1.7 ° and a PEGylated surface has a contact angle of 35.8 ± 1.0 °. The values of the contact angles found for the glass substrate functionalization as can be seen in figure 4.5 are in close proximity with those published values. Using 10 mM cysteamine in formation of the SAM shows the same contact angle as silanized glass. However, using 2 mM cysteamine resulted in a more hydrophobic surface than expected, indicating the unsuccessful formation of a monolayer. In fact, the hydrophobicity did not change compared to the gold substrate before incubation in cysteamine. Thus, a higher concentration of cysteamine is required to form the SAM. However, both the gold surfaces with and without a successfully formed SAM obtain the same result upon PEGylation. This contact angle is the same as for the glass substrate and in agreement with [100]. Since there was no successful SAM formed upon incubation with 2 mM cysteamine, this suggests that PEG can bind nonsp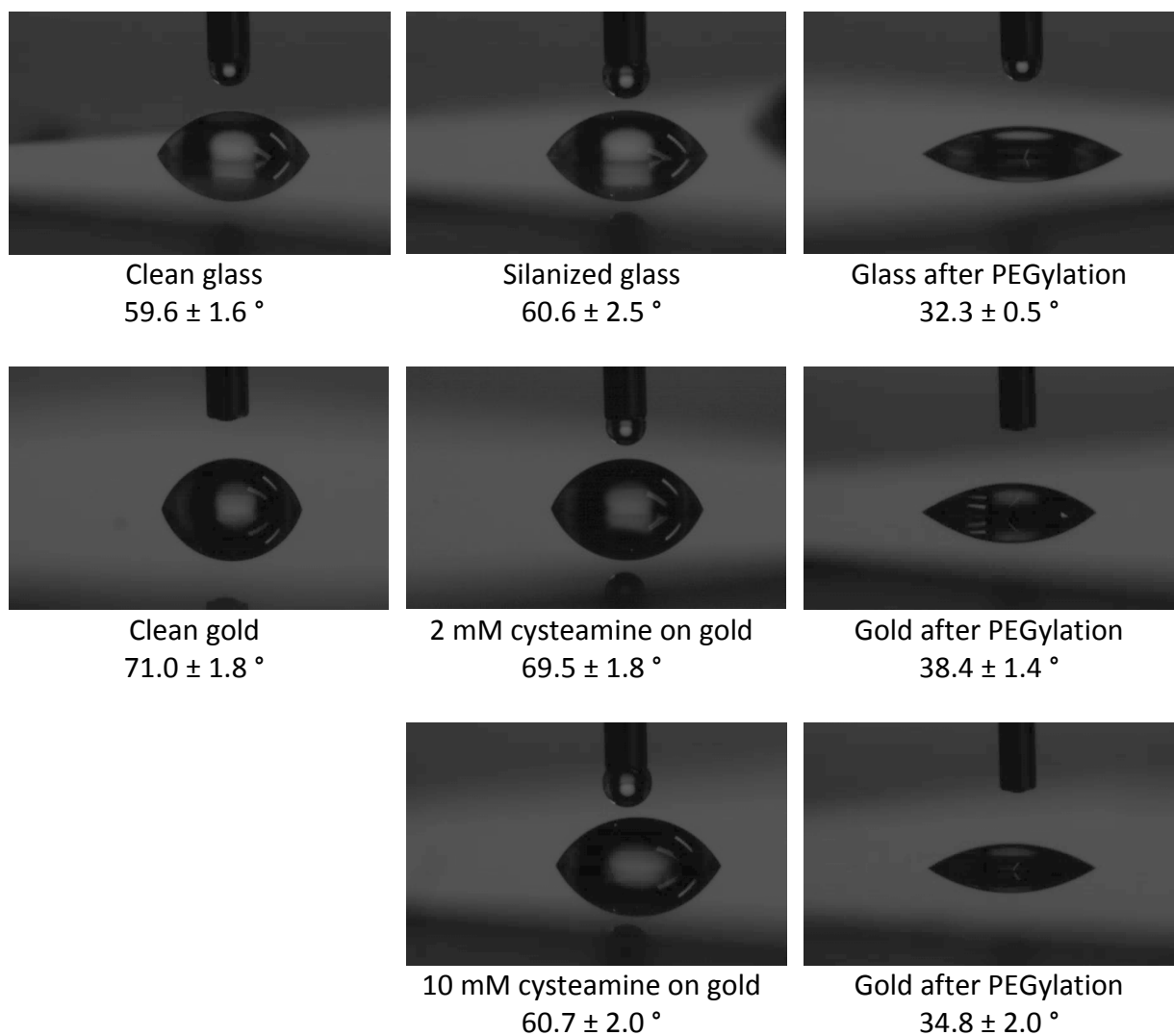ecifically to the surface. For functionalizing the surface, this is no problem. However, for functionalizing only the small surface of a nanowire, this is. This resulted into a lot of nonspecific binding of DNA molecules all over the coverslip. For that reason, and because the long PEG molecules are not needed upon functionalization of the nanowire, the synthesis procedure is slightly modified in this research project. After incubation with 10 mM cysteamine, the coverslips with nanowires are incubated in 5 mM biotin-NHS in $NaHCO_3$ (pH 8.2) for three hours. This links the biotin molecules to the cysteamine in the same way as visualized by the reaction in figure 3.5.

The following section will describe how the gold nanowires are fabricated.

4.3   Preparation of gold nanowires

The gold nanowires used in this research project are fabricated using nanoskiving. This section will explain in detail how the nanowires are fabricated and how nanoskiving works.

Nanoskiving is the name of the technique used for fabrication of nanostructures that combines the deposition of thin films on flat or topologically patterned polymeric substrates using physical vapour deposition with sectioning using a microtome [101]. The procedure is shown schematically in figure 4.6. At first, an epoxy substrate is fabricated. This is done by curing an epoxy prepolymer onto a PDMS layer. This PDMS layer can be flat or patterned, depending on the desired structure. The epoxy substrate is created by removing the PDMS. A thin metal layer (can be as small as 20 nm), gold in this research, is deposited onto the epoxy substrate by evaporation. The thickness of this layer will eventually determine how broad the wire will be. The dimensions are illustrated in figure 4.6. After deposition of the metal layer, another layer of epoxy is cured on top of it. This fully embed the deposited layer in epoxy. A jewellery saw is used in the a first rough cut step. A razor blade is used in the second rough cut step to cut a rough shape so that it fits the diamond knife of the microtome. Then a glass knife is used to cut the first sections, i.e. to make the face of the epoxy block nicely flat. The 45 ° diamond knife in the microtome setup is used to cut sections from the epoxy block with the deposited metal layer embedded in it. This cutting proceeds in the same way a cheese slicer is used to cut cheese, except that the knife is stationary and the microtome moves the epoxy block past the knife. Every time the knife cuts a slab, the epoxy block is automatically moved closer towards the knife (the user can set the desired displacement and hence the desired section-thickness). The microtome can make a numerous amount of circles, automatically creating a lot of sections. The epoxy slabs can be

as thin as 50 nm up to 1 µm using an ultramicrotome. This thickness defines how high the nanowire will be. Transferring the cut sections to a substrate, glass in this research, and removing the epoxy by ozone plasma cleaning will give the free-standing nanowires.
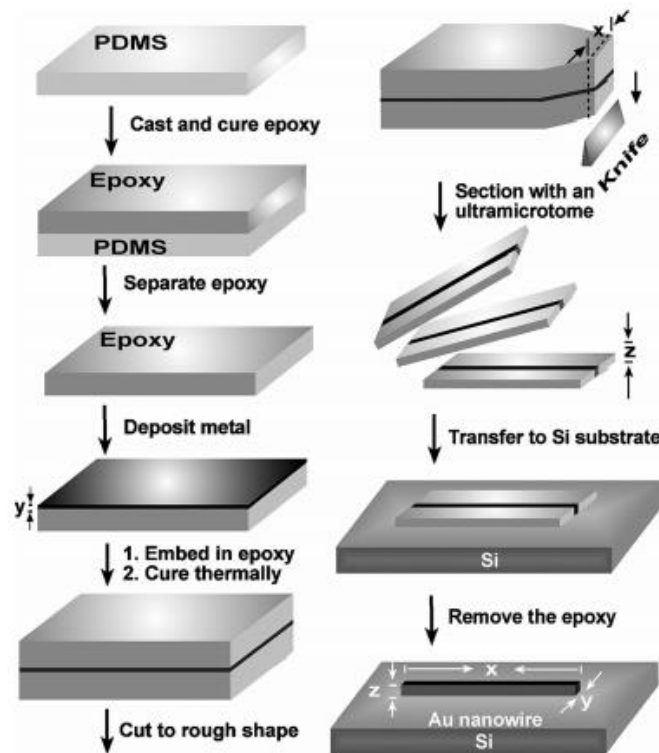
Figure 4.6: Schematic illustration of the steps involved in nanoskiving, used to fabricate metal nanowires. Figure source: [101].

The biggest advantage of using nanoskiving to create these nanostructures is that nanoskiving is relatively cheap and easy. No cleanroom is needed for operation. Another technique to create such structures is Electron-Beam Lithography, which patterns a structure into a resist with an electron beam, over which after development a metal is sputtered or evaporated to create the structure. Although Electron-Beam Lithography has a higher resolution, for the purpose of making the simple bar-shaped nanowires with the dimensions of around 200 x 200 nm in cross-section, nanoskiving is a faster, easier and cheaper way.

A drawback of nanoskiving is the fact that the created nanostructures are hard to handle. After slicing, the sections should be transferred to the desired substrate, which is not easy. Moreover, after epoxy removal, it is not possible to move the individual wires anymore. The wires are either stuck within the epoxy slab, or stuck on the substrate.

Figure 4.7 shows various photographs of how the procedure shown in figure 4.6 looks like in real life. This figure is shown to get a real understanding of how the setup and materials look. The next section will describe how the flow cells used in this study are constructed and how the nanowires are lifted in the flow cell to make it possible for the DNA molecules to hang higher in the flow, where the flow speed is higher than at the bottom of the flow cell, as discussed in section 4.1.
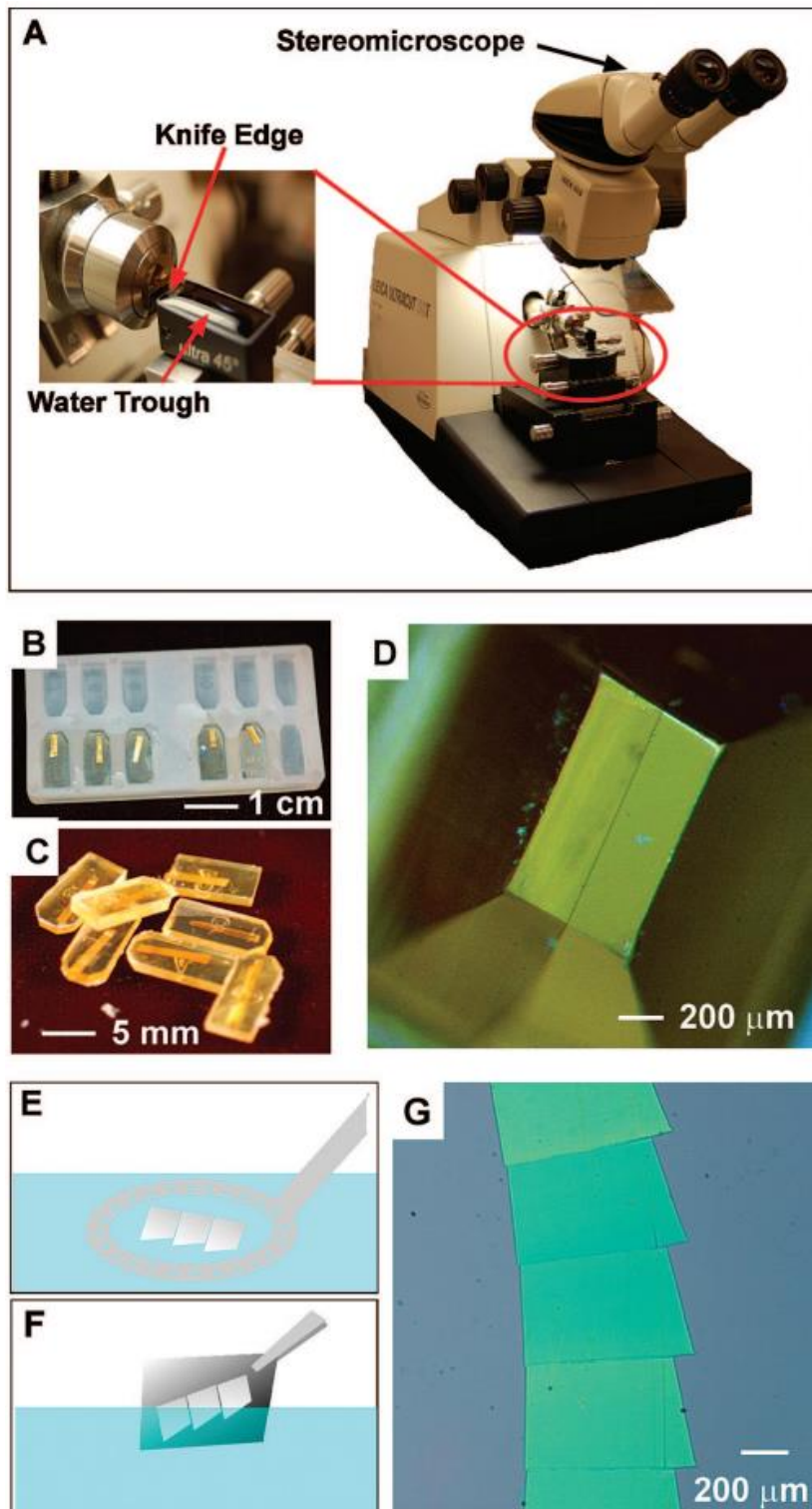
Figure 4.7: A. Ultramicrotome and close-up of the sample, diamond knife and water reservoir that catches the sections at prevents damage of the sections. B. Mold to create the epoxy block in the size that fits the microtome. C. Cured epoxy blocks pressed out of the mold. D. Face of the epoxy block after trimming it with a razor blade in the shape of a trapezoid (done to remember top and bottom, cutting should always be in the same direction) and smoothening it with a glass knife. E. Collection loop (2 mm diameter) used to transfer the sections in a meniscus of water that spans the loop, supporting the sections. F. Direct capture of multiple sections onto a substrate, not used in this research because the coverslips do not fit in the water reservoir and precise deposition is required (the sections cannot be moved anymore after this direct capture). G. Bright-field optical microscopy image of multiple sections on a silicon substrate. Figure source: [101].

4.4   <u>Preparation of flow cell device</u>

This section describes how the flow cell devices are constructed. The device is a version of the devices used in [99], but adapted to the used TIRF microscope setup. As described in section 1.3, the 'standard' flow cell contains a functionalized glass coverslip as bottom part and a PDMS block with the flow channel cut out by the lithography master as the top part. The flow cell is constructed by simply sticking the PDMS on top of the glass. This PDMS adheres to the coverslip and makes it leak-free. It is possible to covalently bind the PDMS to the glass by putting both components in the oxygen plasma cleaner right before putting them together. This is also done in [99]. However, this flow cell devices in this study are only put together through adhesion, which is not leaky and has the advantage of reusing the PDMS flow channels after cleaning (see Appendix D.2 for the cleaning procedure).

     In order to have the nanowires hanging in the flow cell, they must be lifted above the surface. The way to do this is to create a flow channel in the glass coverslip, which is complementary to the PDMS flow channel. Putting the gold nanowires in between the glass and PDMS channel will then result in a hanging wire. As stated in section 1.3 and described in Appendix D.1 and D2, the PDMS channels are created by photolithography. The glass channels on the other hand are created by HF (hydrofluoric acid) etching. The exact protocol of how this etching proceeds, including the important safety guidelines is given in Appendix D.3. The PDMS channels are created using the lithography mask shown in figure 4.8.
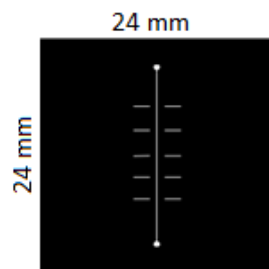
Figure 4.8: Lithography mask used to create the 100 μm wide PDMS channels.

The side five horizontal lines next to each side of the channel are created for alignment purposes. The channels that are etched in the glass coverslips have the exact same structure and makes it easier to align the PDMS top part with the glass bottom part. Moreover, the lines indicate the places where the gold nanowires are places, which makes it easier to find them under the microscope. Thus, every flow cell device will contain five golden nanowires hanging above the glass surface.

     As stated above and described in Appendix D.3, the glass channels are created by HF etching. An important remark about this HF etching is that etching takes place in every direction. The frontside is protected by the chromium layer and the photoresist, but the backside is not, i.e. etching also happens at the back. Moreover, the etching also proceeds sideways. Therefore, the lithography mask used for HF etching needs to hold a smaller shape than the mask used for making the PDMS masters. In this research project, the PDMS masters are 100 μm wide and high, which results in 100 μm wide and high channels. However, the HF etching masks are 20 μ wide, which results into around 56 μm wide and 18 μm deep channels upon etching for 10 minutes (HF etching proceeds in around 1.8 μm/min). This will not result into the wires hanging exactly in the middle of the flow cell, but deeper etching combined with the backside etching on a coverslip of around 160 μm thickness

results in coverslips that are too fragile to handle. An attempt was made to etch around 60 µm deep, but since the etching is not completely uniform, this resulted into etching through the entire coverslip. As shown by the calculation in section 4.1, bringing the DNA molecules up in the flow cell by around 20 µm has already a significant impact on the flow speed compared to the situation at the bottom of the flow cell.

The flow cell devices are created by transferring the microtome section with the collection loop, as illustrated in figure 4.7E, onto the etched glass channels. After baking them at 60 °C for half an hour, the coverslips are put into the ozone plasma cleaner for at least 40 minutes to remove all epoxy. Subsequently, a customized aligner is used to place the PDMS channel on top. The total construction is shown in figure 4.9.

Figure 4.9: Illustration of flow cell device construction.

4.5   Visualization of gold nanowires deposited onto glass substrates

This section describes the experiments performed on gold nanowires deposited onto glass substrates. The hanging nanowires are quite delicate and to see if synthesis onto the nanowires works in general for the microscope setup, this is a relatively easy experiment. Nanowires of 200 and 400 nm thickness are used in this section.

After epoxy removal, the glass surfaces are passivated using dichlorodimethylsilane in order to prevent nonspecific binding to glass. In this way, only molecules bound to the wires should be visible. Unfortunately, it was not possible to see λ phage DNA molecules binding to the wires. The reason for this might be that the change of binding to such a small surface area is highly unlikely for the large λ DNA molecules with only one biotin. However, various other small molecules are used to visualized the nanowires with the TIRF microscope setup. The results are shown in this section. All experiments described in this section are carried out in degassed blocking buffer. The oxygen-scavenging system described in section 3.3 is used in all experiments containing fluorophores.

Labelled streptavidin
During this experiment, streptavidin molecules containing a fluorescent label are directly bound to the biotin synthesized onto the gold nanowires. This is done *in situ* by flowing labelled streptavidin into the flow cell. Figure 4.10 shows two images of Alexa546-labelled (556/573 nm) streptavidin bound to 200 nm gold wires. It is clearly visible that the labelled streptavidin binds to the gold in a particularly high coverage, lighting up the entire wire. Figure 4.10 also shows the result of an identical experiment, which did not have all epoxy successfully removed, showing nonspecific binding of the streptavidin to the epoxy.
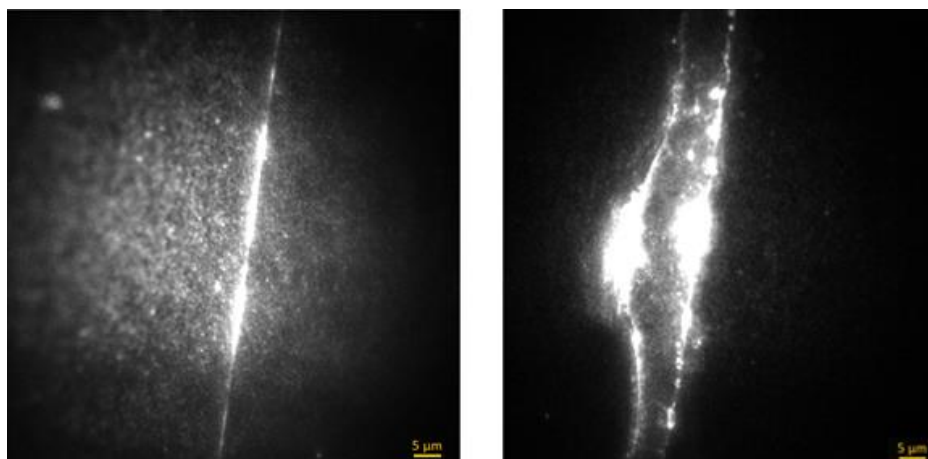
Figure 4.10: TIRF microscope images of Alexa546-streptavidin bound to 200 nm gold wires deposited on glass without (left) and with (right) residual epoxy. These images are single frames, taken with an exposure time of 50 and 40 ms respectively.

Figure 4.11 shows Alexa546-streptavidin bound to a 400 nm gold wire. This image is taken at the boundary of the channel and proves that the nanowires light up due to the fluorescent streptavidin bound and not because of autofluorescence of the gold nanowires itself. Figure 4.11 also shows Alexa660-streptavidin (666/690 nm) bound to a 400 nm gold wire. Despite the decreased contrast, this shows that the procedure is suitable for more colours.
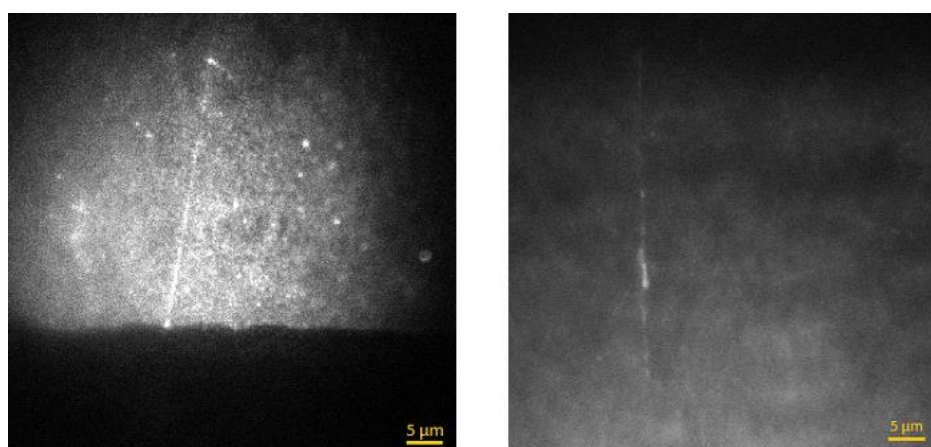
Figure 4.11: TIRF microscope images of Alexa546-streptavidin (left) and Alexa660-streptavidin (right) bound to 400 nm gold wires deposited on glass. The left image shows no autofluorescence. These images are single frames, taken with an exposure time of 30 and 40 ms respectively.

DTT + Alexa660-maleimide

In this experiment, Alexa660 dyes are directly synthesized onto the 200 nm gold nanowires, i.e. this is done *instead* of the cysteine and biotin-NHS incubation described in section 3.2. Since the are no commercially available thiol-fluorophores, DTT is used as a linker between the fluorophore and the gold. The fluorophores are bound to the DTT via the same reaction illustrated in figure 3.7 (the cysteine-maleimide reaction for the labelling of the β clamp). Binding of the DTT to the gold proceeds via self-assembly, as described in section 4.2. This experiment is far from ideal, because DTT has to bind to the fluorophore by one thiol group and to the nanowire by the other thiol group. This is a competing reaction and will result in a mixture of DTT molecules bound to two, one and no fluorophores. To decrease the amount

of DTT molecules bound to two fluorophores, the reaction is performed upon significant dilution. The mixture of 50 µM DTT and 100 µM Alexa660-maleimide in PBS is left at room temperature for one hour and the gold nanowires are incubated in this mixture for two hours. Figure 4.12 shows the result. This visualization worked really well. Note that here the wire outside the channel is fluorescent as well, because fluorescently labelling of the wire took place *before* the flow cell was constructed and not *in situ*.
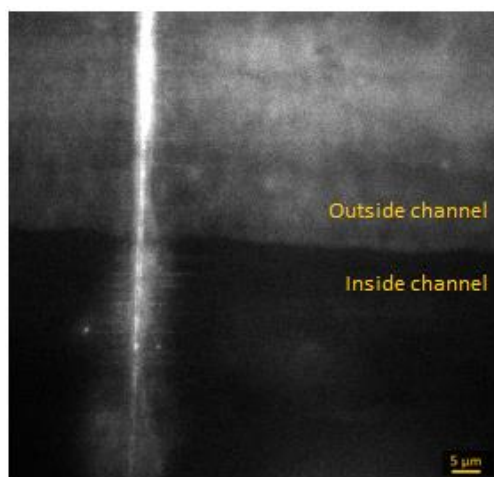
Figure 4.12: TIRF microscope image of 200 nm gold wire deposited on glass visualized with DTT + Alexa660-maleimide. This image is a single frames, taken with an exposure time of 60 ms.

Oligonucleotide

After incubating the 200 nm gold wires with 'normal' streptavidin and constructing the flow cell, 5 nM of oligonucleotides are flown in. As stated above, it was not possible to bind the 48.5 kilobase pairs long λ DNA molecules to the wires deposited on the glass coverslips. Therefore, an attempt was made with short pieces of DNA, i.e. 40 nucleotides long molecules with a biotin at position 40, a Cy3B dye (558/572 nm) at position 1 and an Arto647n (644/669 nm) at position 33. The experiment is only carried out upon excitation of the green dye. The result is shown in figure 4.13. It works and again it proves that the nanowires light up due to the fluorescent molecules bound and not because of autofluorescence of the gold nanowires itself.

Figure 4.13: TIRF microscope image of 200 nm gold wire deposited on glass visualized with the Cy3B fluorophore of an oligonucleotide. This image is a single frames, taken with an exposure time of 90 ms.

M13

Since the oligonucleotides did bind to the nanowires, a longer DNA template is used. 5.3 pM biotinylated M13 templates are bound *in situ* to the gold nanowires and stained with 150 nM SYTOX Orange stain. The result is shown in figure 4.14. The M13 molecules did bind to the nanowires, but the fluorescent dye molecules give a better contrast than the DNA stain that also sticks to the surface. When the nanowires are suspended over the channel, this will not be a problem anymore.
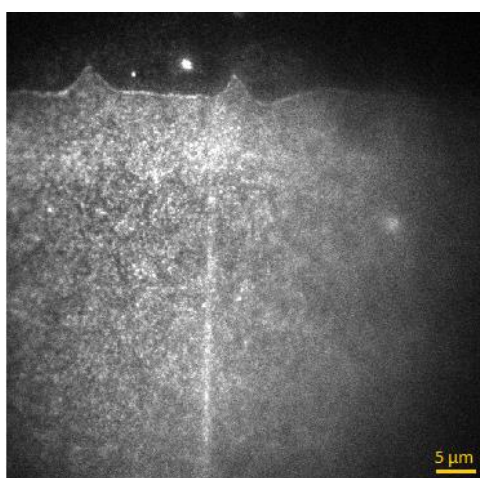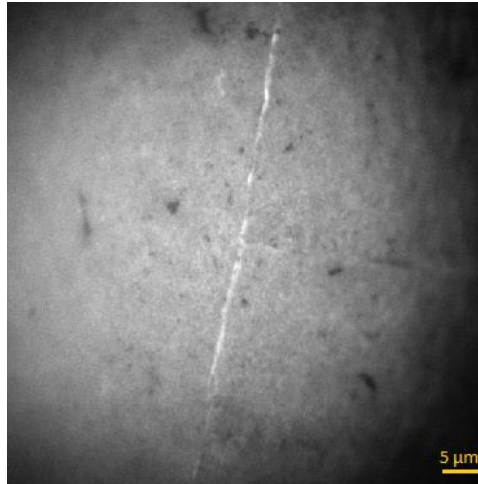

Figure 4.13: TIRF microscope image of 200 nm gold wire deposited on glass visualized with M13 and SYTOX Orange DNA stain. This image is a single frames, taken with an exposure time of 30 ms.

Thus, the gold nanowires deposited on glass coverslips were visualized using different procedures. This work shows that the images are not showing autofluorescence and that it is possible to bind small DNA molecules to the nanowires. The next section will show the work done on nanowires suspended over the channel, i.e. lifted above the glass surface.

4.6   Anchoring DNA to gold nanowires suspended over glass microchannels

This section highlights the results of anchoring DNA to the gold nanowires suspended over the glass channels. Here, the flow cell devices with the etched glass channels, as described in section 4.4, are used. In this study, 400 nm gold wires are used. The reason for these bigger wires is that they are visible through the ocular and makes it therefore easier to search for the wires with the microscope.

Previous work by Kalkman [99] showed that the wires are particularly stable when they are in solution i.e. the wires can withstand very high flow rates and will not break. However, the nanowires break easily when a water surface approaches them. The reason for this is probably the high surface tension of the water-air interface. To overcome this problem, the nanowires should be brought in solution by first flowing in a liquid with a low surface tension, such as methanol or ethanol, at a very low flow rate. After that, the desired buffer can be flown in. Important here is that all solutions that enter the flow cell need to be degassed beforehand, because even the smallest air bubbles can break the wires. Since the first incubation step is cysteamine in ethanol, this step can be done immediately. After that, the incubation in biotin-NHS is performed in degassed PBS (with a higher pH of 8.0), which would induce less air bubbles than $NaHCO_3$, as was used before. Since the nanowires should

always be in solution to prevent damage, all incubation steps need to be performed *in situ*, in a constructed flow cell device.

Unfortunately, it was not possible to obtain any flow cell with functionalized gold nanowires that were still intact. Only broken wires were found. Some wires were completely vanished from the surface or broken before incubation. This was caused by the long plasma cleaning step needed for epoxy removal. Moreover, some etched coverslips broke during the plasma cleaning. However, some broken wires still had pieces of wire hanging in the flow cell and were used to anchor DNA molecules. Although not optimal, this would still result in a proof of principle. Another problem was the alignment of the PDMS top part onto the glass bottom part. This alignment is at the micrometre scale and a microscope and a customized aligner are used to put the pieces together, but this still resulted sometimes into misaligned flow cells. Unfortunately it was found that all correctly aligned flow cell devices did not have any nanowires left after incubation, while some misaligned flow cells had broken pieces still hanging in the flow cell. In these cases, a high concentration (69.6 pM) of λ phage DNA molecules with 150 nM SYTOX Orange DNA stain was flown in. This high concentration was used to have a higher change of binding to the small surface of the wires. As stated in the previous section, it was not possible to bind the long λ DNA molecules to the nanowires deposited on the bottom of the flow cell, but in this case, the bulk of DNA moving in the centre of the flow cell made it possible for the DNA molecules to attach to the nanowire.

Some DNA was indeed found to bind to the 'nanowire arm' (i.e. a piece of the broken nanowire still sticking out in the flow cell). Figure 4.14 shows the optical image of the nanowire arm and the misalignment of the flow cell.
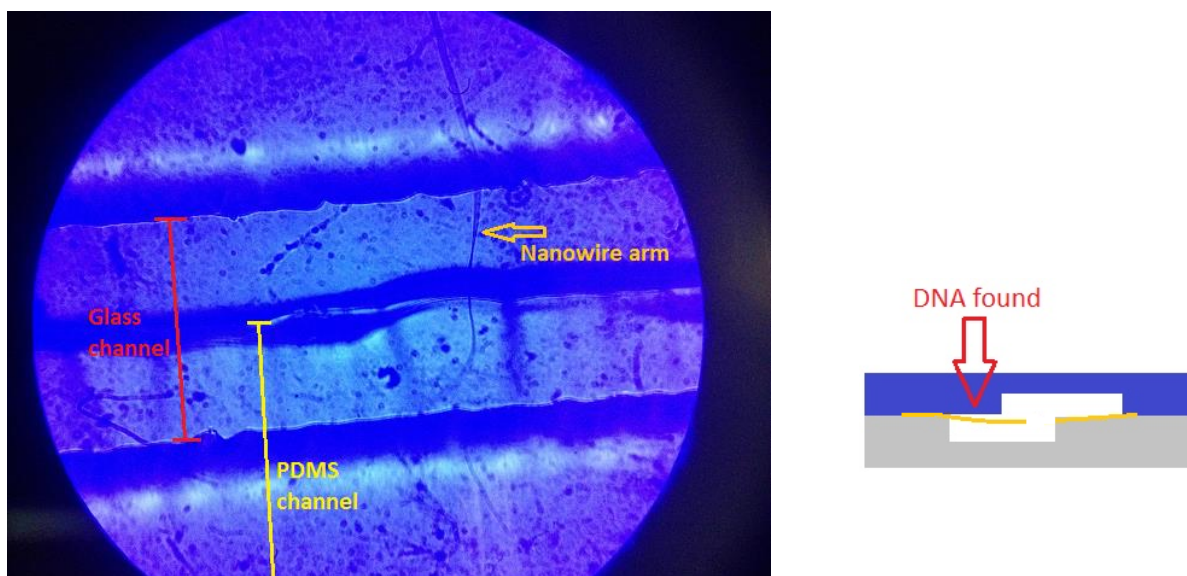
Figure 4.14: *Optical image of nanowire arm in misaligned flow cell (left) and illustration of misalignment and broken nanowire (right). There was DNA found at the orange arrow on the optical image and the red arrow at the illustration.*

Figure 4.15 shows the fluorescence microscopy image of the DNA hanging on the nanowire. As the nanowires are lifted in the flow cell, TIRF microscopy could not be used anymore. Thus, all images are taken in epifluorescence (around 19 W/cm^2). The λ DNA molecule visible in figure 4.15 is not full length, it is broken. There is a lot of undesired fluorescence, but this could be due to sticking of the Alexa546-streptavidin to the wire and the top PDMS. Figure 4.15 also shows a kymograph of the DNA molecule. This kymograph is made during a stop-

flow experiment, i.e. it shows the length of the flow-stretched DNA molecule upon instantaneously changing from a flow to no flow and back. This kymograph proofs that indeed a DNA molecule is hanging on the nanowire arm. It is not a static artefact. Thus, it is possible to bind DNA to a nanowire hanging in a flow cell.
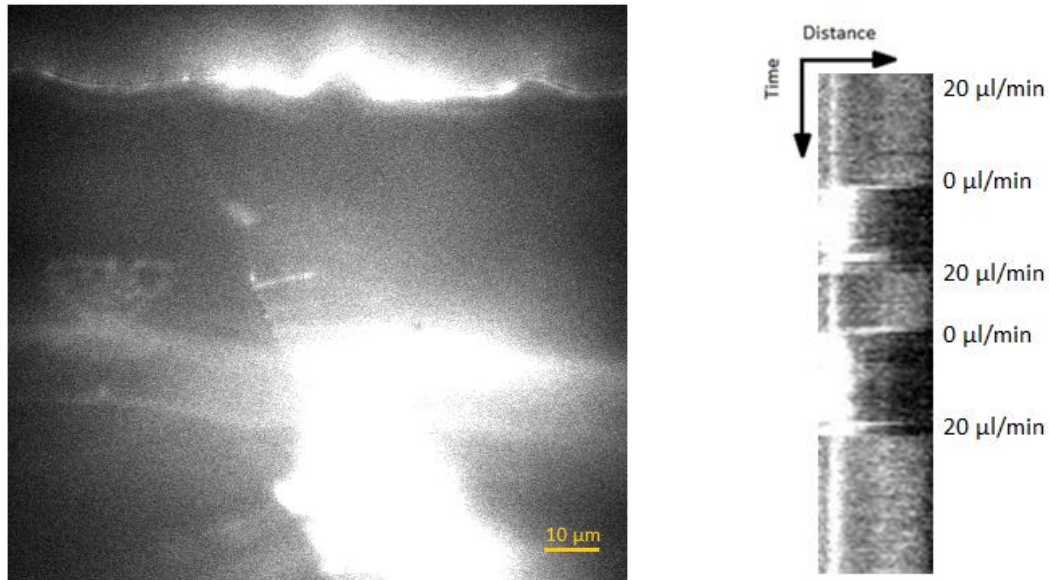
Figure 4.15: The left image is a fluorescence microscope image of a piece of λ DNA, stained with SYTOX Orange, hanging on a piece of 400 nm gold wire. Flow is coming in from the left at a flow rate of 20 µl/min. This image is a single frame, taken with an exposure time of 200 ms. The right image is a kymograph of the same piece of DNA, undergoing a stop-flow experiment, proving that it is DNA hanging onto the wire.

This experiment is performed again, but it also resulted in a broken nanowire arm sticking out in a misaligned flow cell. However, multiple DNA molecules were found to hang on the nanowire. This 'curtain' of DNA can be seen in figure 4.16.

Figure 4.16: Fluorescence microscope image of a 'curtain' of multiple λ DNA molecules, stained with SYTOX Orange, hanging on a piece of 400 nm gold wire. Flow is coming in from the left at a flow rate of 1 µl/min. This image is a single frame, taken with an exposure time of 150 ms.

Figure 4.16 shows multiple long λ DNA molecules hanging in the flow cell. However, the flow rate used is only 1 μl/min and still all DNA molecules are stretched out. Looking at figure 2.6 of the λ phage DNA length calibration, the molecules need a much higher flow rate to be stretched-out. Such a low flow rate would result in the DNA coiling up and being far from fully stretched. Hence, this figure clearly demonstrates what is written in section 4.1, i.e. that bringing the DNA molecules up in the flow would benefit from a significant enhanced flow profile and would not require such a high flow rate as if it were attached to the bottom surface of the flow cell. This experiment here is a significant proof of principle. Moreover, even lower flow rates than 1 μl/min should be possible (see suggestions for future work in section 4.8.).

Besides lowering the flow rate, also the effect upon increasing the flow rate was investigated. As shown in figure 4.15, suddenly changing from zero flow to 20 μl/min did not harm the DNA. The DNA molecules remain intact and bound to the wire, even upon increasing the flow rate up to 250 μl/min. This suggests that the DNA molecules might not be bound to the nanowire via biotin-streptavidin linkage, but are wrapped around the wire by simple running into the wire. In that case, the DNA molecules can only break by breaking the DNA backbone and not by detachment of the biotin-streptavidin bond. A study, in which short ds-DNA molecules were pulled with an AFM tip, showed that DNA molecules can withstand forces up to 1700 pN [102]. On the other hand, AFM studies showed that it takes 105 ± 60 pN to detach biotin from streptavidin [103]. Thus, it takes a significant lower force to break the biotin-streptavidin bond than to break the DNA backbone. The kymograph of figure 4.17 shows that some DNA molecule were indeed wrapped around the wire. In this figure, a DNA molecule is wrapped around the wire at the middle of its length, resulting into two arms of same size. As time proceeds, the flow induces a shift of the centre where it is bound and makes the DNA slide along the wire. This resulted in the growth of one arm and the shrinkage of the other by the same amount.
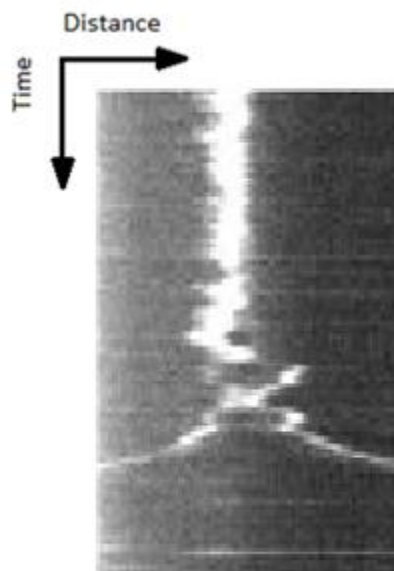

Figure 4.17: Kymograph of a single λ DNA molecule wrapped around a nanowire. As time proceeds, the two arms of identical length are pulled apart by growth of one arm and shrinkage of the other arm due to flow that makes the DN slide off the nanowire.

However, the effect of the curtain of DNA was also investigated by inducing a backflow, i.e. flow in the opposite direction. Still, this curtain of DNA was visible. When the flow was put back to the normal direction, the curtain of DNA still looked like figure 4.16. If all DNA molecules we not bound to the wire, but wrapped around it, it is likely that they would fall off during this reverse flow. Note, however, that this experiment is performed after washing out all DNA molecules that were not bound to the wire, so that no new DNA molecules can bind after others has left. Thus, the fact that there was still a curtain of DNA hanging on the wire, means that the DNA molecules indeed remain bound. This would suggest both molecules attached to the DNA via the biotin-streptavidin linkage and DNA wrapped around the wire. The reason that the truly bound DNA molecules survive high flow speeds could be due to the fact that the nanowire is broken and that this nanowire arm can move within the flow and thus act as some sort of spring that reduces the damage to the DNA. It is clearly visible that higher flow rates result into enormous bending of the nanowire arm in the direction of the flow. However, this would require more work.

4.7   Conclusion

The idea behind this research project was that bringing the DNA molecules higher in the flow cell, instead of tethering them to the bottom surface, would benefit from a better (i.e. more stable) flow profile and a significant lower flow rate. The goal was to use gold nanowires suspended over etched glass channels as a rope for DNA molecules to hang onto.

The gold nanowires are successfully created using nanoskiving. Embedding a hundreds of nanometre thick gold layer in epoxy made it possible to slide hundreds of nanometre thick sections using an ultramicrotome. The epoxy could be removed in the plasma cleaner, leaving 200 or 400 nm thick gold wires behind. Direct deposition of the nanowires onto a glass substrate made it possible to check the functionalization procedure of the gold nanowires. The absence of a fluorescent signal outside the channel proved successful *in situ* binding of fluorescent molecules and hence successful surface chemistry.

Around 18 µm deep glass channels were successfully created using HF etching. Alignment of the glass and PDMS channels remains difficult. The incubation steps were not successful in keeping the nanowires intact. Only broken nanowires were examined. However, the incubation itself was successful and multiple DNA molecules were found to bind to the broken pieces of gold nanowire that were sticking out in the flow cell. Lowering the flow rate to 1 µl/min and still having stretched-out λ DNA molecules proved that the flow profile was indeed enhanced upon bringing the DNA molecules up in the flow cell. This study is a proof of principle.

It was found that not all DNA molecules hanging on the gold nanowire were bound through biotin-streptavidin linkage. Some were found to be wrapped around the wire, simply by running into it. However, inducing backflow and high flow rates suggested that there are also DNA molecules that are bound in the way they should. However, this requires more work.

4.8 Future perspective

This section describes a couple of suggestions for future work. As stated in the conclusions, the work done is a proof of principle. However, more work is required to come up with a result that shows not only qualitatively but also quantitatively what the effect is of bringing the DNA molecules up in the flow cell.

The main issue is that all wires break during the incubation steps. These incubation steps are performed by manually flowing in all solutions, starting from the ethanol with a low surface tension. This should be done in a slower and a more controlled way. The best way to do this, is by immediately putting the flow cell device under the microscope and using the syringe pump to flow in the ethanol at the slow rate of 1 μl/min while having the possibility to check during each step if the wires are still intact. Another point is that all buffers that enter the flow cell should be well degassed beforehand to prevent any air bubbles that might break the wires. Moreover, this work should be performed in a successfully aligned flow cell. This simply requires more practice, because it is a manual procedure.

For the experiment itself, the best way is to not use fluorescently labelled streptavidin. This resulted into too much fluorescence, as can be seen in the microscope images, and made it hard to see the individual DNA molecules. Another point is that a syringe with a smaller diameter should be used to make it possible to pump at lower flow rates than 1 μl/min. In that case, a similar plot as figure 2.6 can be made, where the flow-stretched length is given as a function of flow rate and the minimal flow rate required for full-stretched length can be given.

5.   Conclusion

In the first research project, the effect of flow speed and buffer composition on the flow-stretched length of λ phage DNA was investigated. It was found that there is a saturation behaviour for the flow-stretched length of λ phage DNA that is tethered to the bottom surface in a flow cell. This maximum length is reached at flow rates between 10 and 20 μl/min for rectangular flow cells with dimensions of 100 μm height and 500 μm width. In this saturation regime, the conversion factor for the microscope setup in the Van Oijen Lab is around 650 base pairs per pixel. Moreover, it was found that the presence of divalent magnesium ions in the buffer solutions has a negative influence on the stretched-out length, due to interactions with the negatively charged DNA backbone. As a result, a conversion sheet, which shows the actual length and the conversion factor for the amount of base pairs per μm as a function of both the flow rate and the type of buffer, is obtained. This successful length calibration makes it possible to determine for example replication rates (i.e. the amount of base pairs per second replicated) more precisely by measuring the growth in pixels with the microscope camera and converting it to physical length for the experimental conditions used. At last, an attempt was made to investigate the force profile along flow-stretched λ DNA. Some rough approximation were made to show that this is in the order of 1-12 pN with the lowest force on the tip of the DNA.

In the second research project, the role of the *Escherichia coli* β clamp protein in DNA replication is investigated by carrying out M13 rolling-circle replication experiments. The β clamp is a dimeric ring that is loaded onto the DNA by the clamp-loader complex. The β clamp is opened and assembled around the DNA via ATP hydrolysis. Once bound to the DNA, the β clamp can slide along the DNA strand. To visualize the β clamps, the proteins were labelled with fluorescent molecules, yielding labelling efficiencies up to 90.4 %. It was proven that the labelled proteins maintained their functionality in DNA replication, by simultaneously imaging replication product growth and displacement of the β clamp at the tip of the replication product. It was found that the β clamps were left behind on the replication product after formation of each Okazaki fragment. Analysis showed that the average distance between the β clamp, i.e. the length of the Okazaki fragments, is 529 ± 8 base pairs long, assuming equal affinity of the labelled and the non-labelled β clamps to the DNA. Moreover, it was shown that no Okazaki fragments were formed in the absence of DnaG primase. Without DnaG, only very short replication products were visible. The reason for this can be found in strand displacement synthesis. Long replication products were not visualized, but since these products consist of ss-DNA, it is possible that they were not visible due to the very low affinity of YO-PRO-1 intercalating DNA stain upon binding to ss-DNA. The presence or absence of long products cannot be concluded from this research

In the third project, an attempt was made to bring DNA molecules up in the flow by attaching them to a suspended gold nanowire. The idea behind this research project was that bringing the DNA molecules higher in the flow cell, instead of tethering them to the bottom surface, would benefit from a better (i.e. more stable) flow profile and a significant lower flow rate. The gold nanowires were successfully created using nanoskiving. Direct deposition of the nanowires onto a glass substrate made it possible to check the functionalization procedure of the gold nanowires. The absence of a fluorescent signal outside the channel proved successful *in situ* binding of fluorescent molecules and hence successful surface chemistry. To bring the nanowires up in the flow, glass channels of around 18 μm deep were successfully created using HF etching. Unfortunately, the incubation steps

were not successful in keeping the nanowires intact. Only broken nanowires were examined. However, λ phage DNA molecules were successfully synthesised on pieces of 400 nm thick gold wires that were sticking out in the middle of the flow cell. Lowering the flow rate to 1 μl/min and still having stretched-out λ DNA molecules proved that the flow profile was indeed enhanced upon bringing the DNA molecules up in the flow cell. This was a proof of principle study and future work would require incubation steps in a more controlled way, i.e. in a constant flow system with a syringe pump at a low flow rate, in order to keep the nanowires intact.

All in all, the three research projects presented in this thesis successfully used single-molecule tools to study DNA processes. All research projects contain real-time, single-molecule observation of DNA processes in a flow cell, where a laminar flow is used to stretch out multiple DNA molecules at the same time. It was shown that the single-molecule tools, such as DNA visualization through fluorescently staining, protein tracking by fluorescently labelling and TIRF microscopy are useful tools for investigating the DNA processes described above.

Acknowledgements

This work could not have been possible without the help of a number of people. At first I would like to thank Antoine van Oijen for giving me the opportunity to do my final research project is his group, I had a great time in the Single-Molecule Biophysics group. Moreover, I would like thank Antoine for his advice and support during my application for and obtaining of a PhD position in a different research group. I would like to thank Sarah Stratmann for her daily supervision and her help on all research projects described in this thesis. Her great expertise in the field of biochemistry has definitely taught me a lot. For the λ phage DNA length calibration research project, I would like to thank Enrico Monachino for his share in the project. The nanowire project could not have been possible without our collaborators, and for that I would like to thank Pieter Oomen and Patty Mulder from the Pharmaceutical Analysis group for their work on photolithography and HF etching, and Zhiyuan Zhao, Yanxi Zhang, Parisa Pourhossein and Ryan Chiechi from the RCCLab for their work on nanowire fabrication with nanoskiving.

References

[1]   M. Bischof, "Some remarks on the history of biophysics and its future". In: *The Current Development of Biophysics*, eds. C.L. Zhang, F.A. Popp & M. Bischof. Hangzhou, China: Hangzhou University Press, 10-21, (1996).

[2]   D. Burns, *An Introduction to Biophysics,* New York: Macmillan, (1921).

[3]   J.R. Loofbourow, "Borderland problems in biology and physics", *Rev. Mod. Phys.*, **12**, 267-358*,* (1940).

[4]   H. Frauenfelder, P.G. Wolynes & R.H. Austin, "Biological physics", *Rev. Mod. Phys.*, **71(2)**, S419-S430, (1999).

[5]   J.D. Watson & F.H.C. Crick, "A structure for Deoxyribose Nucleic Acid", *Nature*, **171**, 737-738, (1953).

[6]   G.S. Hurst, M.H. Nayfeh & J.P. Young, "A demonstration of one-atom detection", *Appl. Phys. Lett.*, **30**, 229-231, (1977).

[7]   W.E. Moerner & L. Kador, "Optical detection and spectroscopy of single molecules in a solid", *Phys. Rev. Lett.*, **62**, 2535-2538*,* (1989).

[8]   E.B. Shera, N.K. Seitzinger, L.M. Davis, R.A. Keller & S.A. Soper, "Detection of single fluorescent molecules", *Chem. Phys. Lett.,* **174**, 553-557, (1990).

[9]   C.E. Perez & R.L. Gonzales Jr., "*In vitro* and *in vivo* single-molecule fluorescence imaging of ribosome-catalyzed protein synthesis", *Curr. Opin. Chem. Biol.*, **15(6)**, 853-863, (2011).

[10]   E.R. Nichols & D.B. Craig, "Single molecule assays reveal differences between in vitro and in vivo synthesized β-galactosidase", *Protein J.*, **27**, 376-383, (2008).

[11]   E.A. Abbondanzieri, W.J. Greenleaf, J.W. Shaevitz, R. Landick & S.M. Blok, "Direct observation of base-pair stepping by RNA polymerase", *Nature*, **438(7064)**, 460-465, (2005).

[12]   R. Yasuda, H. Noji, K.J. Kinosita Jr. & M. Yoshida, "F1-ATPase is a highly efficient molecular motor that rotates with discrete 120° steps", *Cell*, **93**, 1117-1124, (1998).

[13]   S.J. Koch, A. Shundrovsky, B.C. Jantzen & M.D. Wang, "Probing protein-DNA interactions by unzipping a single DNA double helix", *Biophys. J.*, **83(2)**, 1098-1105, (2002).

[14]   M. Carrion-Vazquez, A.F. Oberhauser, S.B. Fowler, P.E. Marszalek, S.E. Broedel, J. Clarke & J.M. Fernandez, "Mechanical and chemical unfolding of a single protein: a comparison", *Proc. Natl. Acad. Sci. U.S.A.*, **96(7)**, 3694-3699, (1999).

[15]   C. Cecconi, E.A. Shank, C. Bustamante & S. Marqusee, "Direct observation of the three-state folding of a single protein molecule", *Science*, **309(5743)**, 2057-2060, (2005).

[16]   X. Zhuang & M. Rief, "Single-molecule folding", *Curr. Opin. Struc. Biol.*, **13**, 88-97*,* (2003).

[17]   J.M. Fernandez & H.B. Li, "Force-clamp spectroscopy monitors the folding trajectory of a single protein", *Science*, **303(5664)**, 1674-1678, (2004).

[18]   N. Gregerson, P. Bross, S. Vang 7 J.H. Christensen, "Protein misfolding and human disease", *Annu. Rev. Genom. Hum. G.*, **7**, 103-124, (2006).

[19]   A. Pastore & P. Temussi, "Protein aggregation and misfolding: good or evil?", *J. Phys. Condens. Matter,* **24(24)**, 244101 (1-9), (2012).

[20]   W.J. Greenleaf, M.T. Woodside & S.M. Block, "High-resolution, single-molecule measurements of biomolecular motion", *Annu. Rev. Biophys. Biomol. Struct.*, **36**, 171-190, (2007).

[21]   D.J. Brockwell, "Probing the mechanical stability of proteins using the atomic force microscope", *Biochem, Soc. T.*, **35(6)**, 1564-1568, (2007).

[22]   A.P. Wiita, S.R.K. Ainavarapu, H.H. Huang & J.M. Fernandez, "Force-dependent chemical kinetics of disulfide bond reduction observed with single-molecule techniques", *Proc. Natl. Acad. Sci. U.S.A.*, **103(19)**, 7222-7227, (2006).

[23]   R.B. Best, D.J. Brockwell, J.L. Toca-Herrera, A.W. Blake, D.A. Smith, S.E. Radford & J. Clarke, "Force mode atomic force microscopy as a tool for protein folding studies", *Anal. Chem. Acta,* **479(1)**, 87-105, (2003).

[24]   N. Crampton, K. Alzahrani, G.S. Beddard, S.D. Cornell & D.J. Brockwell, "Mechanically unfolding protein L using a laser-feedback-controlled cantilever", *Biophys. J.*, **100(7)**, 1800-1809, (2011).

[25]   K.C. Neuman & A. Nagy, "Single-molecule force spectroscopy: optical tweezers, magnetic tweezers and atomic force microscopy", *Nat. Methods*, **5(6)**, 491-505, (2008).

[26]   "Measuring twisting modulus of DNA", *JAEA R&D Review* (2007), section 10-3.
http://jolisfukyu.tokai-sc.jaea.go.jp/fukyu/mirai-en/2007/

[27]   Y. Seol, G.M. Skinner & K. Visscher, "Elastic properties of a single-stranded charged homopolymeric ribonucleotide", *Phys. Rev. Lett.*, **93(11)**, 118102 (1-4), (2004).

[28]   M.S.Z. Kellermayer, S.B. Smith, H.L. Granzier & C. Bustamante, "Folding-unfolding transitions in single titin molecules characterized with laser tweezers", *Science*, **276**, 1112-1116, (1997).

[29]   K.C. Neuman, E.H. Chadd, G.F. Liou, K. Bergman & S.M. Block, "Characterization of photodamage to *Escherichia coli* in optical traps", *Biophys. J.*, **77(5)**, 2856-2863, (1999).

[30]   J. Gore, Z. Bryant, M. Nöllmann, M.U. Le, N.R. Cozzarelli & C. Bustamante, "DNA overwinds when stretched", *Nature*, **442**, 836-839, (2006).

[31]   D. Salerno, D. Brogioli, V. Cassina, D. Turchi, G.L. Beretta, D. Seruggia, R. Ziano, F. Zunino & F. Mantegazza, "Magnetic tweezers measurements of the nanomechanical properties of DNA in the presence of drugs", *Nucl. Acids Res.*, **38(20),** 7089-7099, (2010).

[32]   A. Trache & G.A. Meininger, "Total internal reflection fluorescence (TIRF) microscopy", *Curr. Protoc. Microbiol.*, **10**, 2A.2.1-2A.2.22, (2008).

[33]   M. Kramer & K. Zeiss, "Evanescent waves in microscopy", *Photonik*, **2**, 42-44, (2004).

[34]   W.E. Moerner & D.P. Fromm, "Methods of single-molecule fluorescence spectroscopy and microscopy", *Rev. Sci. Instrum.*, **74(8)**, 3597-3619, (2003).

[35]   R.A. Bhat, T. Lahaye & R. Panstruga, "The visible touch: *in planta* visualization of protein-protein interactions by fluorophore-based methods", *Plant Methods*, **2(12)**, 12-26, (2006).

[36]   G. Danuser & C.M. Waterman-Storer, "Quantitative fluorescent speckle microscopy of cytoskeleton dynamics", *Annu. Rev. Biophys. Biomol. Struct.*, **35**, 361-387, (2006).

[37]   J. Schmoranzer, M. Goulian, D. Axelrod & S.M. Simon, "Imaging constitutive exocytosis with total internal reflection fluorescence microscopy", *J. Cell Biol.*, **149(1)**, 23-32, (2000).

[38]   A. Yildiz & P.R. Selvin, "Fluorescence imaging with one nanometer accuracy: application to molecular motion", *Acc. Chem. Res.*, **38**, 574-582, (2005).

[39]   S.J. Sophia, V. Premnath & E.W. Merrill, "Poly(ethylene oxide) grafted to silicon surfaces: grafting density and protein adsorption", *Macromolecules,* **31(15)**, 5059-5070, (1998).

[40]   E.M. Lederberg, "Lysogenicity in *E. coli* K-12", *Genetics*, **36**, 560 (abstract), (1951).

[41]   S.V. Rajagopala, S. Casjens & P. Uetz, "The protein interaction map of bacteriophage lambda", *BMC Microbiol.*, **11(1)**, 213(1-15), (2011).

[42]   G.J. Tortora, *Microbiology. An introduction*, 8th ed., San Francisco: Pearson Benjamin Cummings, (2004).

[43]   M. Better & D. Freifelder, "Studies on the replication of *Escherichia coli* phage λ DNA I. The kinetics of DNA replication and requirements for the generation of rolling-circles", *Virology*, **126(1)**, 168-182, (1983).

[44]   C. Helms, M.Y. Graham, J.E. Dutchik & M.V. Olson, "A new method for purifying lambda DNA from phage lysates", *DNA*, **4(1)**, 39-49, (1985).

[45]   R.V. Santelli & L.D. Navarro-Cattapan, "A simplified CsCl protocol for lambda DNA purification: no enzymatic treatment/one phenol extraction", *Genet. Mol. Biol.*, **23(1)**, 65-66, (2000).

[46]   A.M. Campbell, "Bacteriophages". In: *Escherichia coli and Salmonella: cellular and molecular biology*, eds. F.C. Niedhardt. Washington D.C.: ASM Press, (1996).

[47]   M. Krishnan, I. Mönch & P. Schwille, "Spontaneous stretching of DNA in a two-dimensional nanoslit", *Nano Lett.*, **7(5)**, 1270-1275, (2007).

[48]   N.A. Tanner & A.M. van Oijen, "Visualizing DNA replication at the single-molecule level", *Methods Enzymol.*, **475**, 259-278, (2010).

[49]   SYTOX® Orange nucleic acid stain (S-11368), product information. Molecular probes 11368, (2001).

[50]   X. Yan, R.C. Habbersett, J.M. Cordek, J.P. Nolan, T.M. Yoshida, J.H. Jett & B.L. Marrone, "Development of a mechanism-based, DNA staining protocol using SYTOX Orange nucleic acid stain and DNA fragment sizing flow cytometry", *Anal. Biochem.*, **286**, 138-148, (2000).

[51]   T.T. Perkins, D.E. Smith, R.G. Larson & S. Chu, "Stretching a single tethered polymer in a uniform flow", *Science*, **268(5207)**, 83-87, (1995).

[52]   J.F. Marko & E.D. Siggia, "Stretching DNA", *Macromolecules*, **28**, 8759-8770, (1995).

[53]   C. Bustamante, S.B. Smith, J. Liphardt & D. Smith, "Single-molecule studies of DNA mechanics", *Curr. Opin. Struct. Biol.*, **10(3)**, 279-285, (2000).

[54]   H. Fu, H. Chen, C.G. Koh & C.T. Lim, "Effects of magnesium salt concentrations on B-DNA overstretching transition", *Eur. Phys. J. E Soft Matter,* **29(1)**, 45-49, (2009).

[55]   T.K Chiu & R.E. Dickerson, "1 A crystal structures of B-DNA reveal sequence-specific binding and groove-specific bending of DNA by magnesium and calcium", *J. Mol. Biol.*, **301(4)**, 915-945, (2000).

[56]   L. Yang, K. Arora, W.A. Beard, S.H. Wilson & T. Schlick, "Critical role of magnesium ions in DNA polymerase β's closing and active site assembly", *J. Am. Chem. Soc.*, **126**, 8441-8453, (2004).

[57]   T.R. Strick, J.F. Allemand, D. Bensimon & V. Croquette, "Behavior of supercoiled DNA", *Biophys. J.*, **74(4)**, 2016-2028, (1998).

[58]   W. Messer & J. Zakrzewska-Czerwińska, "*Streptomyces* and *Escherichia coli*, model organisms for the analysis of the initiation of bacterial chromosome replication", *Arch. Immunol. Ther. Ex.*, **50**, 393-398, (2002).

[59]   S. Sundararaj, A. Guo, B. Habibi-Nazhad, M. Rouani, P. Stothard, M. Ellison & D.S. Wishart, "The CyberCell Database (CCDB): a comprehensive, self-updating, rational database to coordinate and facilitate in silico modeling of Escherichia coli" *Nucl. Acids Res.*, **32(Database issue)**, D293-D295, (2004).

[60]   F.R. Blattner, G. Plunkett 3rd, C.A. Bloch, N.T. Perna, V. Burland, M. Riley, J. Collado-Vides, J.D. Glasner, C.K. Rode, G.F. Mayhew, J. Gregor, N.W. Davis, H.A. Kirkpatrick, M.A. Goeded, D.J. Rose, B. Mau & Y. Shao, "The complete genome sequence of Escherichia coli K-12", *Science*, **277(5331)**, 1453-1462, (1997).

[61]   M. Chandler, R.E. Bird & L. Caro, "The replication time of the *Escherichia coli* K12 chromosome as a function of cell doubling time", *J. Mol. Biol.*, **94(1)**, 127-132, (1975).

[62]   J.W. Drake, E.F. Allen, S.A. Forsberg, R.M. Preparata & E.O. Greening, "Genetic control of mutation rates in bacteriophage T4", *Nature*, **221(5186)**, 1128-1132, (1969).

[63]   N.A. Tanner, S.M. Hamdan, S. Jergic, K.V. Loscha, P.M. Schaeffer, N.E. Dixon & A.M. van Oijen, "Single-molecule studies of fork dynamics in *Escherichia coli* DNA replication", *Nat. Struct. Mol. Biol.*, **15**, 170-176, (2008).

[64]   N.Y. Yao & M. O'Donnell, "Snapshot: the replisome", *Cell*, **141(6)**, 1088-1089, (2010).

[65]   S.M. Hamdan & C.C. Richardson, "Motors, switches, and contacts in the replisome", *Annu. Rev. Biochem.*, **78**, 205-243, (2009).

[66]   J.A. Kobori & A. Kornberg, "The *Escherichia coli dnaC* gene product. III. Properties of the dnaB-dnaC protein complex", *J. Biol. Chem.*, **257(22)**, 13770-13775, (1982).

[67]   Z. Kelman & M. O'Donnell, "DNA polymerase III holoenzyme: structure and function of a chromosomal replication machine", *Annu. Rev. Biochem.*, **64**, 171-200, (1995).

[68]   M. O'Donnell, "β sliding clamp dynamics within *E. coli* DNA polymerase III holoenzyme", *Ann. N. Y. Acad. Sci.*, **726(1)**, 144-155, (1994).

[69]   F.J. López de Saro & M. O'Donnell, "Interaction of the β sliding clamp with MutS, ligase, and DNA polymerase I", *Proc. Natl. Acad. Sci. U.S.A.*, **98**, 8376-8380, (2001).

[70]   M. Hedglin, R. Kumar & S.J. Benkovic, "Replication clamps and clamp loaders", *Cold Spring Harb. Perspect. Biol.*, **5(4)**, 010165(1-19), (2013).

[71]   G.P. Glover & C.S. McHenry, "The χψ subunits of DNA polymerase III holoenzyme bind to single-stranded DNA-binding protein (SSB) and facilitate replication of an SSB-coated template", *J. Biol. Chem.*, **273(36)**, 23476-23484, (1998).

[72]   P.C. Hanawalt & R.H. Haynes, "The repair of DNA", *Sci. Am.,* **216(2)**, 36-43, (1967).

[73]   I.J. Molineux, A. Pauli & M.L. Gefter, "Physical studies of the interaction between Escherichia coli DNA binding protein and nucleic acids", *Nucleic Acids Rev.*, **2(10)**, 1821-1837, (1975).

[74] R. Shereda, A. Kozlov, T. Lohman, M. Cox & J. Keck, "SSB as an organizer/mobilizer of genome maintenance complexes", *Crit. Rev. Biochem. Mol. Biol.*, **43**, 289-318, (2008).

[75] A.M. van Oijen & J.J. Loparo, "Single-molecule studies of the replisome", *Annu. Rev. Biophys.*, **39**, 429-448, (2010).

[76] T. Ogawa & T. Okazaki, "Discontinuous DNA replication", *Annu. Rev. Biochem.*, **49**, 421-457, (1980).

[77] K. Sakabe & R. Okazaki, "A unique property of the replicating region of chromosomal DNA", *Biochim. Biophys. Acta*, **129(3)**, 651-654, (1966).

[78] D.N. Frick & C.C. Richardson, "DNA primases", *Annu. Rev. Biochem.*, **70**, 39-80, (2001).

[79] B.M. Alberts, J. Barry, P. Bedinger, T. Formosa, C.V. Jongeneel & K.N. Kreuzer, "Studies on DNA replication in the bacteriophage T4 in vitro system", *Cold Spring Harb. Symp. Quant. Biol.*, **47**, 655-668, (1983).

[80] S.M. Hamdan, J.J. Loparo, M. Takahashi, C.C. Richardson & A.M. van Oijen, "Dynamics of DNA replication loops reveal temporal control of lagging-strand synthesis", *Nature*, **457(7227)**, 336-339, (2009).

[81] B. Alberts, A. Johnson, J. Lewis, M. Raff, K. Roberts & P. Walter, *Molecular biology of the cell*, 5th ed., New York: Garland Science, (2008).

[82] N.A. Tanner, G. Tolun, J.J. Loparo, S. Jergic, J.D. Griffith, N.E. Dixon & A.M. van Oijen, "*E. coli* DNA replication in the absence of free β clamps", *EMBO J.*, **30(9)**, 1830-1840, (2011).

[83] A. Gahlmann & W.E. Moerner, "Exploring bacterial cell biology with single-molecule tracking and super-resolution imaging", *Nat. Rev. Microbiol.*, **12(1)**, 9-22, (2014).

[84] C.O. Paschall, J.A. Thompson, M.R. Marzahn, A. Chiraniya, J.C. Hayner, M. O'Donnell, A.H. Robbins, R. McKenna & L.B. Bloom, "The *Escherichia coli* clamp loader can actively pry open the β-sliding clamp", *J. Biol. Chem.*, **286(49)**, 42704-42714, (2011).

[85] P.T. Stukenberg, P.S. Studwell-Vaughan & M. O'Donnell, "Mechanism of the sliding β-clamp of DNA polymerase III holoenzyme", *J. Biol. Chem.*, **266(17)**, 11328-11334, (1991).

[86] I. Rasnik, S.H. McKinney & T. Ha, "Nonblinking and long-lasting single-molecule fluorescence imaging", *Nat. Methods*, **3(11)**, 891-893, (2006).

[87] R. Roy, S. Hohng & T. HA, "A practical guide to single-molecule FRET", *Nat. Methods*, **5(6)**, 507-516, (2008).

[88] A.B. Kochaniak, S. Habuchi, J.J. Loparo, D.J. Chang, K.A. Cimprich, J.C Walter & A.M. van Oijen, "Proliferating cell nuclear antigen uses two distinct modes to move along DNA", *J. Biol. Chem.*, **284(26)**, 17700-17710, (2009).

[89] E. Slager, "The diffusion of the beta clamp at dsDNA", *BSc. Thesis*, University of Groningen, under progress (2014).

[90] P.M. van Wezenbeek, T.J. Hulsebos & J.G. Schoenmakers, "Nucleotide sequence of the filamentous bacteriophage M13 DNA genome: comparison with phage fd", *Gene*, **11(1-2)**, 129-148, (1980).

[91] N.A. Tanner, J.J. Loparo, S.M. Hamdan, S. Jergic, N.E. Dixon & A.M. van Oijen, "Real-time single-molecule observation of rolling-circle DNA replication", *Nucleic Acids Res.*, **37(4)**, e27 (1-6), (2009).

[92] P.T. Stukenberg, J. Turner & M. O'Donnell, "An explanation for lagging strand replication: polymerase hopping among DNA sliding clamps", *Cell*, **78(5)**, 877-887, (1994).

[93] F.P. Leu, M.M. Hingorani, J. Turner & M. O'Donnell, "The δ subunit of DNA polymerase III holoenzyme serves as a sliding clamp unloader in *Escherichia coli*", *J. Biol. Chem.*, **275(44)**, 34609-34618, (2000).

[94] N.Y. Yao, R.E. Georgescu, J. Finkelstein & M.E. O'Donnell, "Single-molecule analysis reveals that the lagging strand increases replisome processivity but slows replication fork progression", *Proc. Natl. Acad. Sci. U.S.A.*, **106(32)**, 13236-13241, (2009).

[95] J. O. Wilkes, *Fluid mechanics for chemical engineers*, 2nd ed., Upper Saddle River, N.J: Prentice Hall PTR, (2005).

[96] Y. Cui, Q. Wei, H. Park & C.M. Lieber, "Nanowire nanosensors for highly sensitive and selective detection of biological and chemical species", *Science*, **293(5533)**, 1289-1292, (2001).

[97] J. Hahm & C.M. Lieber, "Direct ultrasensitive electrical detection of DNA and DNA sequence variations using nanowire nanosensors", *Nano Lett.*, **4(1)**, 51-54, (2004).

[98] F. Patolsky, G. Zheng & C.M. Lieber, "Nanowire-based biosensors", *Anal. Chem.*, **78**, 4260-4269, (2006).

[99] G.A. Kalkman, "Doubly clamped, ultra-long gold nanowires suspended freely in micrsocannels", *MSc. Thesis,* University of Groningen, (2013).

[100] D. Janssen, R. de Palma, S. Verlaak, P. Heremans & W. Dehaen, "Static solvent contact angle measurements, surface free energy and wettability determination of various self-assembled monolayers on silicon dioxide", *Thin Solid Films*, **515**, 1433-1438, (2006).

[101] Q. Xu, R.M. Rioux, M.D. Dickey & G.M. Whitesides, "Nanoskiving: a new method to produce arrays of nanostructures", *Acc. Chem. Res.*, **41(12)**, 1566-1577, (2008).

[102] G.U. Lee, L.A. Chrisey & R.J. Colton, "Direct measurement of forces between complementary strands of DNA", *Science*, **266(5186)**, 771-773, (1994).

[103] J. Wong, A. Chilkoti & V.T. Moy, "Direct force measurements of the streptavidin-biotin interaction", *Biomol. Eng.*, **16**, 45-55, (1999).

Appendix A: List of buffer solutions

Blocking buffer (BB)   **pH = 7.5**
- 20 mM Tris
- 2 mM EDTA
- 50 mM NaCl
- 1 mg/mL BSA
- 0.025% Tween 20

***E. coli* replication buffer (+)**   **pH = 7.9**
- 50 mM HEPES
- 80 mM KCl
- 12 mM MgOAc
- 0.1 mg/ml BSA

***E. coli* replication buffer (-)**   **pH = 7.9**
- 50 mM HEPES
- 80 mM KCl
- 0.1 mg/ml BSA

T7 replication buffer (+)   **pH = 7.5**
- 40 mM Tris
- 50 mM K-glutamate
- 10 mM $MgCl_2$
- 0.1 mg/ml BSA

T7 replication buffer (-)   **pH = 7.5**
- 40 mM Tris
- 50 mM K-glutamate
- 2 mM EDTA
- 0.1 mg/ml BSA

HU buffer   **pH = 7.9**
- 60 mM KCl
- 20 mM HEPES

β buffer   **pH = 7.9**
- 40 mM Tris
- 80 mM KCl
- 12 mM MgOAc
- 0.1 mg/ml BSA

Appendix B: Conversion sheet λ phage DNA length calibration
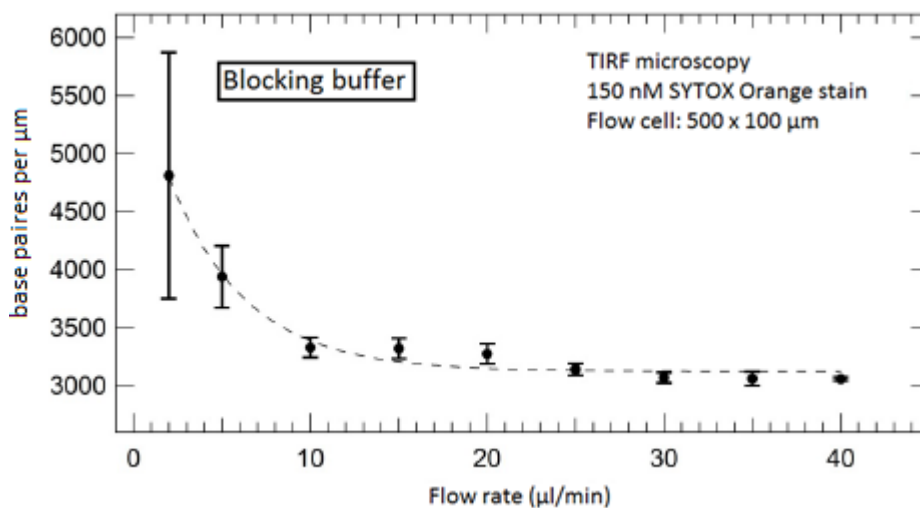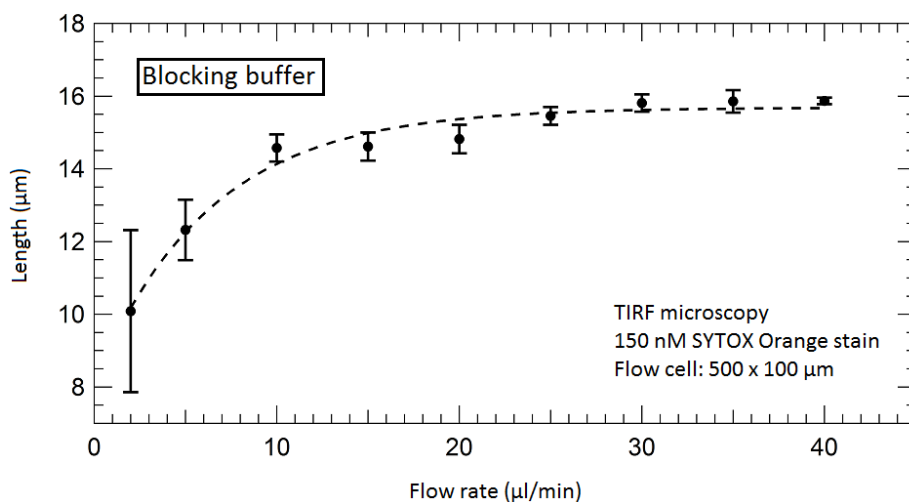
| Buffers | base pairs per µm | | length (µm) | |
	conversion	error	conversion	error
BB	1.000	0.047	1.000	0.047
T7 (-)	0.998	0.056	1.002	0.056
E. coli (+)	1.169	0.058	0.855	0.042
T7 (+)	1.145	0.063	0.874	0.048
β	1.124	0.077	0.890	0.061

Pick length or conversion factor (base pairs per µm) at the used flow rate and correct for the buffer by multiplying the value with buffer conversion factor from the table

Machteld Kamminga
Enrico Monachino
19/05/2014

Appendix C: Protocols M13 replication experiments

1. **Standard protocol replication experiments Van Oijen Lab with labelled β clamps (stock concentration varies for different labels) for replication mixture of 500 μl.**

Component	Function	Stock	Volume	Final concentration
ATP	ribonucleotides, ATP used as energy source	100 mM	5 μl	1 mM
CTP		100 mM	1.25 μl	250 μM
UTP		100 mM	1.25 μl	250 μM
GTP		100 mM	1.25 μl	250 μM
dNTPs	deoxyribonucleotides	25 mM	2 μl	50 μM
$\tau_3\delta\delta'\chi\psi$	clamp-loader complex	3.5 μM	2.14 μl	15 nM
β	clamp	-	-	around 14 nM
DnaB/DnaC	helicase with loader	6.5 μM	2.3 μl	30 nM
DnaG	primase	47 μM	1.1 μl	100 nM
$\alpha\epsilon\theta$	polymerase	8.1 μM	1.85 μl	30 nM
SSB	single-stranded binding protein	56 μM	2.2 μl	250 nM
Pri A	restart proteins	12 μM	0.83 μl	20 nM
Pri B		101 μM	0.19 μl	40 nM
Pri C		123 μM	1.3 μl	320 nM
DnaT		191 μM	1.32 μl	480 nM
Glucose	oxygen scavenging system	2 M	10 μl	40 mM
Catalase		16 μM	2 μl	64 nM
Glucose oxidase		62.5 μM	2 μl	250 nM
DTT		1 M	5 μl	10 mM
Trolox		10 mM	50 μl	1 mM
Stain	intercalating dye	50 μM	1.5 μl	150 nM
Buffer	bring total volume to 500 μl	-	405 μl	-

The buffer should always be heated up to 37 °C and degassed before use. The buffer needs to be degassed to avoid air bubbles in the flow cell, which can break the DNA constructs. The microscope setup contains a heater to keep the temperature within the flow cell at 37 °C, which is required for the *E. coli* proteins to work.

2. Modified protocol replication experiments Van Oijen Lab with labelled β clamps, pre-loading of the DnaB/DnaC complex and without restarts proteins.

Pre-loading mixture of 500 μl (with 37.5 nM DnaB/DnaC compex), to give binding of the DnaB/DnaC complex to the DNA template a 'head start'. After flowing in 100 μl, the replication mixture of 100 μl is added to create again a 500 μl replication mixture (with 30 nM DnaB/DnaC complex).

Component	Function	Stock	Volume	Final concentration
ATP	energy source	100 mM	5 μl	1 mM
DnaB/DnaC	helicase with loader	6.5 μM	2.9 μl	37.5/30 nM
DTT	enhance signal	1 M	2.5 μl	5 mM
Stain	intercalating dye	50 μM	1.5 μl	150 nM
Buffer	bring total volume to 500 μl	-	488 μl	-

Replication mixture in 100 μl. The final concentration represents the concentration when added to the 400 μl left-over from the above mixture.

Component	Function	Stock	Volume	Final concentration
ATP		100 mM	1 μl	1 mM
CTP	ribonucleotides,	100 mM	1.25 μl	250 μM
UTP	ATP used as energy source	100 mM	1.25 μl	250 μM
GTP		100 mM	1.25 μl	250 μM
dNTPs	deoxyribonucleotides	25 mM	4 μl	100 μM
$\tau_3\delta\delta'\chi\psi$	clamp-loader complex	3.5 μM	2.14 μl	15 nM
β	clamp	-	-	around 10 nM
DnaG	primase	47 μM	1.1 μl	100 nM
$\alpha\epsilon\theta$	polymerase	8.1 μM	1.85 μl	30 nM
SSB	single-stranded binding protein	56 μM	2.2 μl	250 nM
Glucose		2 M	10 μl	40 mM
Catalase		16 μM	2 μl	64 nM
Glucose oxidase	oxygen scavenging system	62.5 μM	2 μl	250 nM
DTT		1 M	0.5 μl	5 mM
Trolox		10 mM	50 μl	1 mM
Stain	intercalating dye	50 μM	1.5 μl	150 nM
Buffer	bring total volume to 100 μl	-	18 μl	-

The buffer should always be heated up to 37 °C and degassed before use. The buffer needs to be degassed to avoid air bubbles in the flow cell, which can break the DNA constructs. The microscope setup contains a heater to keep the temperature within the flow cell at 37 °C, which is required for the *E. coli* proteins to work.

Appendix D: Protocols flow cell construction

This appendix gives the protocols for flow cell construction, including making the lithography masters, making the PDMS channels and HF etching the glass channels.

1.   Making PDMS masters with photolithography

This work requires a cleanroom with UV-free light. The top part of figure D.1 illustrates the procedure.

- Wafer cleaning:
    - Acetone
    - Isopropanol
    - Milli-Q water
    - Bake at 150 °C for 5 minutes
    - Cool down to room temperature
- Spin coat 4.5 ml SU-8 (negative photoresist, highly viscous polymer that will internally cross-link and harden under UV exposure) into a 100 μm thick layer (note that this will result in a 100 μm high flow channel):
    - Step 1:
        - Velocity: 500 rpm
        - Ramp: 100 rpm/s
        - Time: 13 seconds
    - Step 2:
        - Velocity: 1000 rpm
        - Ramp: 300 rpm/s
        - Time: 43 seconds
- Soft bake step:
    - Keep wafers at room temperature for 30 minutes
    - 65 °C for 10 minutes
    - 95 °C for 30 minutes
    - Cool down to room temperature
- Exposure:
    - Stabilize UV lamp temperature for 10 minutes
    - Place wafer under lamp with mask on top of it
    - Cover mask with borofloat wafer to prevent movement of mask during exposure (will result in bad quality structures)
    - Expose wafer wit;h dose of 250 mJ/cm^2
- Post exposure bake step
    - 65 °C for 1 minute
    - 95 °C for 10 minutes
    - Cool down to room temperature
- Development step:
    - Put wafers in SU-8 developer
    - Shake gently for 10 minutes
    - Put wafers in fresh developer for another 5 minutes

- Rinse with isopropanol
- Repeat steps if necessary
- HMDS (hexamethyldisilane) step (makes it easier to remove PDMS from the masters):
  - Put wafer in evaporator with plastic beaker with few droplets of HMDS
  - Evaporate for 30 minutes

2.   Making PDMS channels

This work does not require a cleanroom and starts from the PDMS masters described above. The bottom part of figure D.1 illustrates the procedure.

- Clean PDMS masters with ethanol
- Place master in square Petri dish and tape around the wafers to fix them and prevent air and PDMS to get under the wafer
- Mix PDMS monomer and curing agent in 10:1 ratio by weight in beakers (around 150 g in total needed)
- Stir mixture thoroughly for at least three minutes
- Place beakers under vacuum for at least half an hour to remove all air bubbles
- Pour mixtures in Petri dish to get a height of around 8 mm
- Place open under vacuum to remove residual air bubbles
- Bake at 60 °C for 2 hours to harden the PDMS
- Cool down to room temperature
- Use razor blade to cut the PDMS and pull it from the wafers. Cut PDMS to maximum size of 24 x 24 mm, to fit the device holder
- Make the channel inlets (1.2 mm) in PDMS blocks for PE-60 tubing
- Clean PDMS flow channels by sonicating for 20 minutes in:
  - 0.5% triton
  - $NaHCO_3$ (1 M)
  - 70% EtOH.
  - Wash with Milli-Q water, dry and store
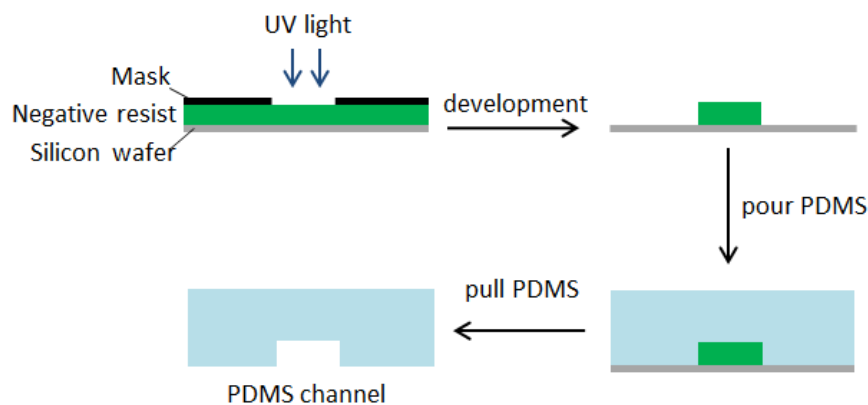- Petri dishes can be reused as a mold for making more flow channels

Figure D.1: Illustration of PDMS flow channel fabrication using photolithography.

3.   HF etching of glass channels

This work requires a cleanroom with UV-free light. Figure D.2 illustrates this procedure.

This etching needs to be performed in an 25 % containing HF-etching solution (hydrofluoric acid) that consists of 49 % HF, 70 % HNO_3 and water in a ratio of 100:28:70. HF is highly dangerous, because it searches for calcium. In other words, it will go through the skin to eat the bones, leaving significant burn marks behind. Therefore, important safety guidelines apply.

Safety guidelines:
- Never work alone. The second person should not touch the HF and wear an alarm batch
- Wear gloves, face shield, protective apron, glasses and second HF-resistant gloves with long sleeves up to the armpits
- HF may only be used in a cleanroom under a working fume hood
- Only use beakers and flasks made of Teflon and always keep these in a drip tray to avoid spreading of spilled HF
- Everything that has been in contact with HF should be rinsed directly after us
- Use a separated waste container for HF-contaminated liquid waste

Procedure:

- Exposure:
  - Stabilize UV lamp temperature for 10 minutes
  - Place coverslips under lamp with mask on top of it
  - Cover mask with borofloat wafer to prevent movement of mask during exposure (will result in bad quality structures)
  - Expose coverslips with dose of 45 mJ/cm^2
- Development steps 1 and 2:
  - Put coverslips in 3:1 water-diluted AZ351B developer for 60 seconds to expose chromium
  - Rinse with water
  - Postbake at 115 °C for 50 seconds
  - Put coverslips in Chrom etch for 50 seconds to expose glass. Use microscope to check if all chromium is removed and put in Chrom etch longer if necessary
- HF etching:
  - Put coverslips in customized Teflon holder
  - Carefully place holder in HF-containing solution (see above)
  - Leave for 20 minutes (etching speed is around 1.8 μm/min)
  - Gently shake the holder every minute
  - Put holder with coverslips in ultrapure water bath for 5 minutes to stop etching process (use a lot of water to significantly dilute HF to stop etching)
- Development steps 3 and 4:
  - Remove photoresist with acetone
  - Rinse with water
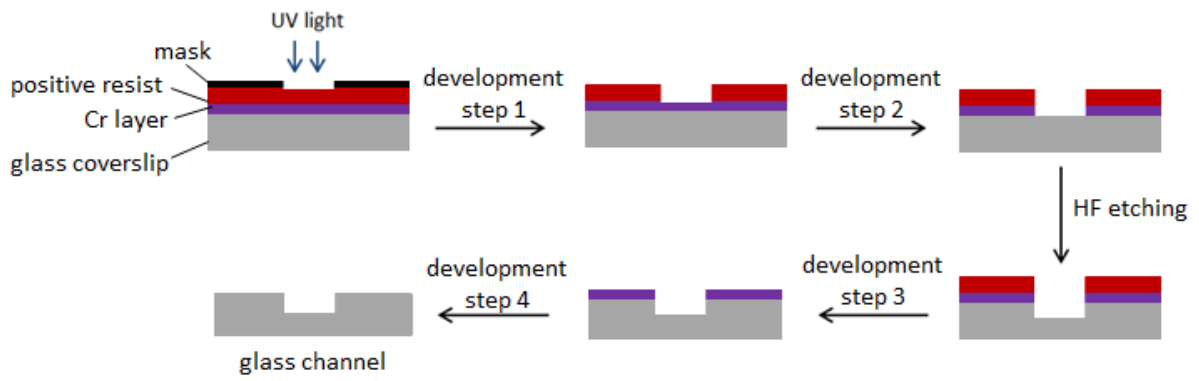 - Remove chromium layer with Chrom etch
  - Rinse with water

Figure D.2: Illustration of HF etching procedure used to create etched glass channels. The chromium layer is 1200 Å and the AZ1500 photoresist layer is 5300 Å in thickness.